Electronic Supplementary Material (ESI) for New Journal of Chemistry.

The acronyms L12-L15 in the formulae of complexes in ESI-MS represent the completely deprotonated form of the ligands (as L in the general formula of complexes in the *Potentiometric-spectrophotometric measurements* section), so, as an example, $(L12)H_3$ is the completely protonated ligand.

Figure S1. ESI-MS spectrum in positive mode for the L12 compound.

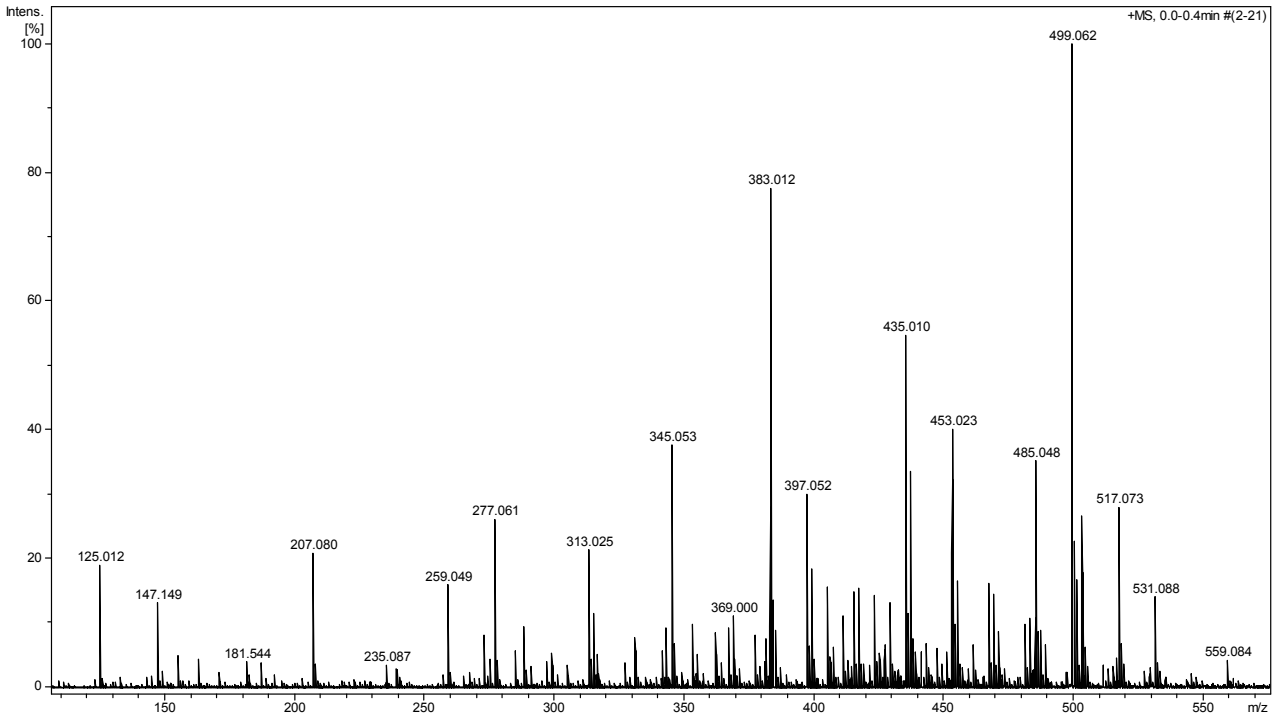

Figure S1A. Experimental data for the peaks m/z = 435.010 and 453.023 are shown at the top of the panel and compared with the data calculated for the $[(L12)H_3+H_2O+H]^+$ ($C_{20}H_{19}O_{11}$) and $[(L12)H_3+2H_2O+H]^+$ ($C_{20}H_{21}O_{12}$) (lower panels).

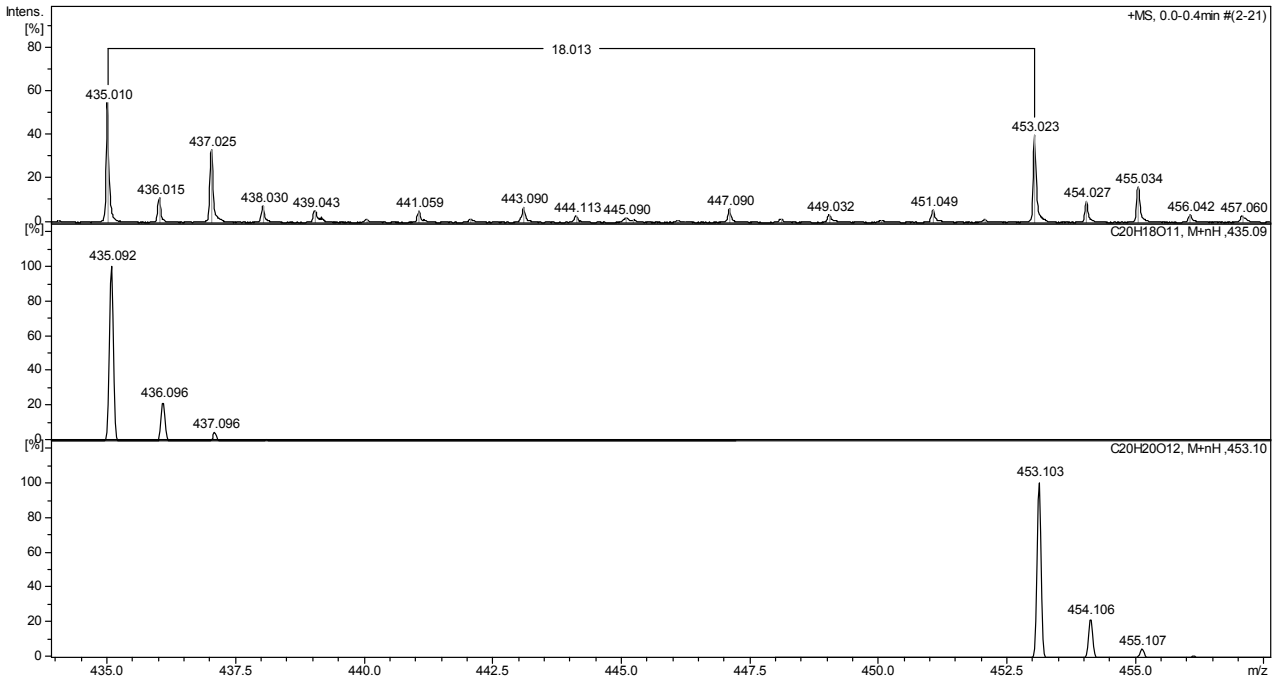

Figure S2. ESI-MS spectrum in negative mode for the L12 compound.

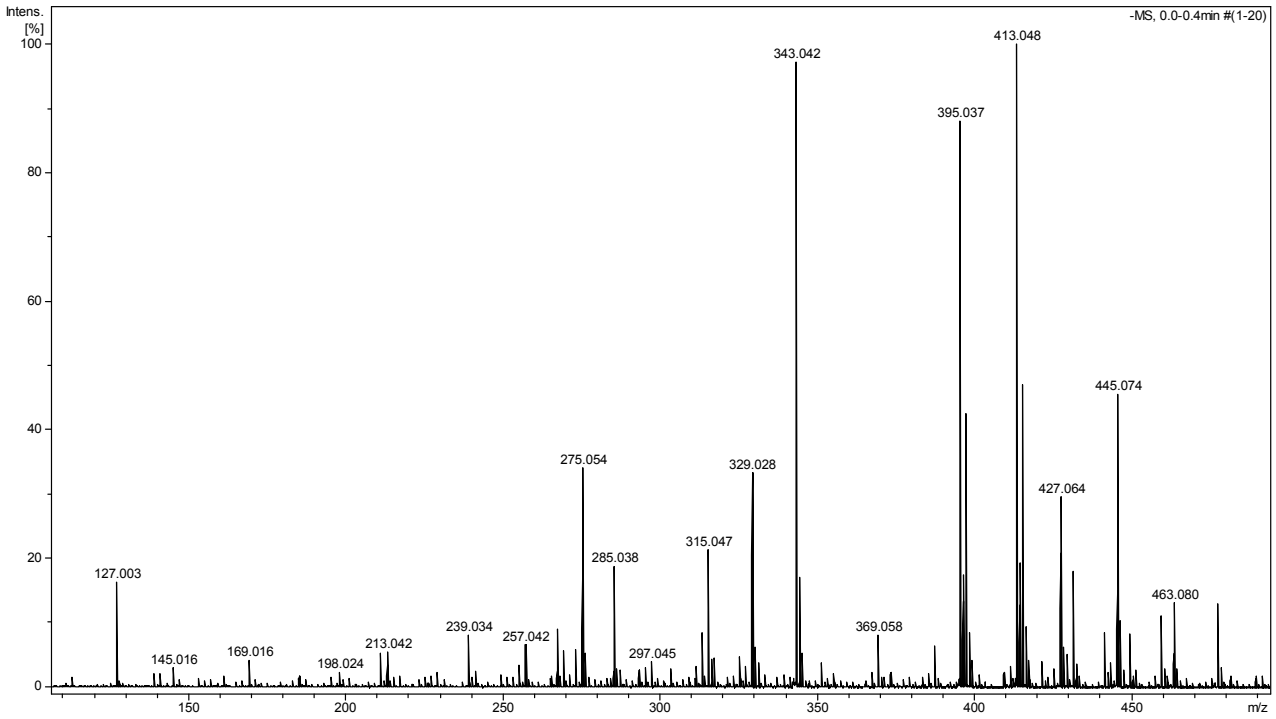

Figure S2A. Experimental data for the peaks m/z = 413.048 and 415.066 are shown at the top of the panel and compared with the data calculated for the $[(L12_{ox})]^-$ ($C_{20}H_{13}O_{10}$) and $[(L12)H_2]^-$ ($C_{20}H_{15}O_{10}$) (lower panels).

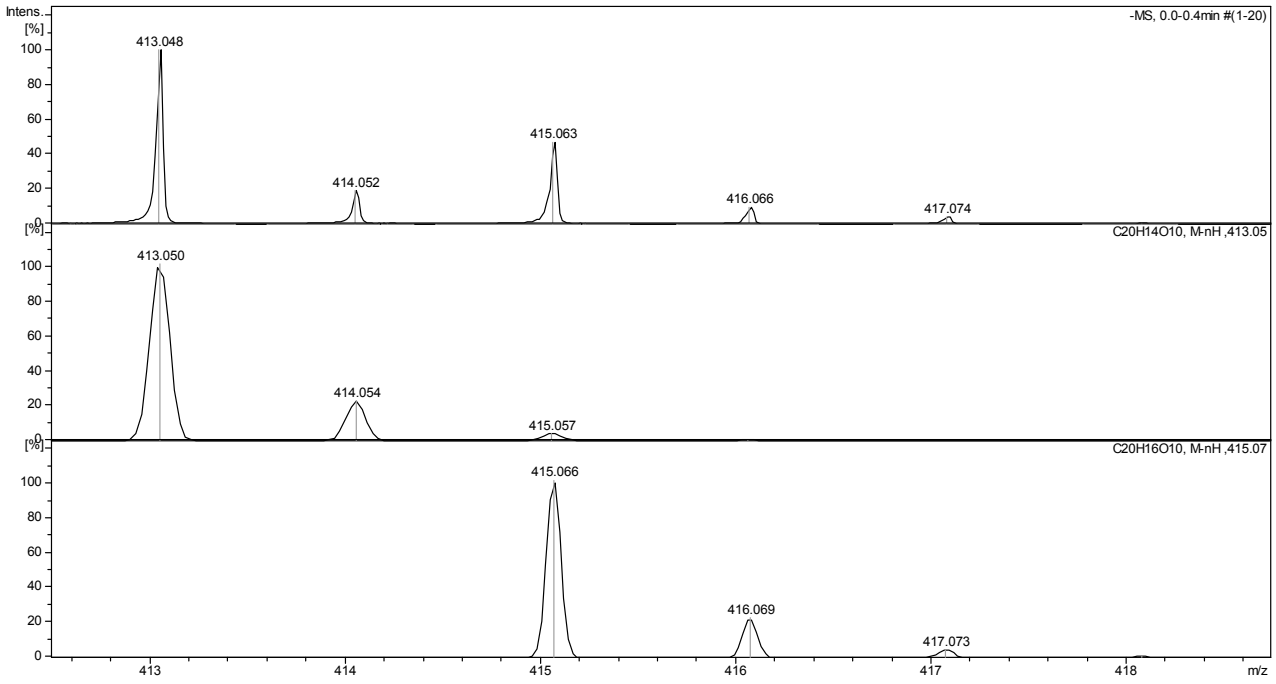

Figure S3. The full spectrum of L12-Al^{3+} solution in the 1:1 metal-to-ligand molar ratio in positive mode.

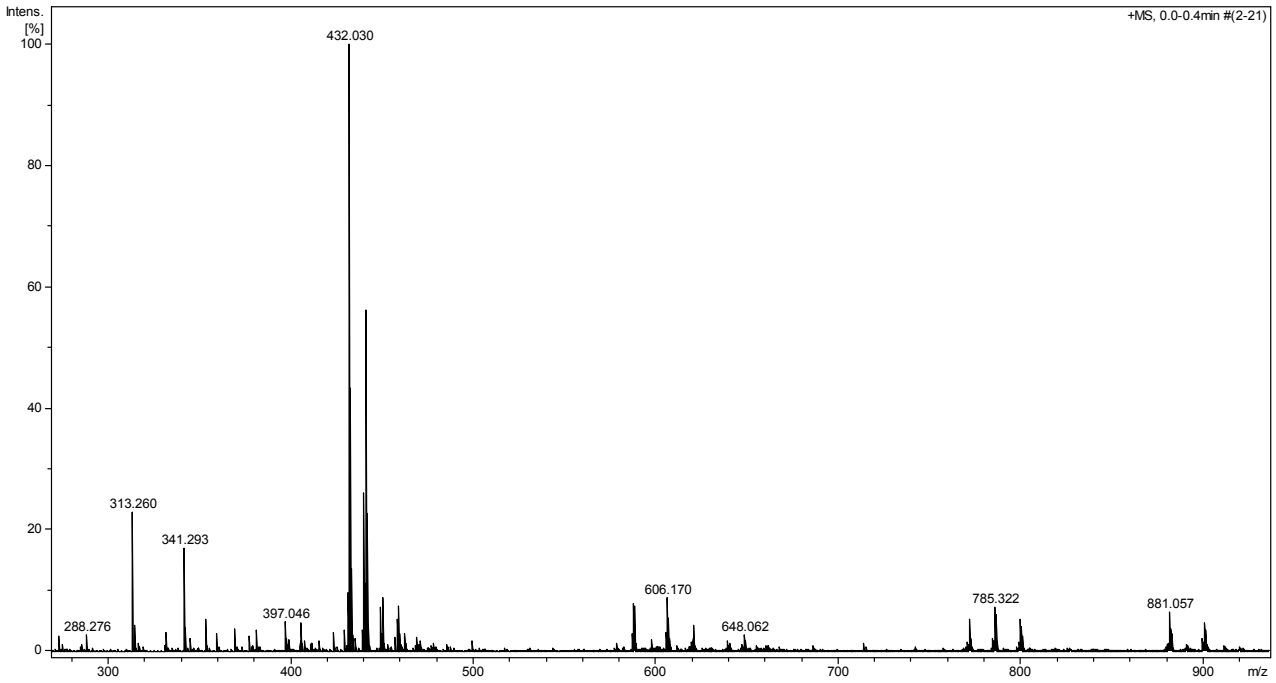

Figure S3A. Experimental data for the peaks m/z = 441.035, 450.041 and 459.045 are shown at the top of the panel and compared with the data calculated for the $[Al_2(L12)_2H_2]^{2+}$ ($C_{40}H_{28}Al_2O_{20}$), $[Al_2(L12)_2H_2+H_2O]^{2+}$ ($C_{40}H_{30}Al_2O_{21}$) and $[Al_2(L12)_2H_2+2H_2O]^{2+}$ ($C_{40}H_{32}Al_2O_{22}$) complexes (lower panels).

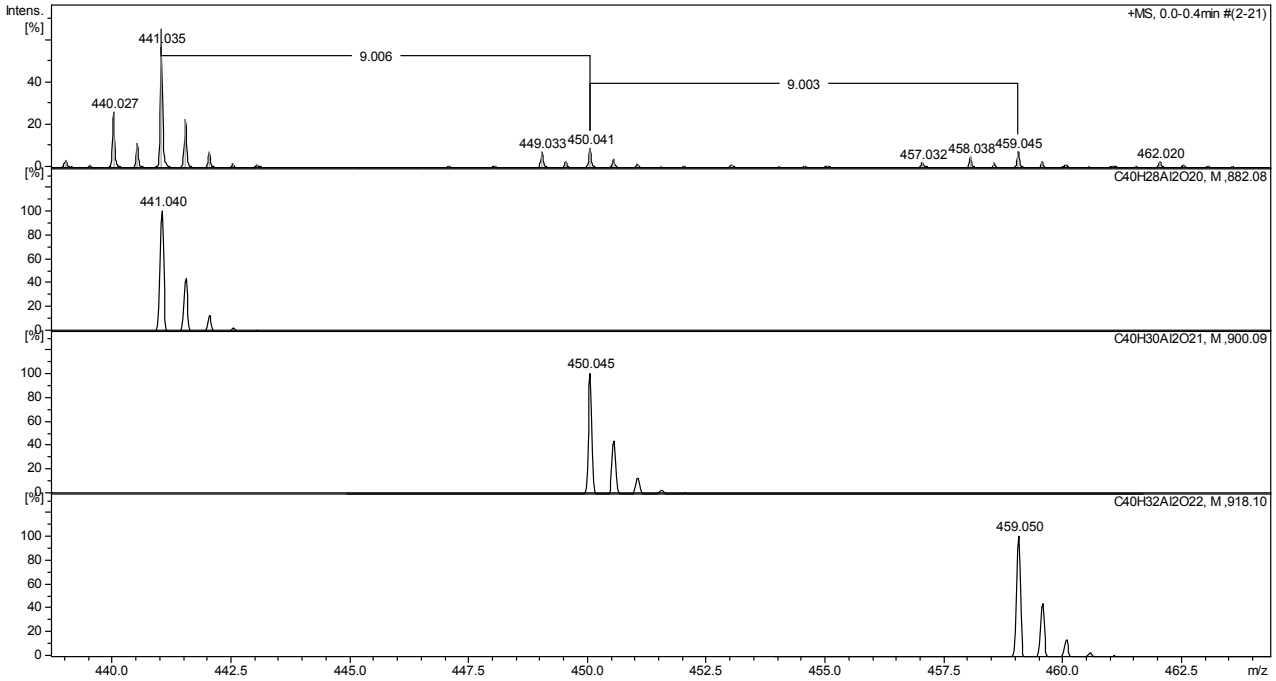

Figure S3B. Experimental data for the peaks m/z = 440.027, 449.033 and 458.038 are shown at the top of the panel and compared with the data calculated for the $[Al_2(L12_{ox})_2]^{2+}$ ($C_{40}H_{26}Al_2O_{20}$), $[Al_2(L12_{ox})_2+H_2O]^{2+}$ ($C_{40}H_{28}Al_2O_{21}$) and $[Al_2(L12_{ox})_2+2H_2O]^{2+}$ ($C_{40}H_{30}Al_2O_{22}$) complexes (lower panels).

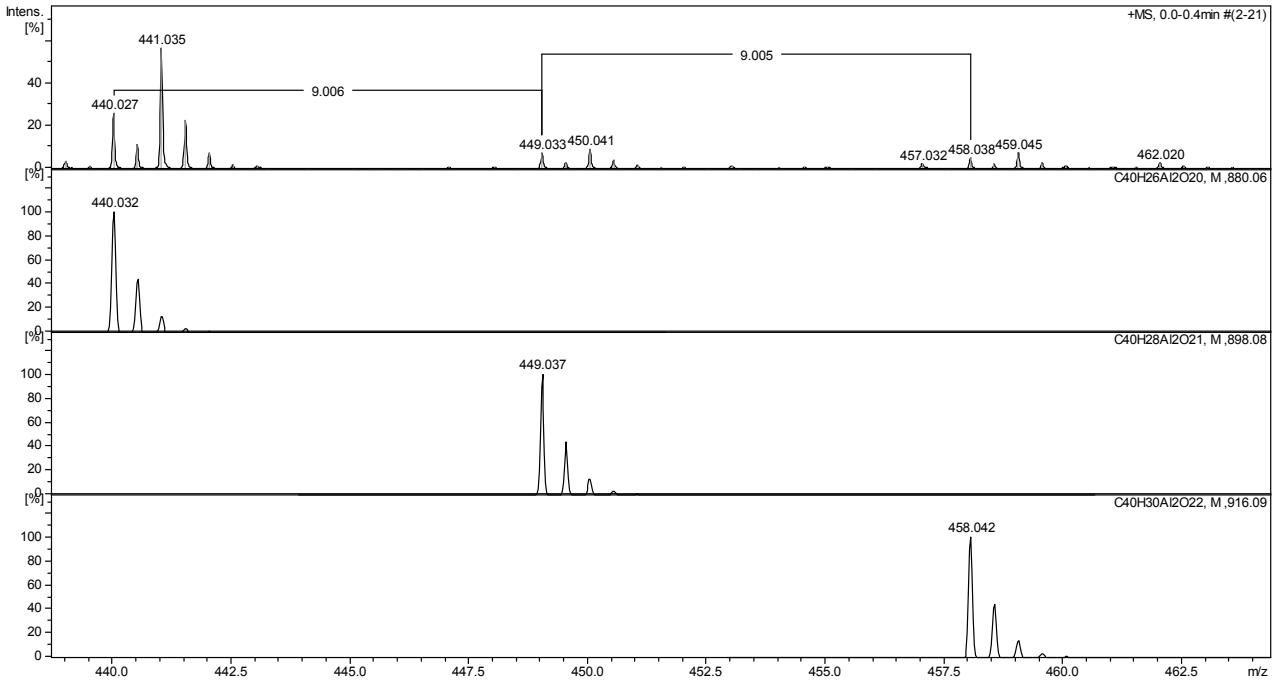

Figure S4. The full spectrum of L12-Al^{3+} solution in the 1:1 metal-to-ligand molar ratio in negative mode.

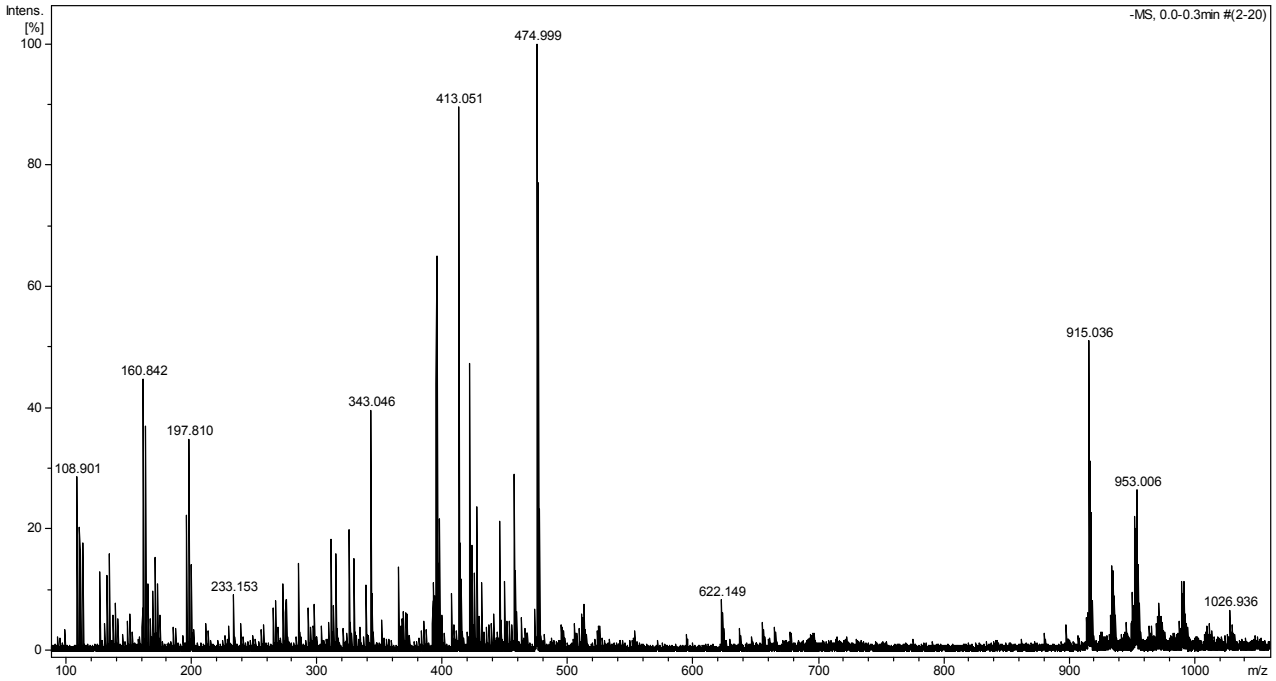

Figure S4A. Experimental data for the peak m/z = 474.999 is shown at the top of the panel and compared with the data calculated for the $[Al_2(L12)_2+2Cl]^{2-}$ ($C_{40}H_{26}Al_2Cl_2O_{20}$) complex (lower panel).

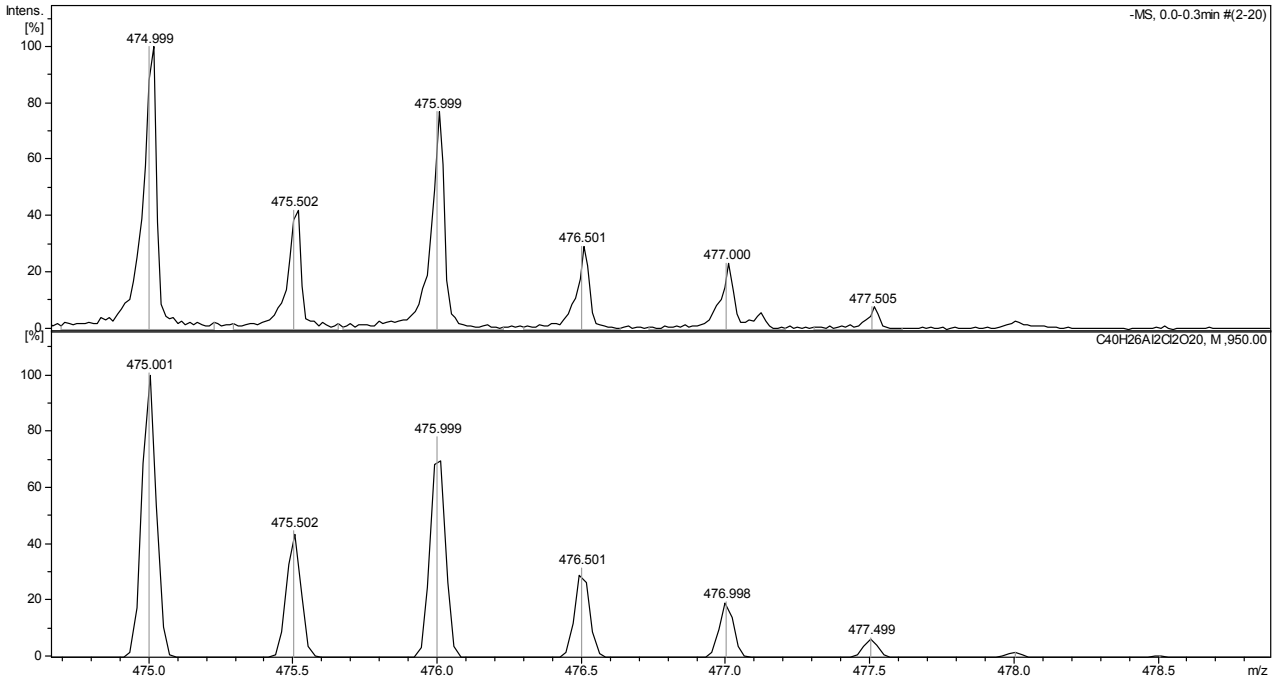

Figure S4B. Experimental data for the peaks m/z = 915.036, 933.022 and 951.009 are shown at the top of the panel and compared with the data calculated for the $[Al_4(L12)_4+2Cl]^{2-}$($C_{80}H_{52}Al_4Cl_2O_{40}$), $[Al_4(L12)_4+2Cl+2H_2O]^{2-}$ ($C_{80}H_{56}Al_4Cl_2O_{42}$) and $[Al_4(L12)_4+2Cl+4H_2O]^{2-}$ ($C_{80}H_{60}Al_4Cl_2O_{44}$) complexes (lower panel).

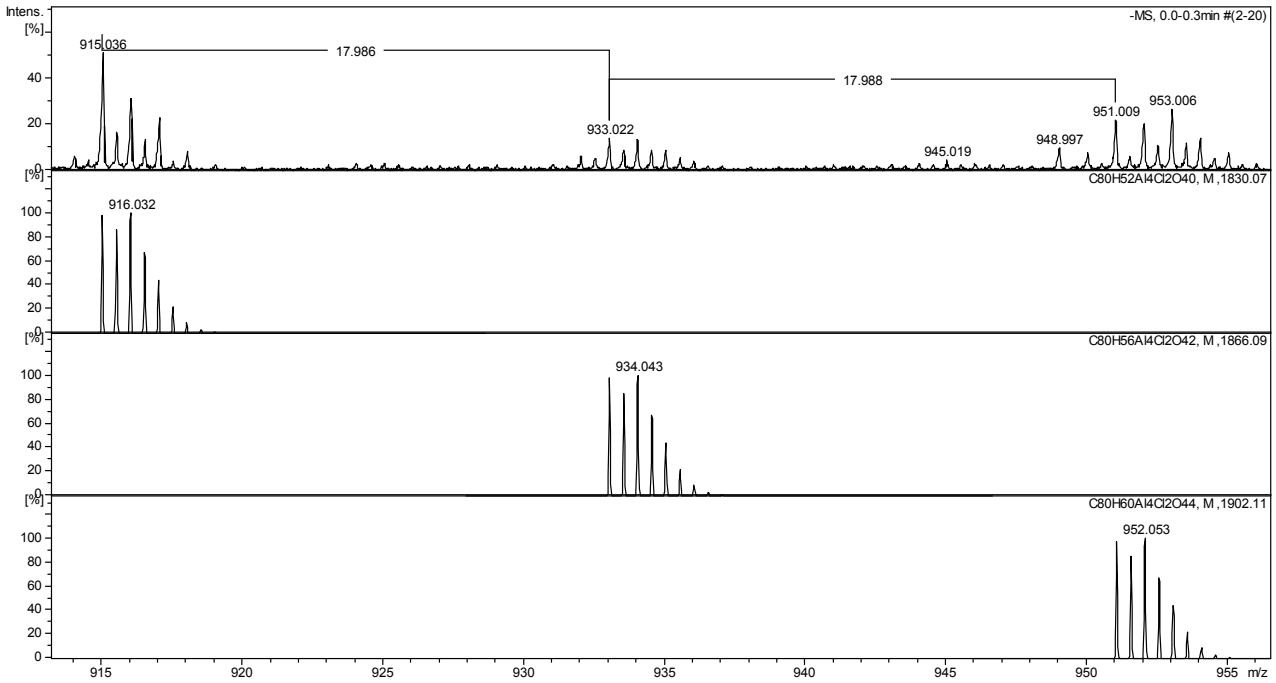

Figure S5. The full spectrum of L12-Cu^{2+} solution in the 1:1 metal-to-ligand molar ratio in positive mode.

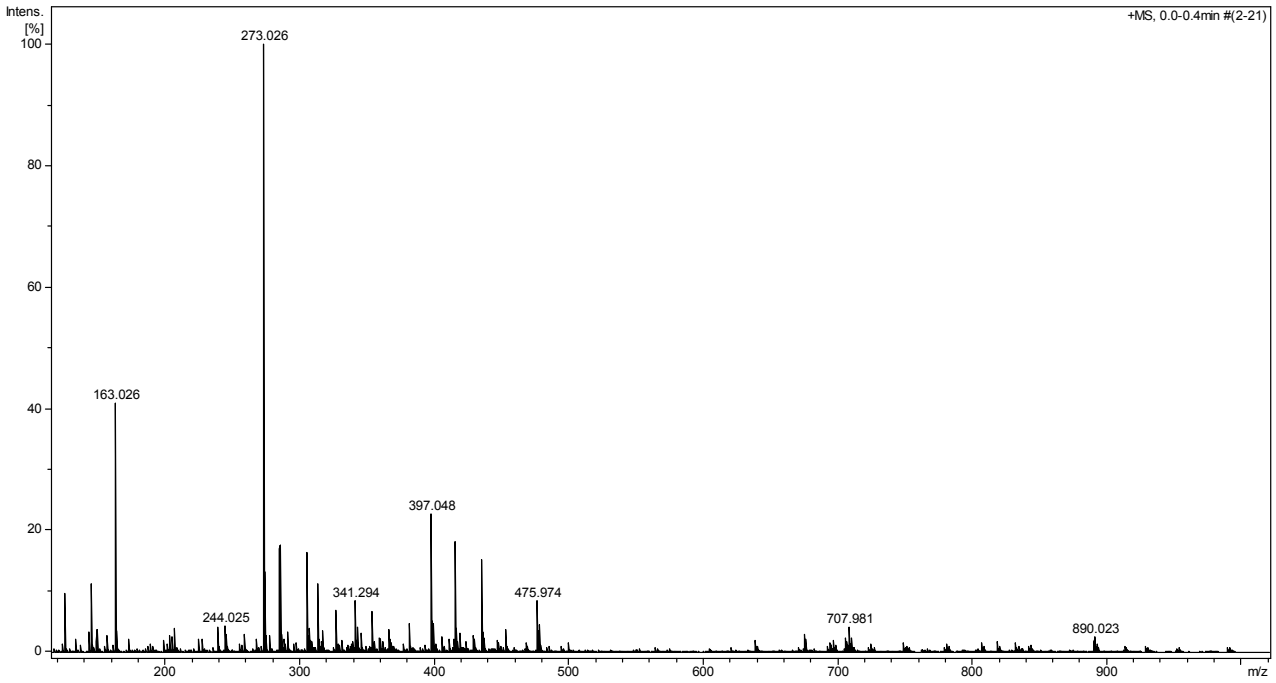

Figure S5A. Experimental data for the peaks m/z = 475.974 and 493.980 are shown at the top of the panel and compared with the data calculated for the $[Cu(L12_{ox})]^{+}$ ($C_{20}H_{13}CuO_{10}$), $[Cu_2(L12_{ox})_2]^{2+}$ ($C_{40}H_{26}Cu_2O_{20}$) and $[Cu(L12_{ox})+H_2O]^{+}$ ($C_{20}H_{15}CuO_{11}$) complexes (lower panels).

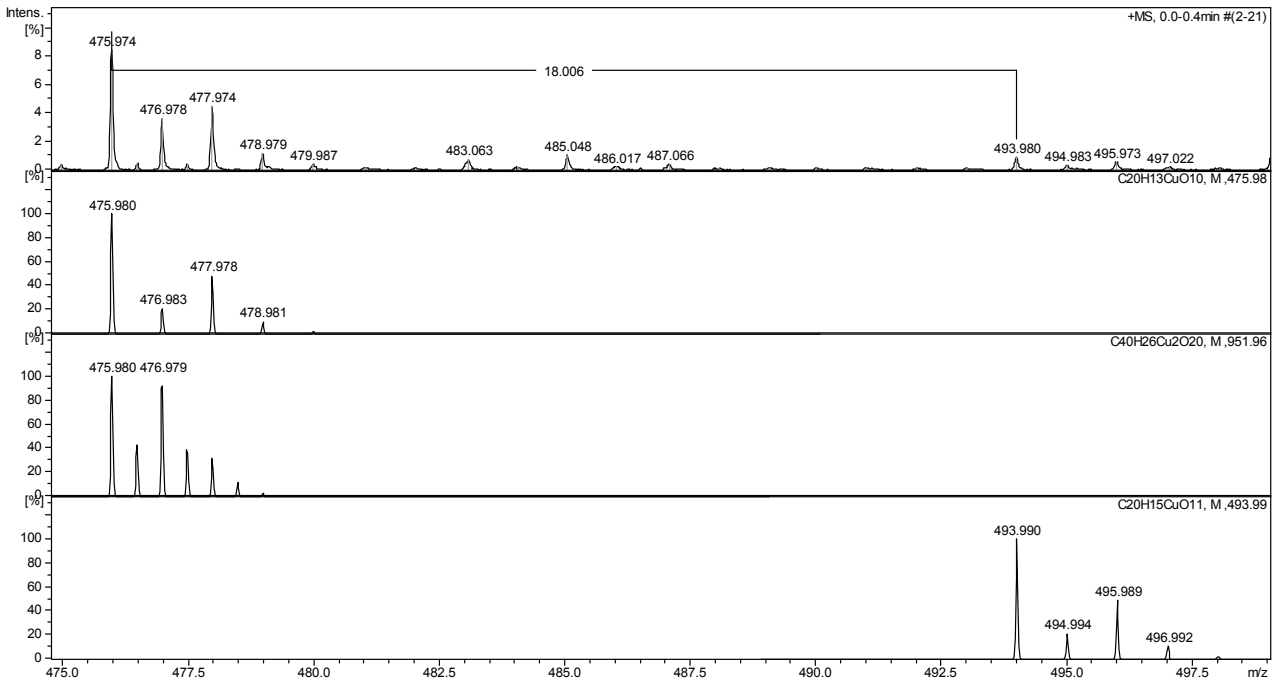

Figure S6. The full spectrum of L12- Fe^{3+} solution in the 1:1 metal-to-ligand molar ratio in positive mode.

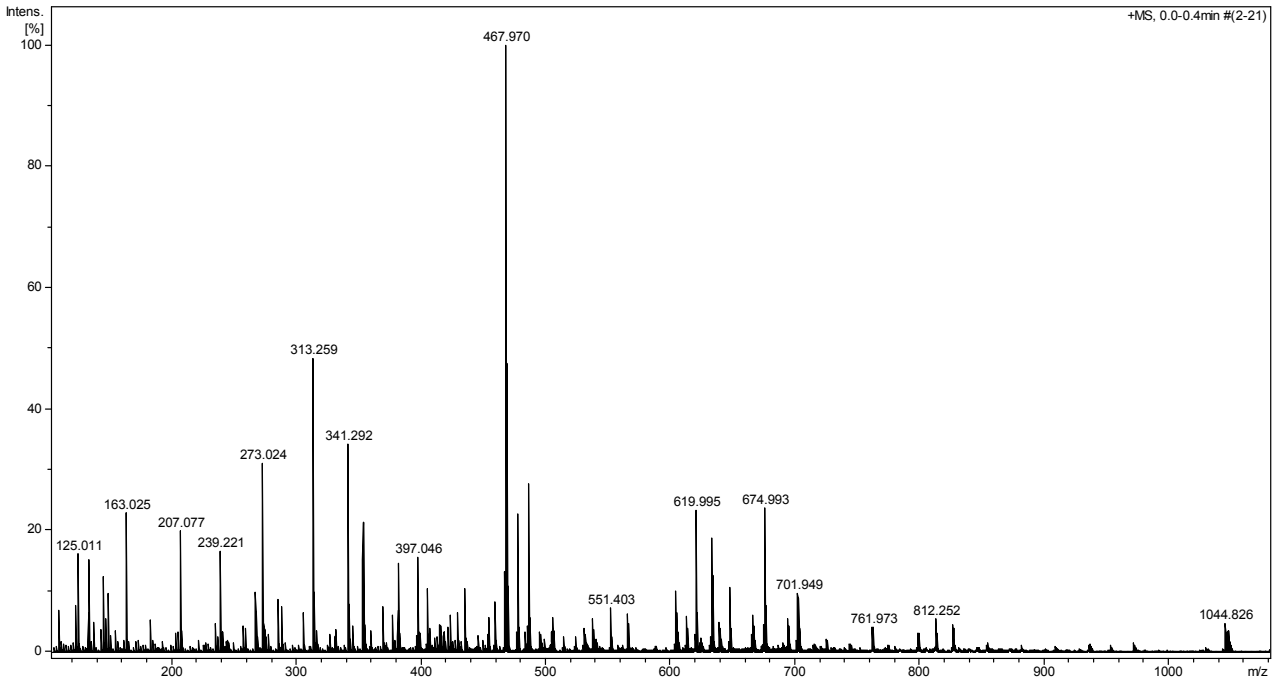

Figure S6A. Experimental data for the peaks m/z = 466.973, 475.976, 484.991 and 493.980 are shown at the top of the panel and compared with the data calculated for the $[Fe_2(L12_{ox})_2]^{2+}$ ($C_{40}H_{24}Fe_2O_{20}$), $[Fe_2(L12_{ox})_2+H_2O]^{2+}$ ($C_{40}H_{26}Fe_2O_{21}$), $[Fe_2(L12_{ox})_2+2H_2O]^{2+}$ ($C_{40}H_{28}Fe_2O_{22}$) and $[Fe_2(L12_{ox})_2+3H_2O]^{2+}$ ($C_{40}H_{30}Fe_2O_{23}$) complexes (lower panels).

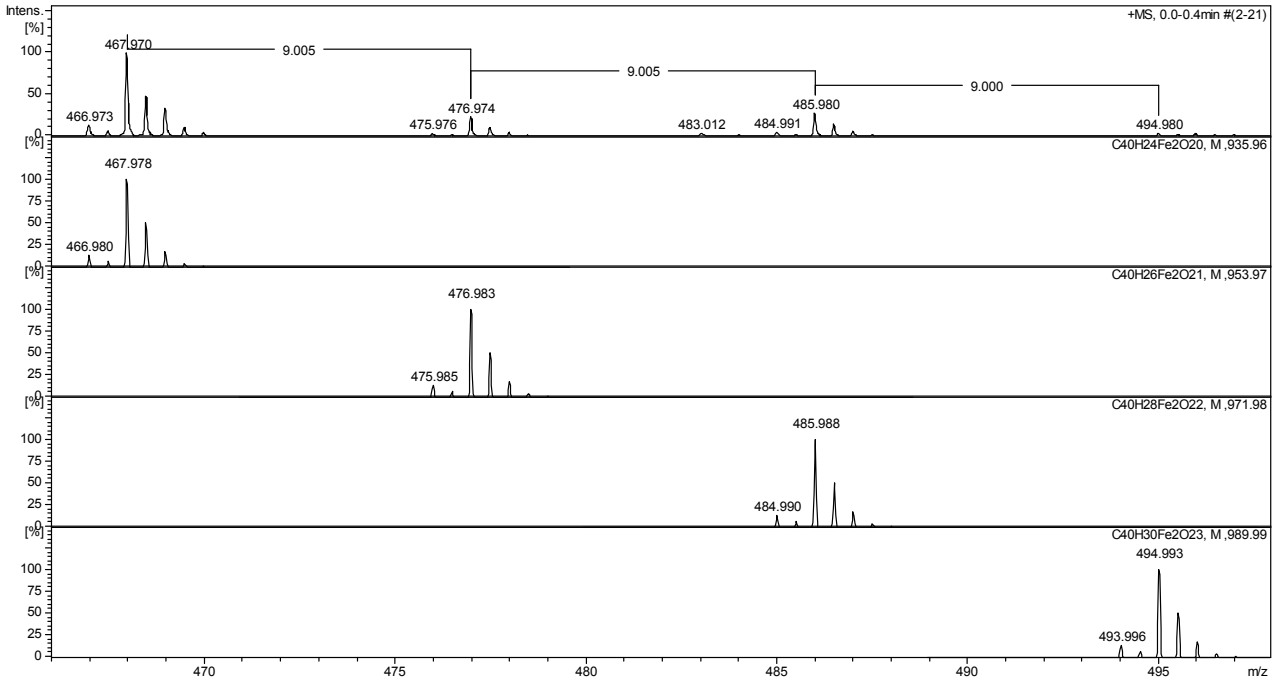

Figure S7. The full spectrum of L12- Fe^{3+} solution in the 1:1 metal-to-ligand molar ratio in negative mode.

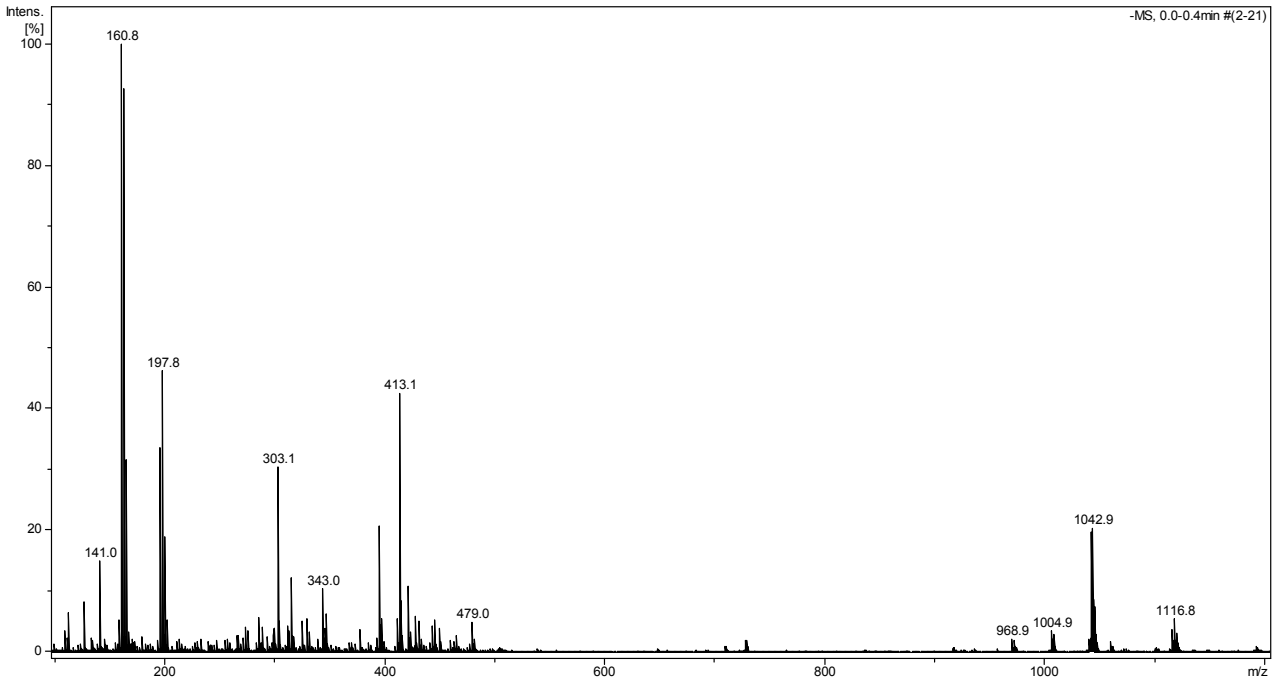

Figure S7A. Experimental data for the peak m/z = 1040.870 are shown at the top of the panel and compared with the data calculated for the $[Fe_2(L12_{ox})_2+3Cl]^-$ ($C_{40}H_{24}Cl_3Fe_2O_{20}$) complex (lower panel).

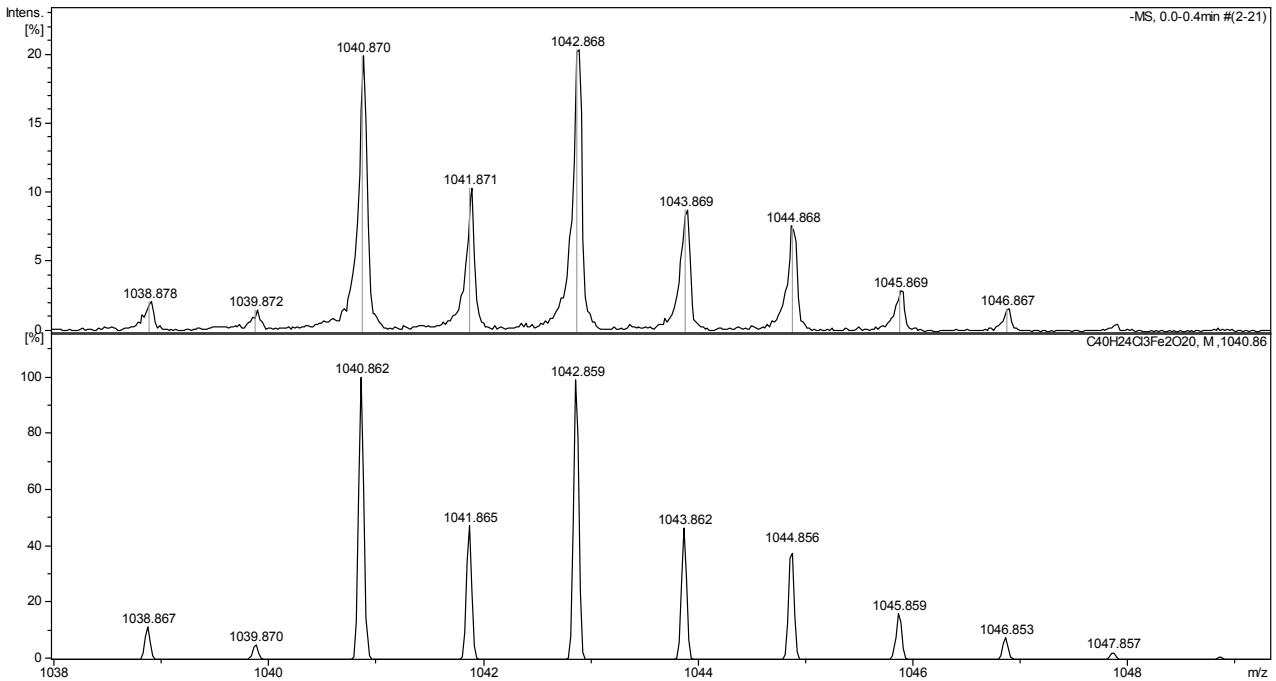

Figure S8. The full spectrum of L12-Zn^{2+} solution in the 1:1 metal-to-ligand molar ratio in positive mode.

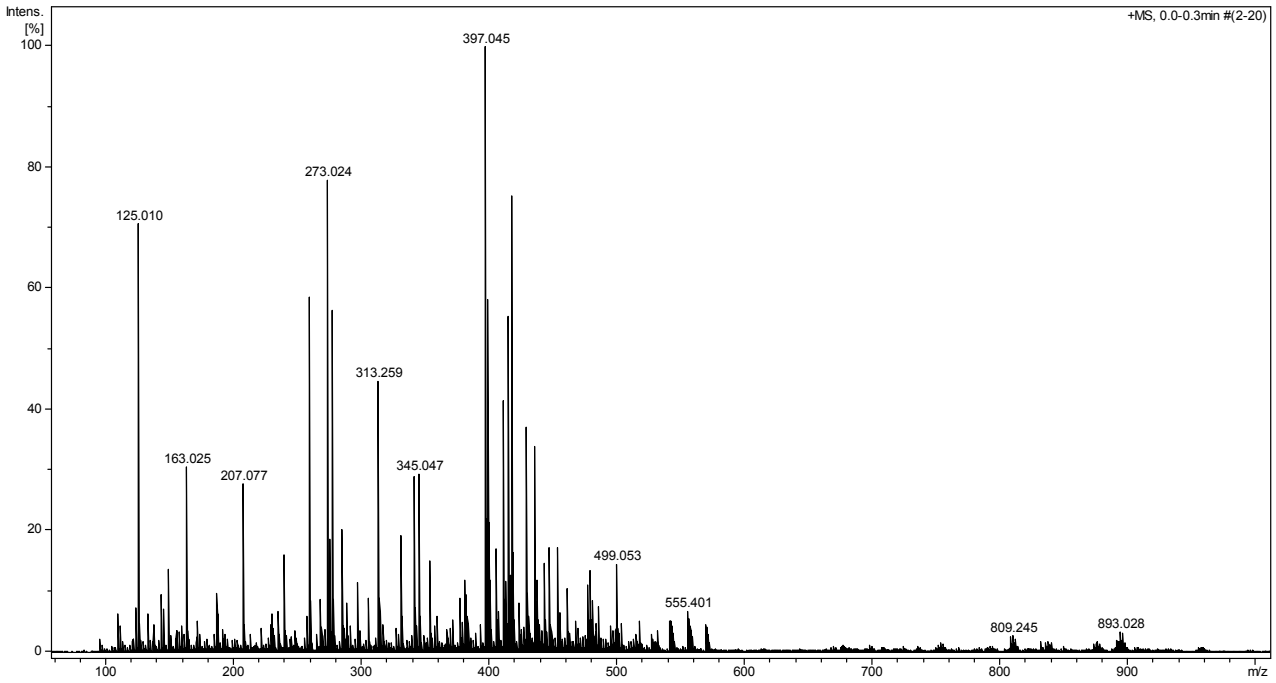

Figure S8A. Experimental data for the peaks m/z = 476.972 and 478.979 are shown at the top of the panel and compared with the data calculated for the $[Zn(L12_{ox})]^+$ ($C_{20}H_{13}ZnO_{10}$) and $[Zn(L12)H_2]^+$ ($C_{20}H_{15}ZnO_{10}$) complexes (lower panels).

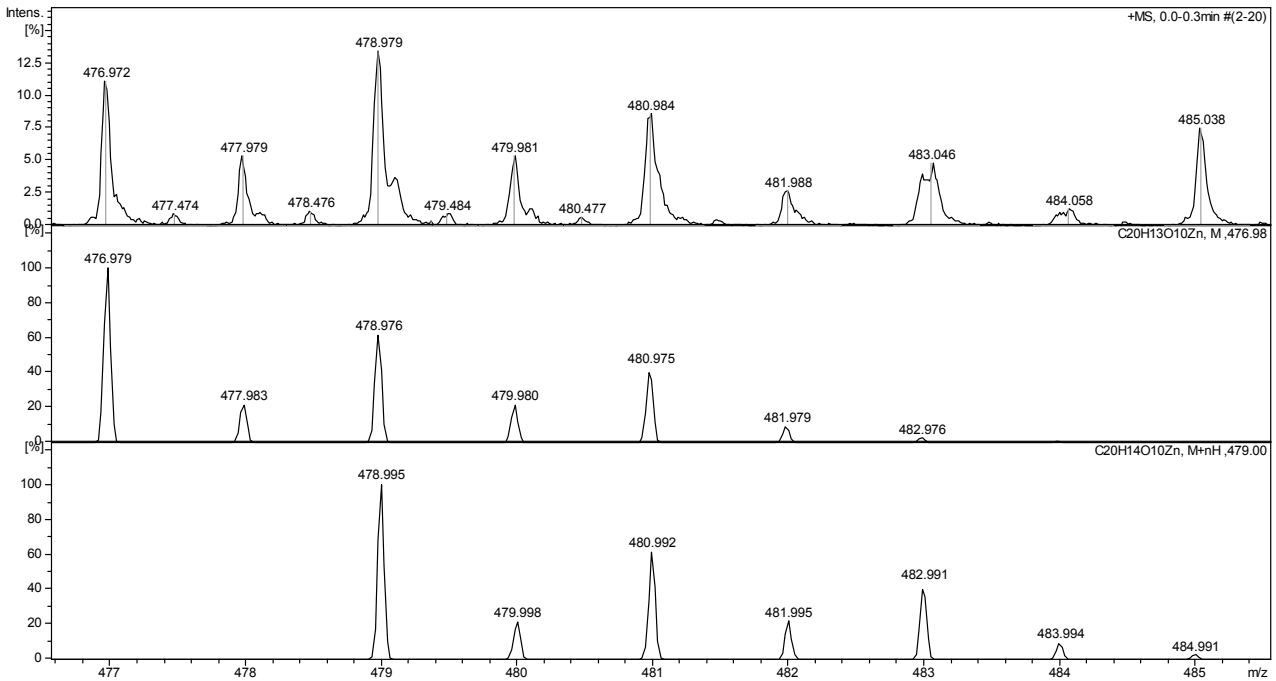

Figure S9. The full spectrum of L12- Zn^{2+} solution in the 1:1 metal-to-ligand molar ratio in negative mode.

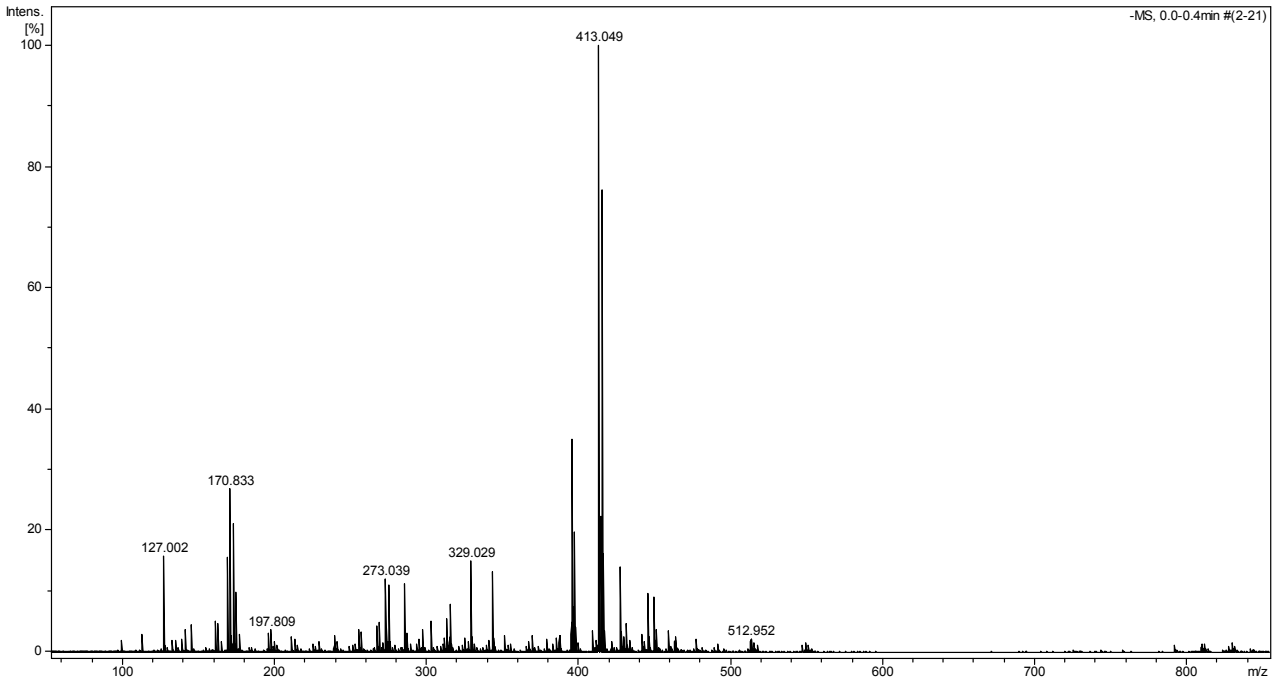

Figure S9A. Experimental data for the peak m/z = 477.096 are shown at the top of the panel and compared with the data calculated for the $[Zn(L12)]^-$ ($C_{20}H_{13}ZnO_{10}$) complex (lower panel).

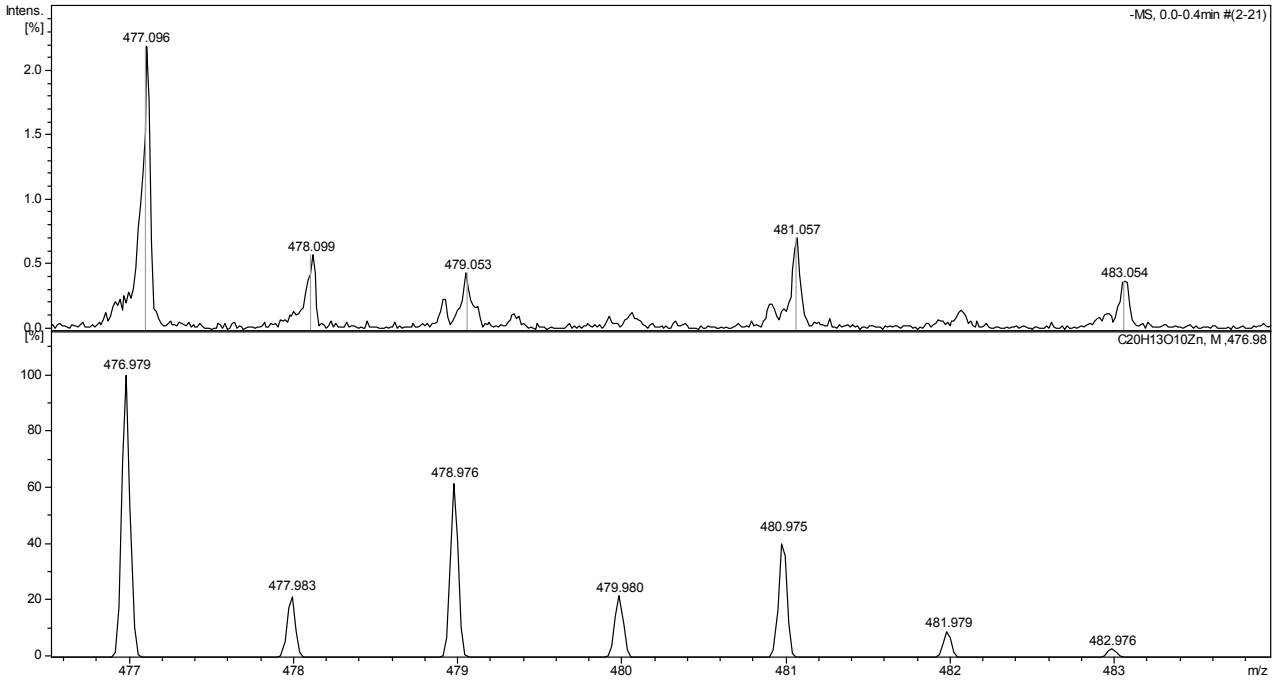

Figure S9B. Experimental data for the peak m/z = 512.952 are shown at the top of the panel and compared with the data calculated for the $[Zn(L12)H+Cl]^-$ ($C_{20}H_{14}ZnClO_{10}$) complex (lower panel).

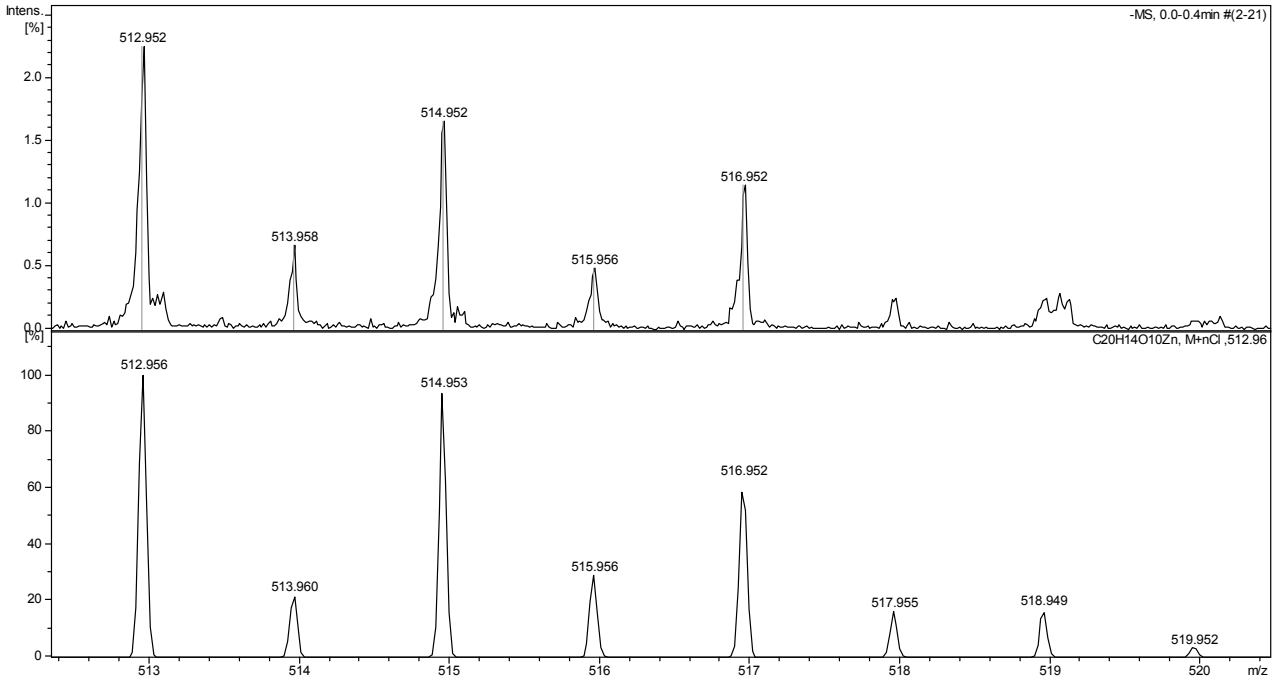

Figure S9C. Experimental data for the peak m/z = 548.921 are shown at the top of the panel and compared with the data calculated for the $[Zn(L12)H_2+2Cl]^-$ ($C_{20}H_{15}ZnCl_2O_{10}$) complex (lower panel).

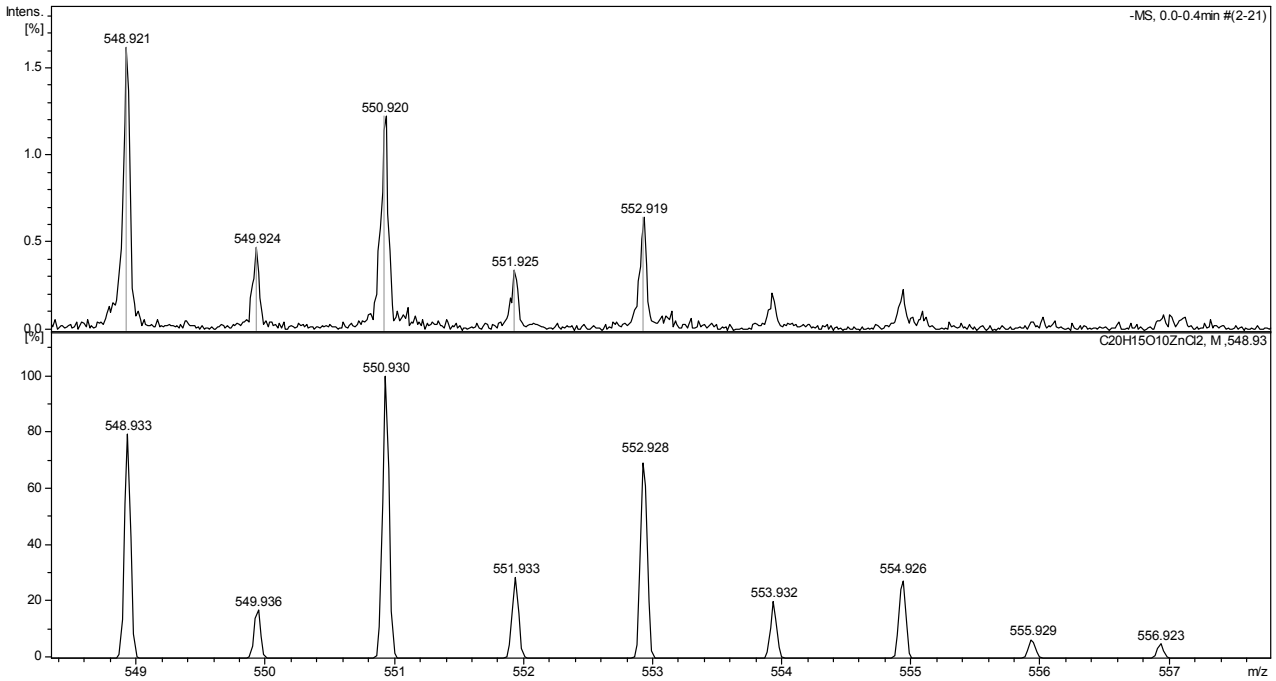

Figure S10. ESI-MS spectrum in positive mode for the L13 compound.

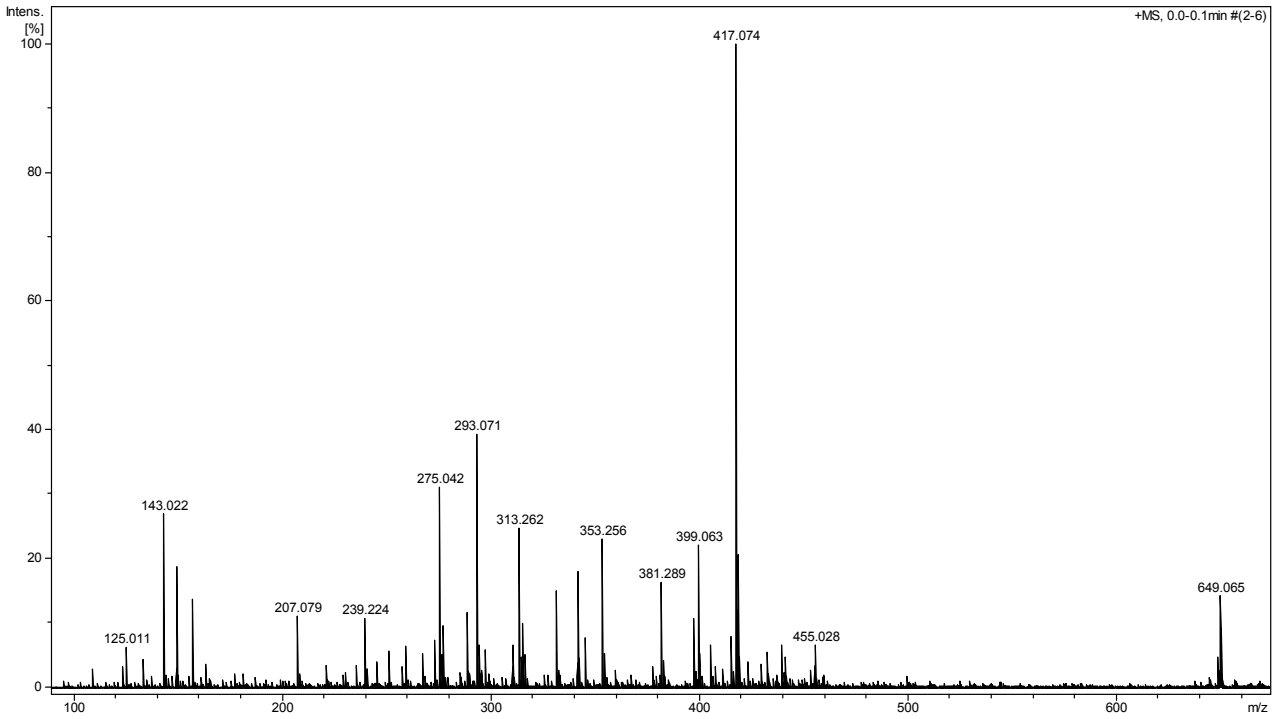

Figure S10A. Experimental data for the peak m/z = 417.074 are shown at the top of the panel and compared with the data calculated for the $[(L13)H_3+H]^+$ ($C_{20}H_{17}O_{10}$) (lower panel).

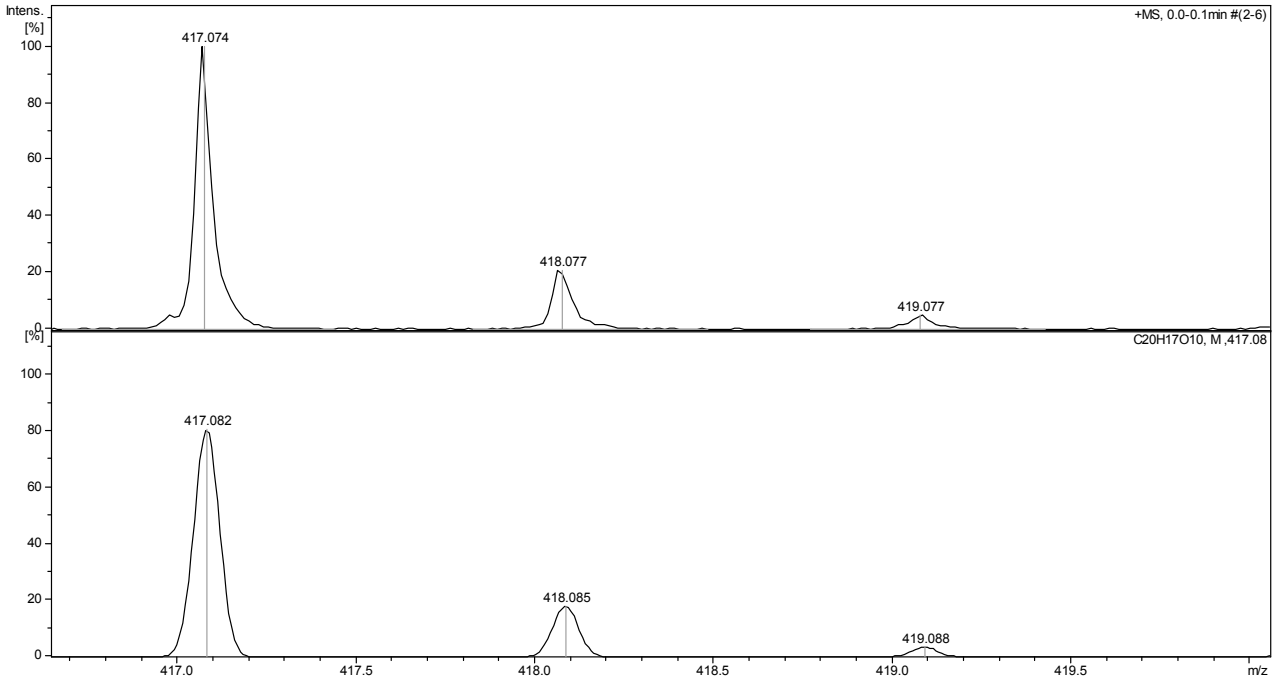

Figure S10B. Experimental data for the peaks m/z = 143.022 and 275.055 are shown at the top of the panel and compared with the data calculated for the ($C_6H_7O_4$) and ($C_{14}H_{11}O_6$) fragments (lower panels).

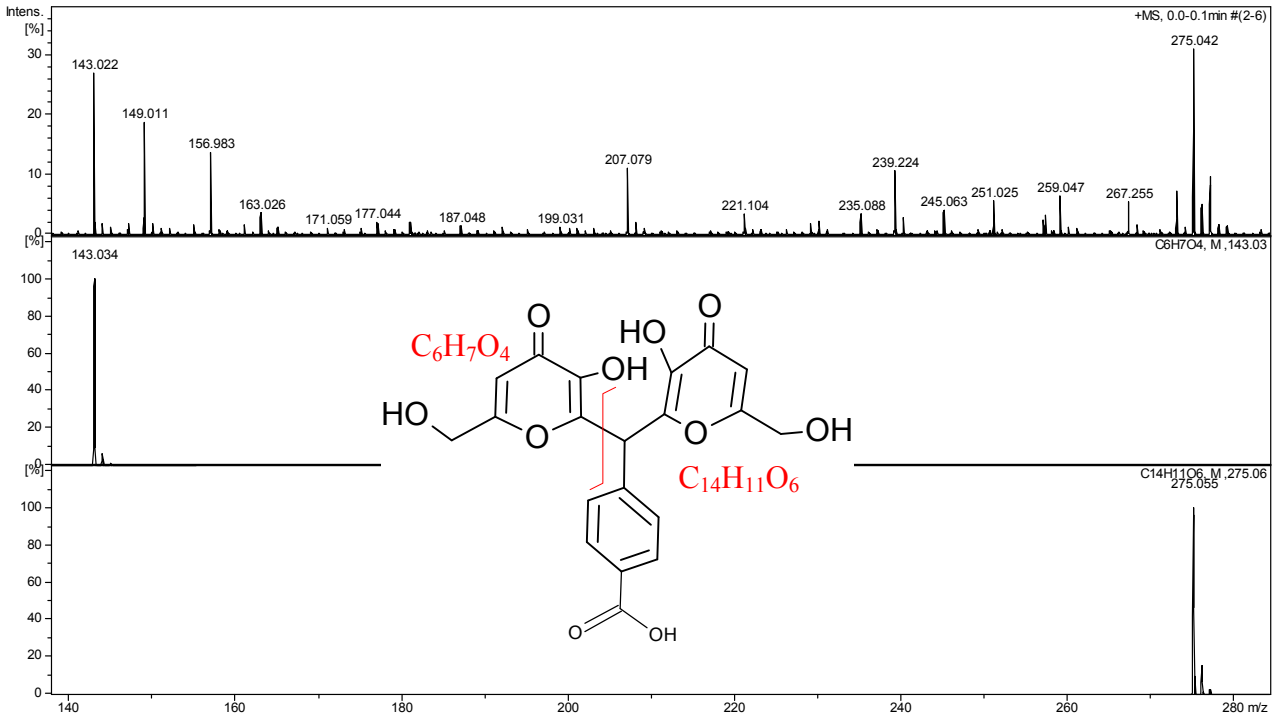

Figure S11. ESI-MS spectrum in negative mode for the L13 compound.

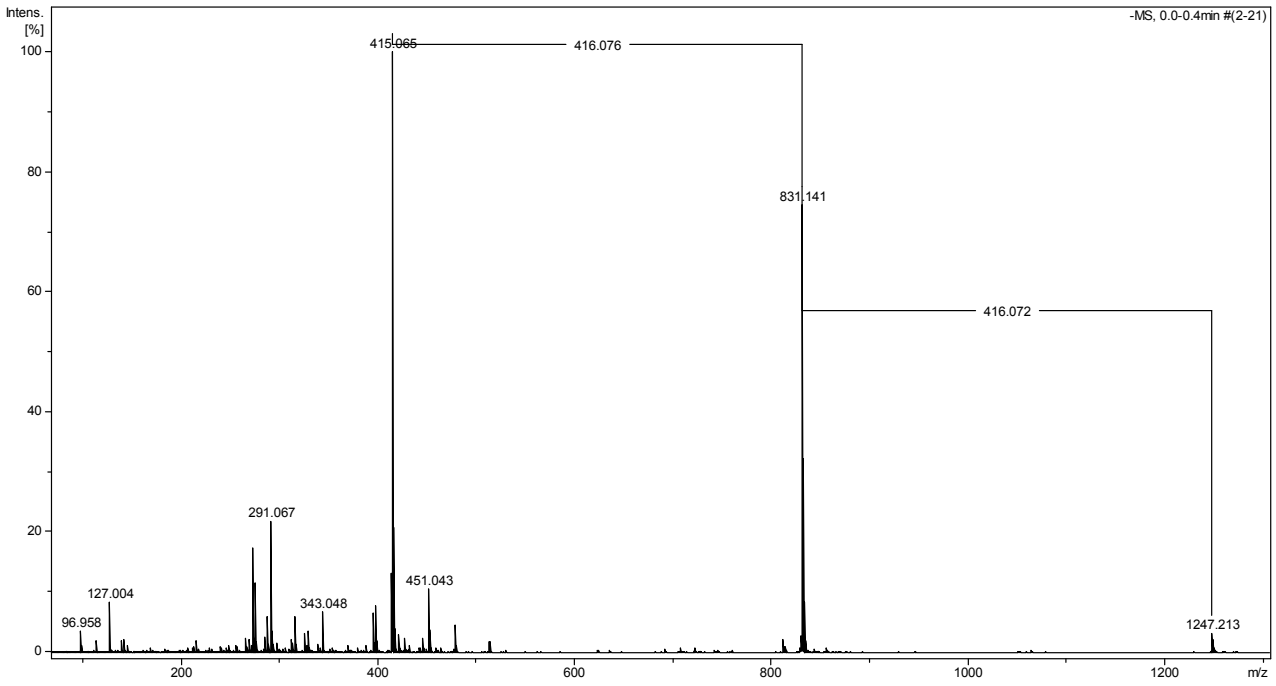

Figure S11A. Experimental data for the peak m/z = 415.065 are shown at the top of the panel and compared with the data calculated for the $[(L13)H_2]^-$ ($C_{20}H_{15}O_{10}$) (lower panel).

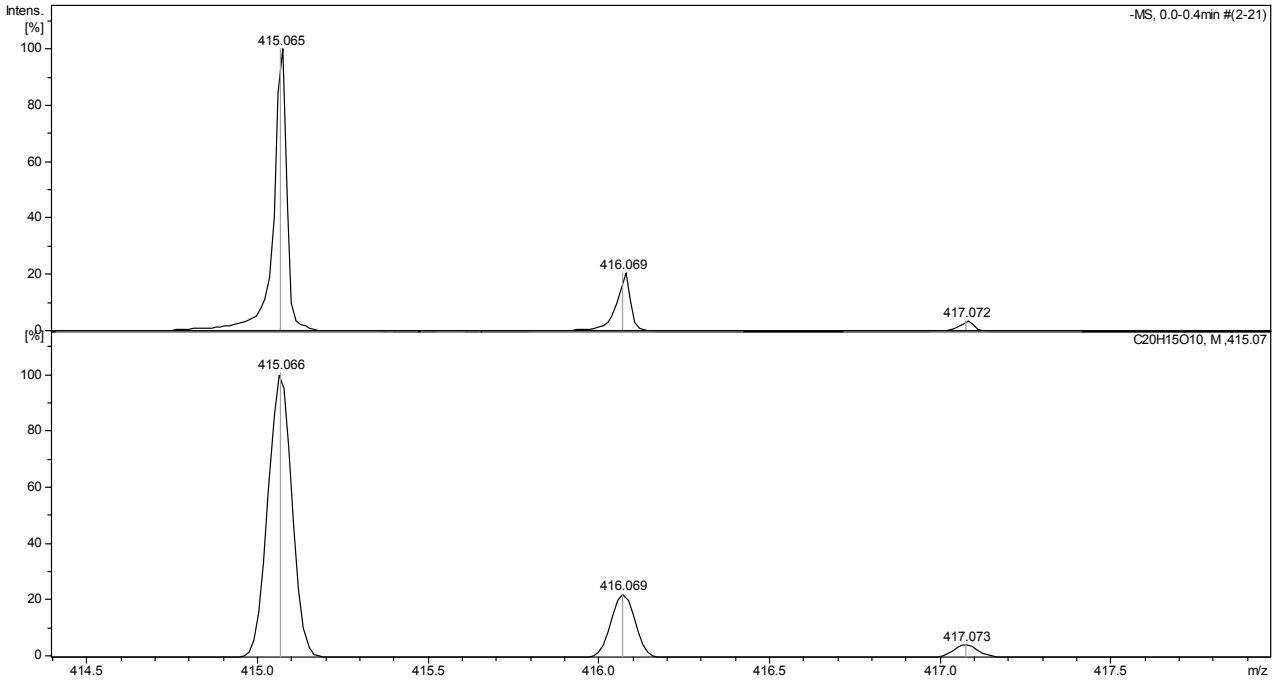

Figure S11B. Experimental data for the peak m/z = 831.141 are shown at the top of the panel and compared with the data calculated for the $[(L13)_2H_5]^-$ ($C_{40}H_{31}O_{20}$) (lower panel).

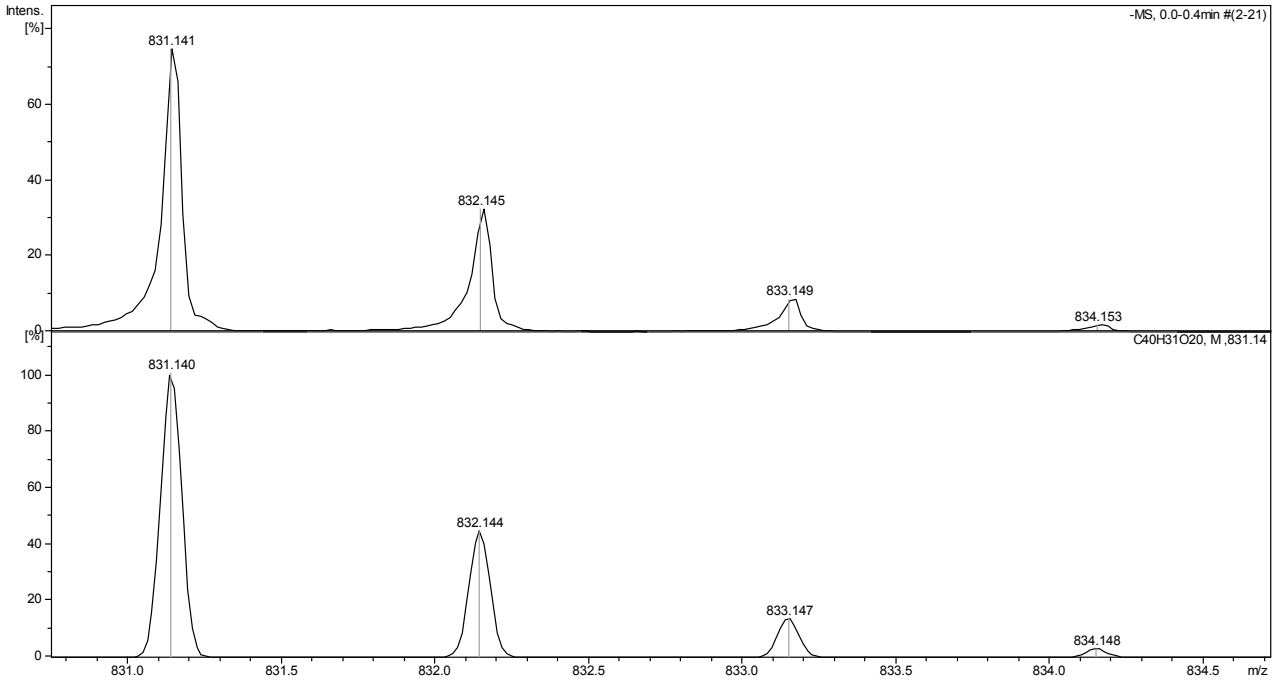

Figure S11C. Experimental data for the peak m/z = 1247.213 are shown at the top of the panel and compared with the data calculated for the $[(L13)_3H_8]^-$ ($C_{60}H_{47}O_{30}$) (lower panel).

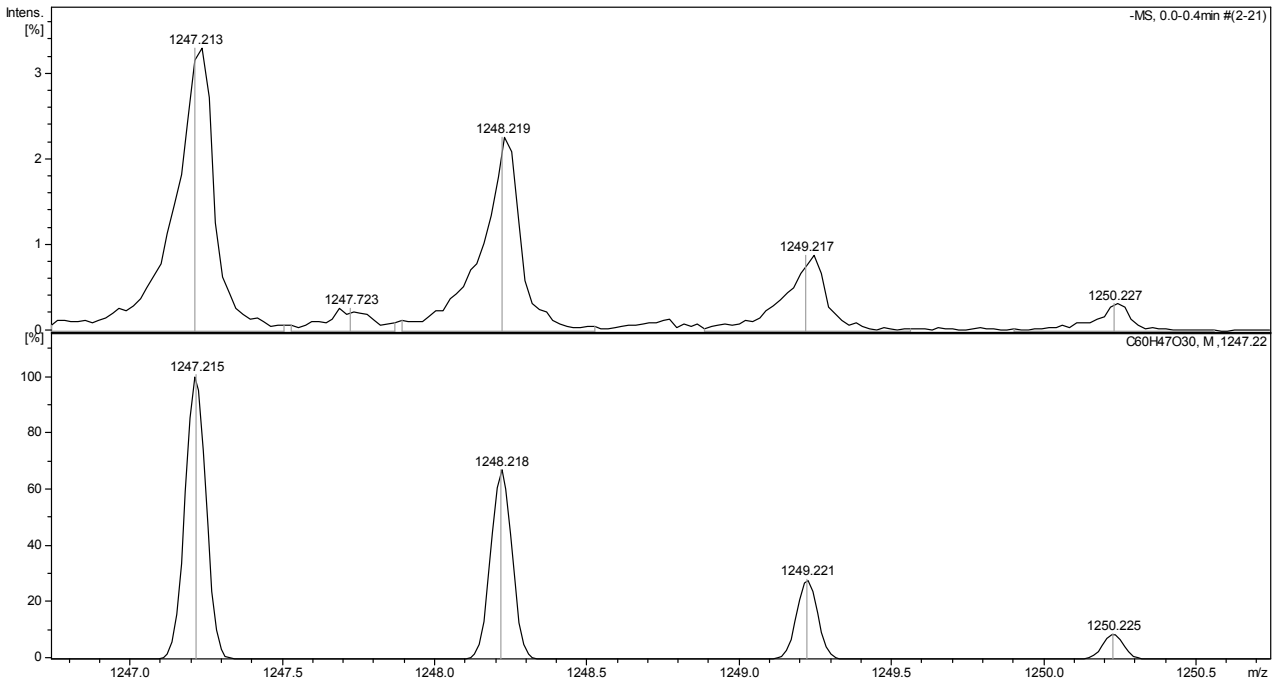

Figure S12. The full spectrum of L13-Al^{3+} solution in the 1:1 metal-to-ligand molar ratio in positive mode.

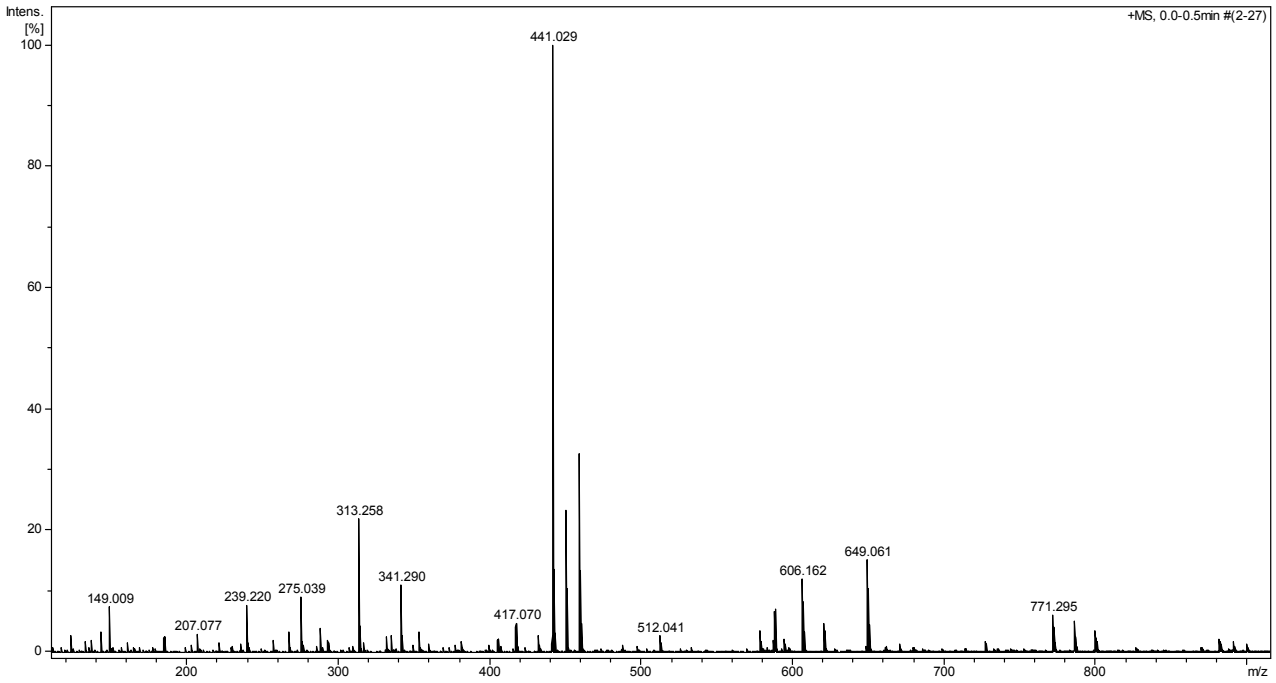

Figure S12A. Experimental data for the peaks m/z = 441.029 and 459.040 are shown at the top of the panel and compared with the data calculated for the $[Al_2(L13)_2H_2]^{2+}$ ($C_{40}H_{28}Al_2O_{20}$) and $[Al_2(L13)_2H_2+2H_2O]^{2+}$ ($C_{40}H_{32}Al_2O_{22}$) complexes (lower panels).

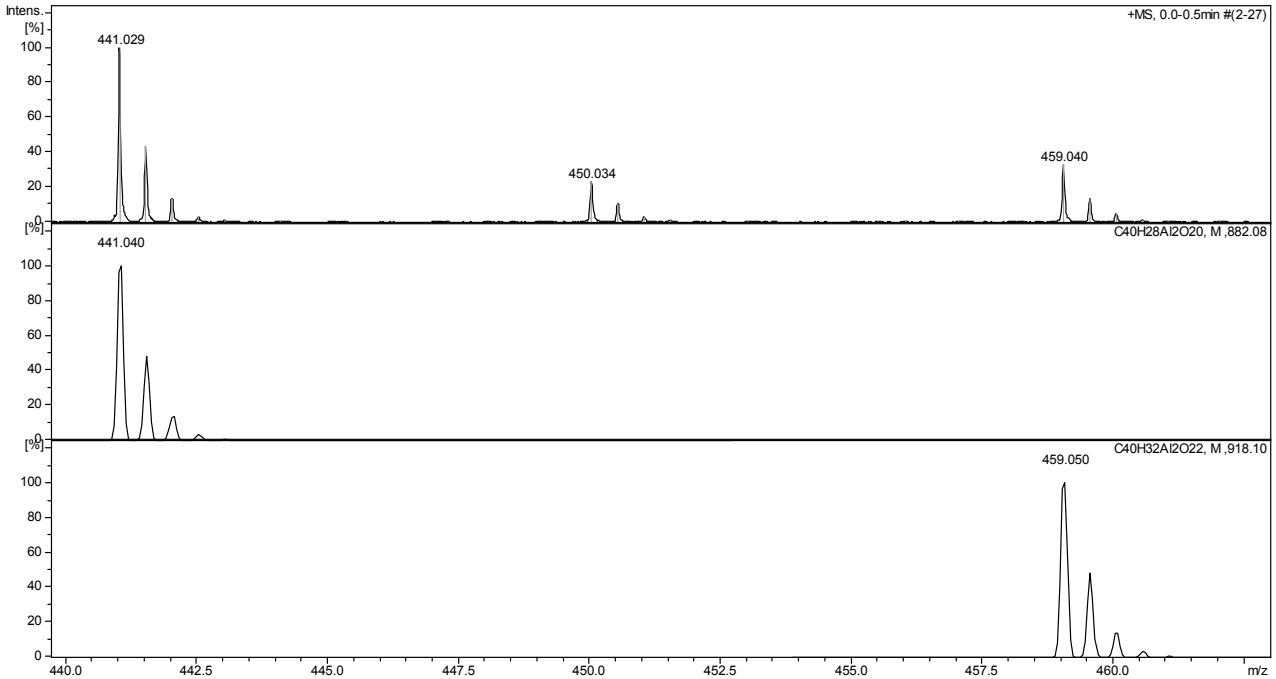

Figure S13. Electrospray ionization with tandem mass spectrometry (MS/MS) spectrum of the $[Al_2(L13)_2H_2]^{2+}$ complex. The peak selected for fragmentation in the MS/MS experiment is indicated by a diamond.

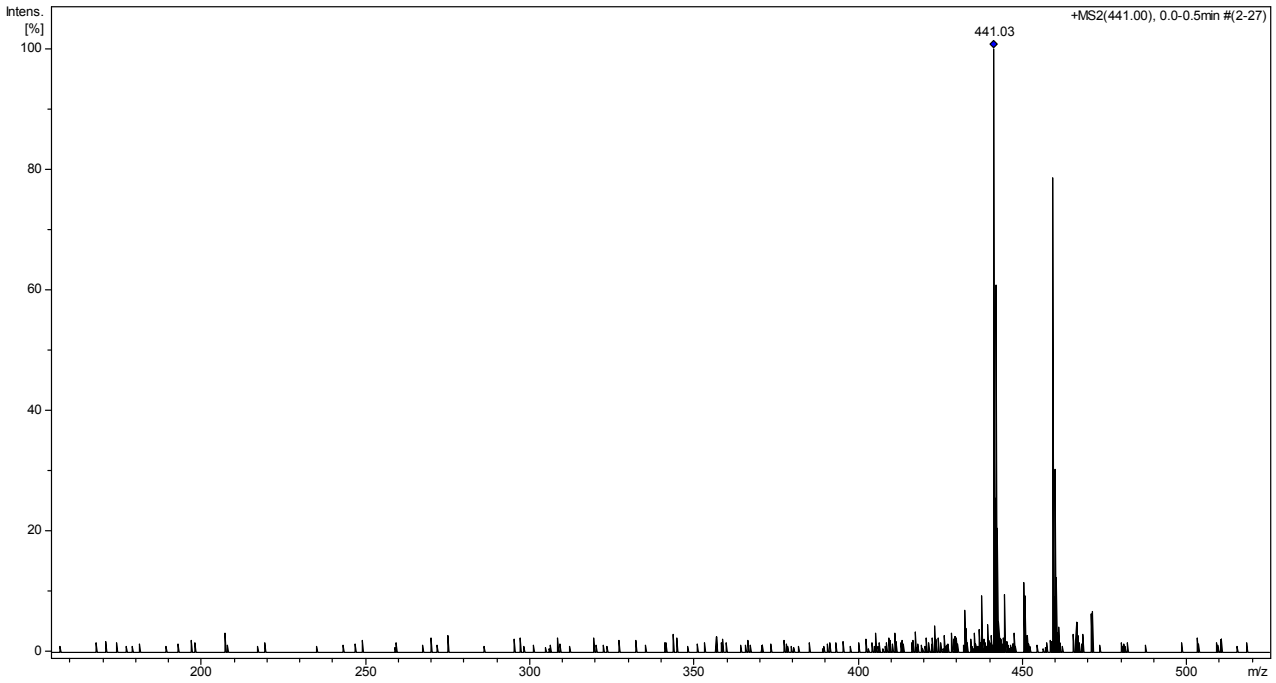

Figure S13A. Experimental data for the peak m/z = 459.05 are shown at the top of the panel and compared with the data calculated for the $[Al(L13)H+H_2O]^+$ ($C_{20}H_{16}AlO_{11}$) complex (lower panel).

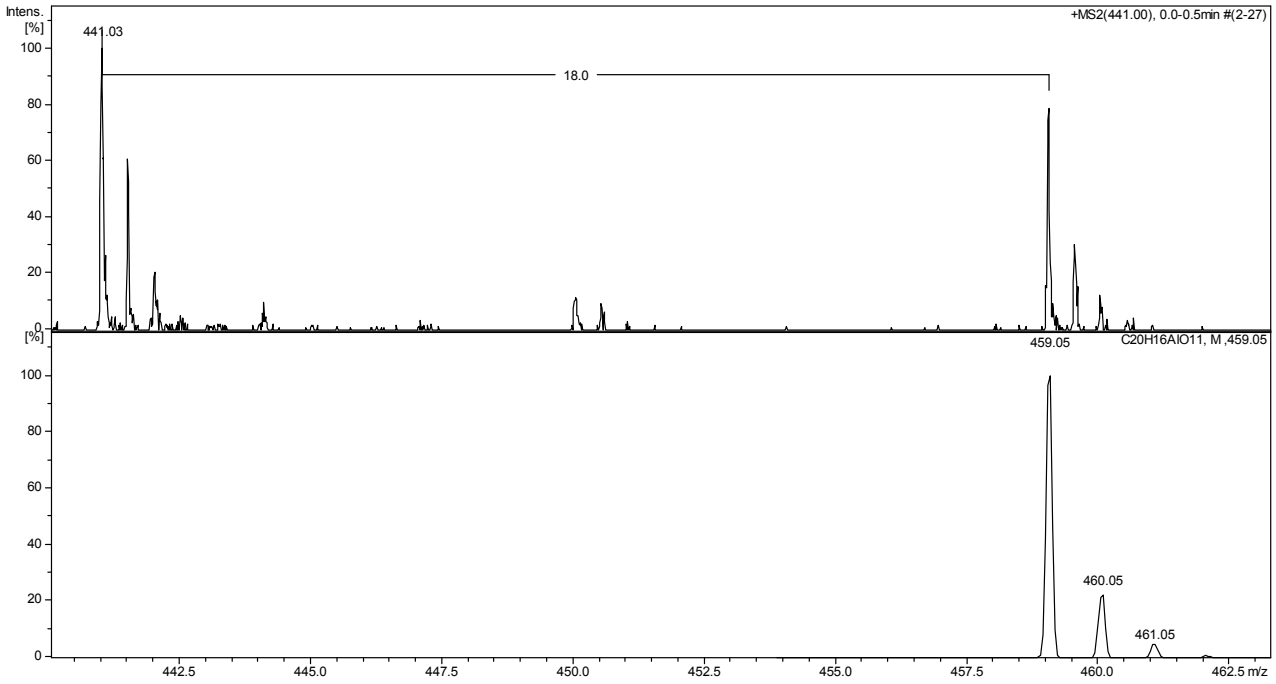

Figure S14. The full spectrum of L13-Cu^{2+} solution in the 1:1 metal-to-ligand molar ratioin positive mode.

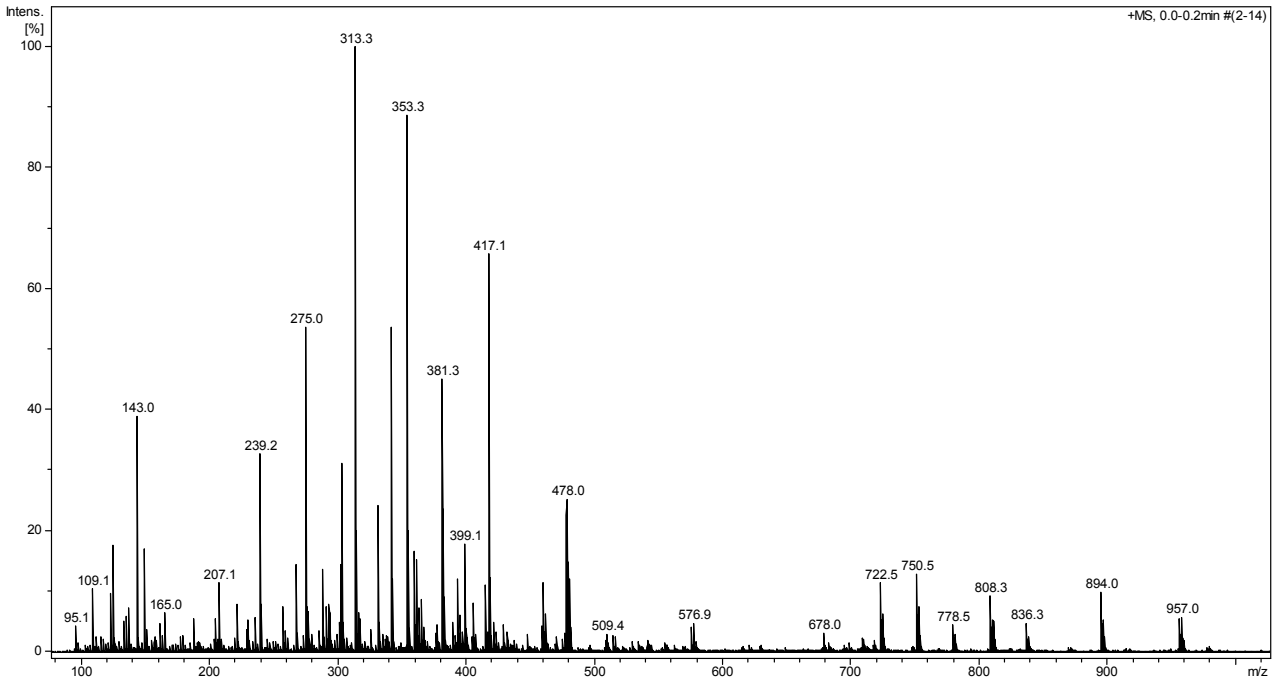

Figure S14A. Experimental data for the peak m/z = 477.986 are shown at the top of the panel and compared with the data calculated for the $[Cu(L13)H_2]^+$ ($C_{20}H_{15}CuO_{10}$) and $[Cu_2(L13)_2H_4]^{2+}$ ($C_{40}H_{30}Cu_2O_{20}$) complexes (lower panels).

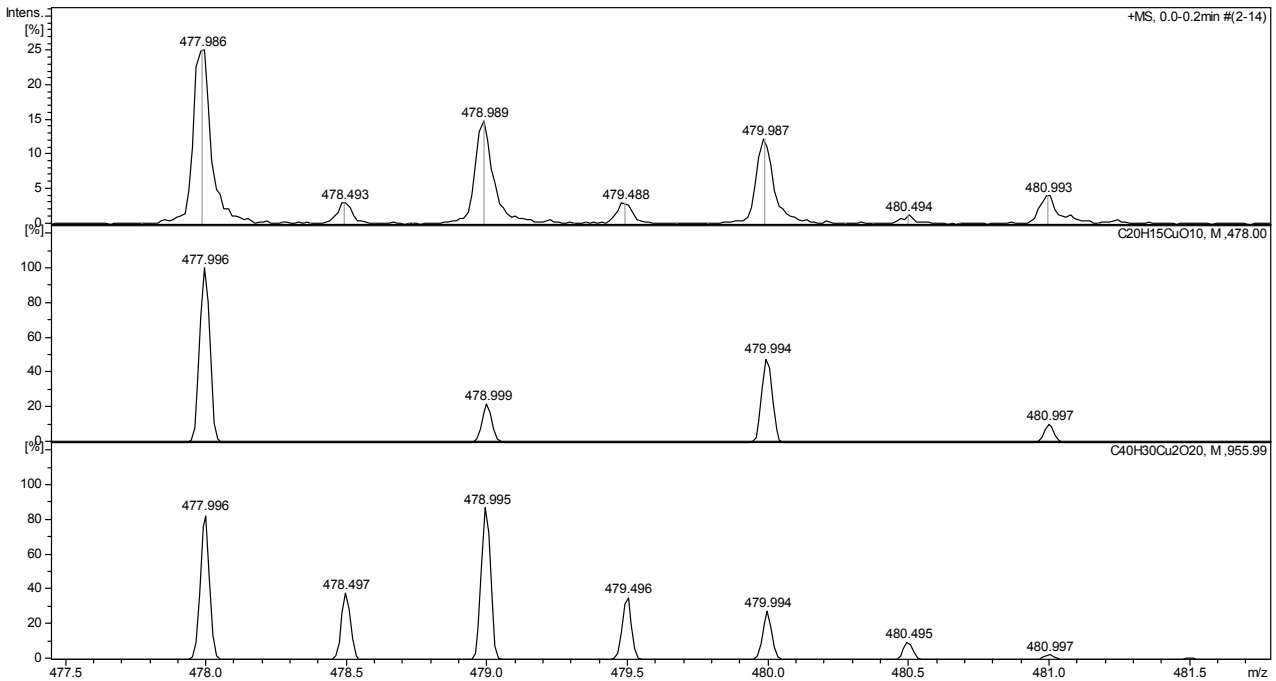

Figure S14B. Experimental data for the peak m/z = 954.960 are shown at the top of the panel and compared with the data calculated for the $[Cu_2(L13)_2H]^+$ ($C_{40}H_{29}Cu_2O_{20}$) complex (lower panel).

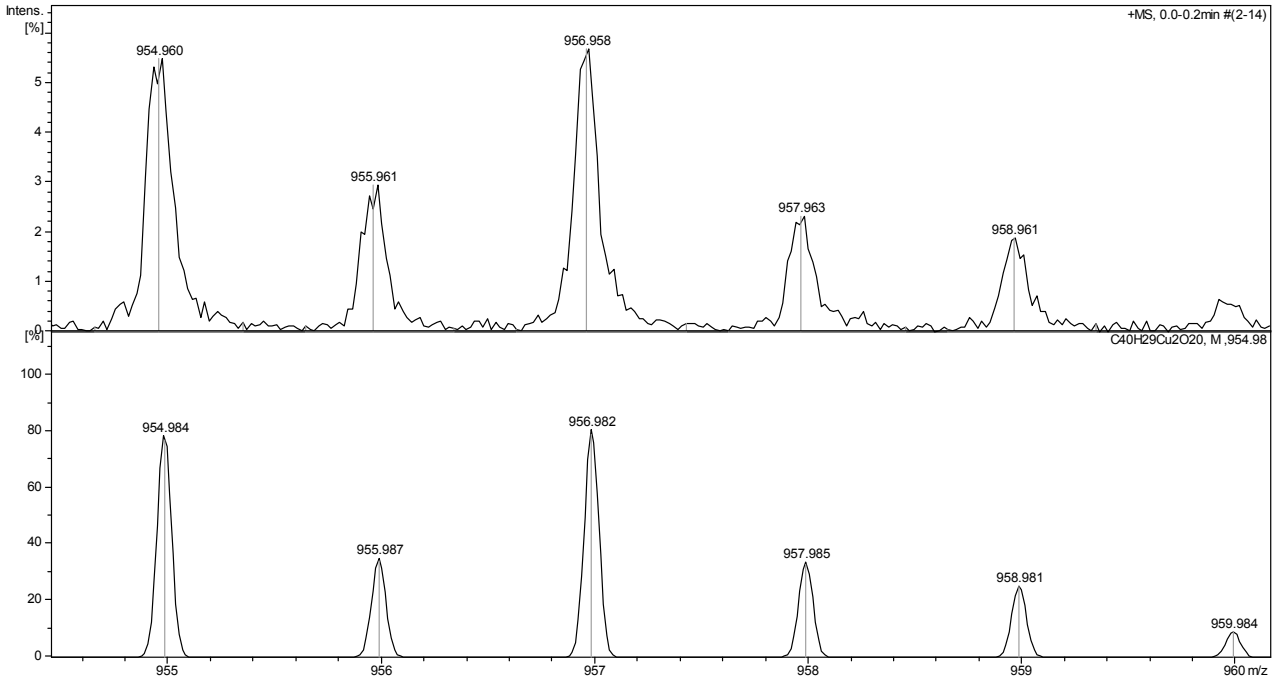

Figure S15. The full spectrum of L13-Fe^{3+} solution in the 1:1 metal-to-ligand molar ratioin positive mode.

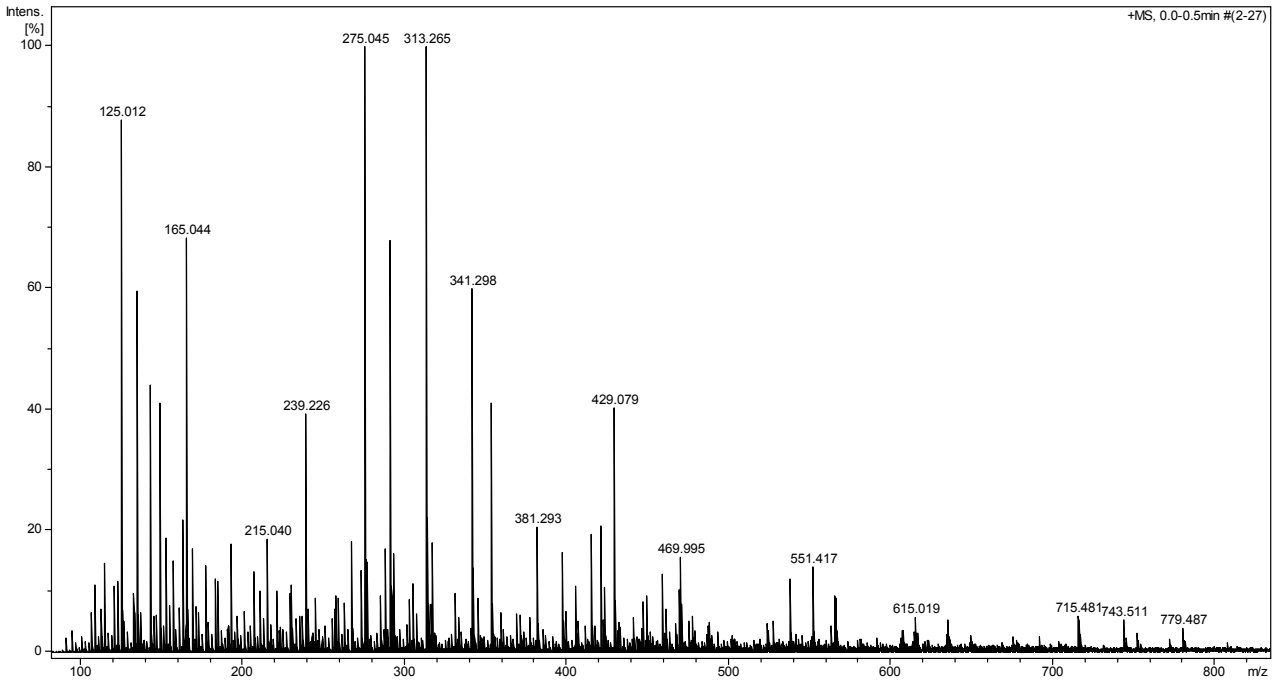

Figure S15A. Experimental data for the peaks m/z = 469.995, 478.998 and 488.004 are shown at the top of the panel and compared with the data calculated for the $[Fe_2(L13)_2H_2]^{2+}$ ($C_{40}H_{28}Fe_2O_{20}$), $[Fe_2(L13)_2H_2+H_2O]^{2+}$ ($C_{40}H_{30}Fe_2O_{21}$) and $[Fe_2(L13)_2H_2+2H_2O]^{2+}$ ($C_{40}H_{32}Fe_2O_{22}$) complexes (lower panels).

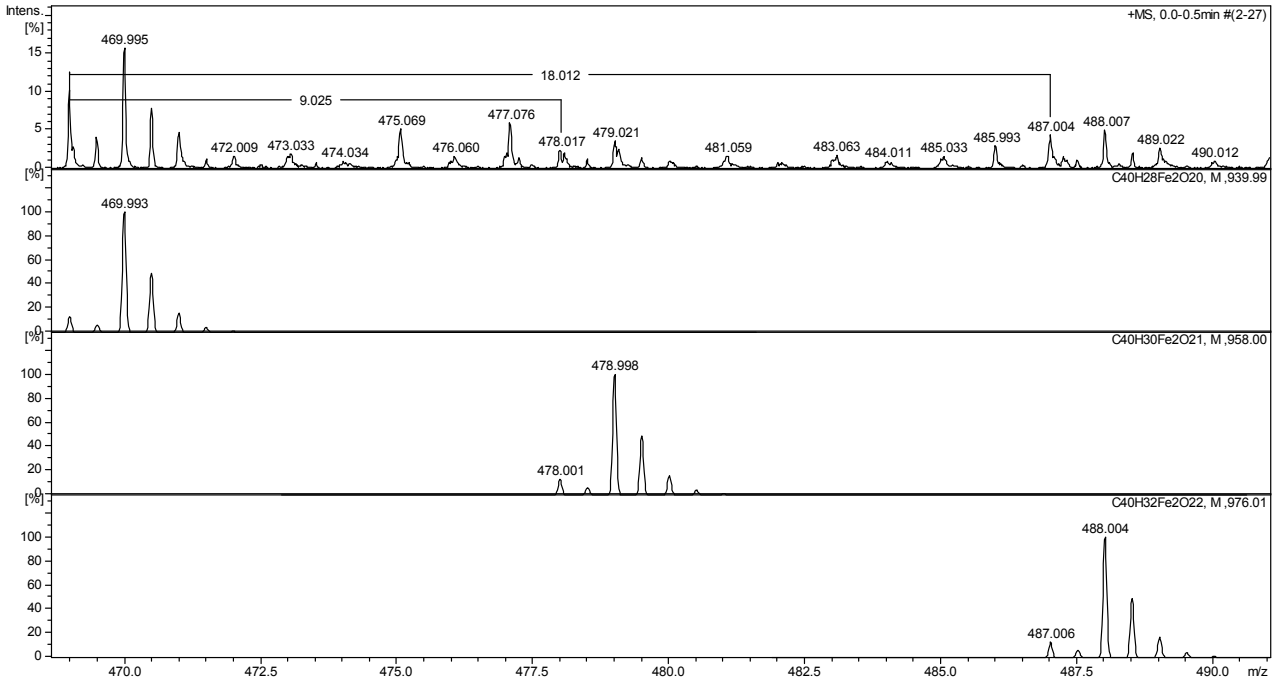

Figure S16. The full spectrum of L13-Zn^{2+} solution in the 1:1 metal-to-ligand molar ratio in positive mode.

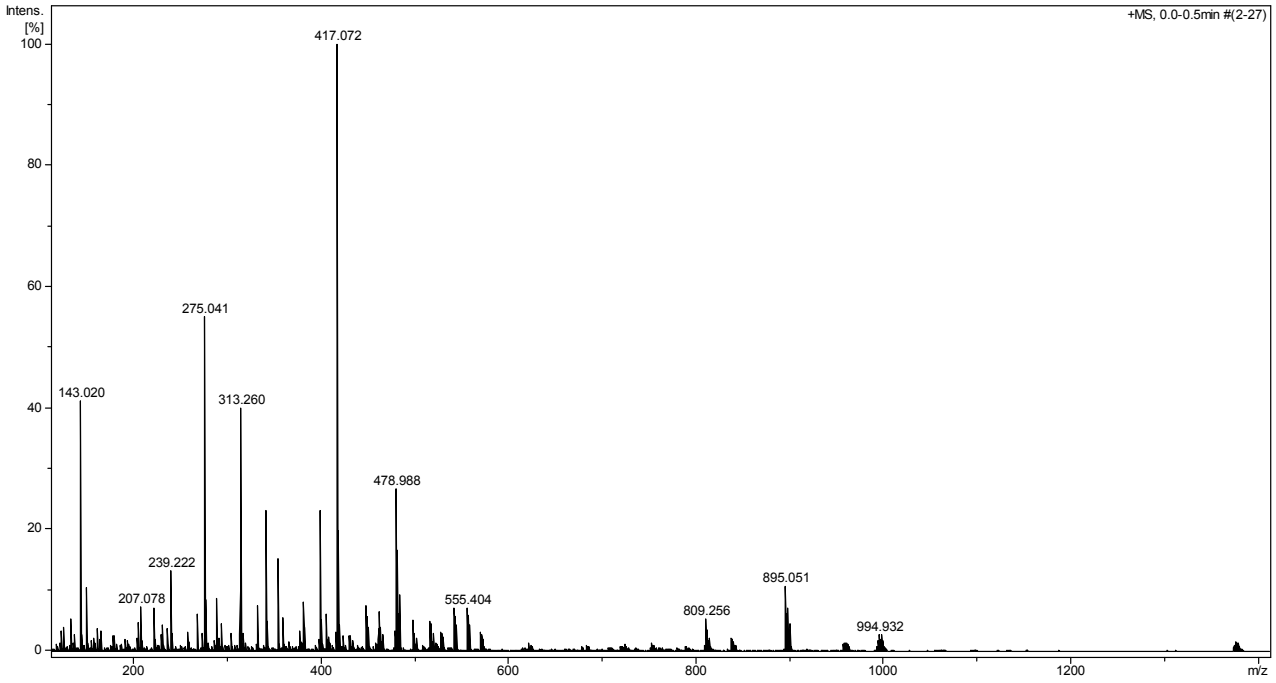

Figure S16A. Experimental data for the peak m/z = 478.988 are shown at the top of the panel and compared with the data calculated for the $[Zn_2(L13)_2H_4]^{2+}$ ($C_{40}H_{30}Zn_2O_{20}$) and $[Zn(L13)H_2]^{+}$ ($C_{20}H_{15}ZnO_{10}$) complexes (lower panels).

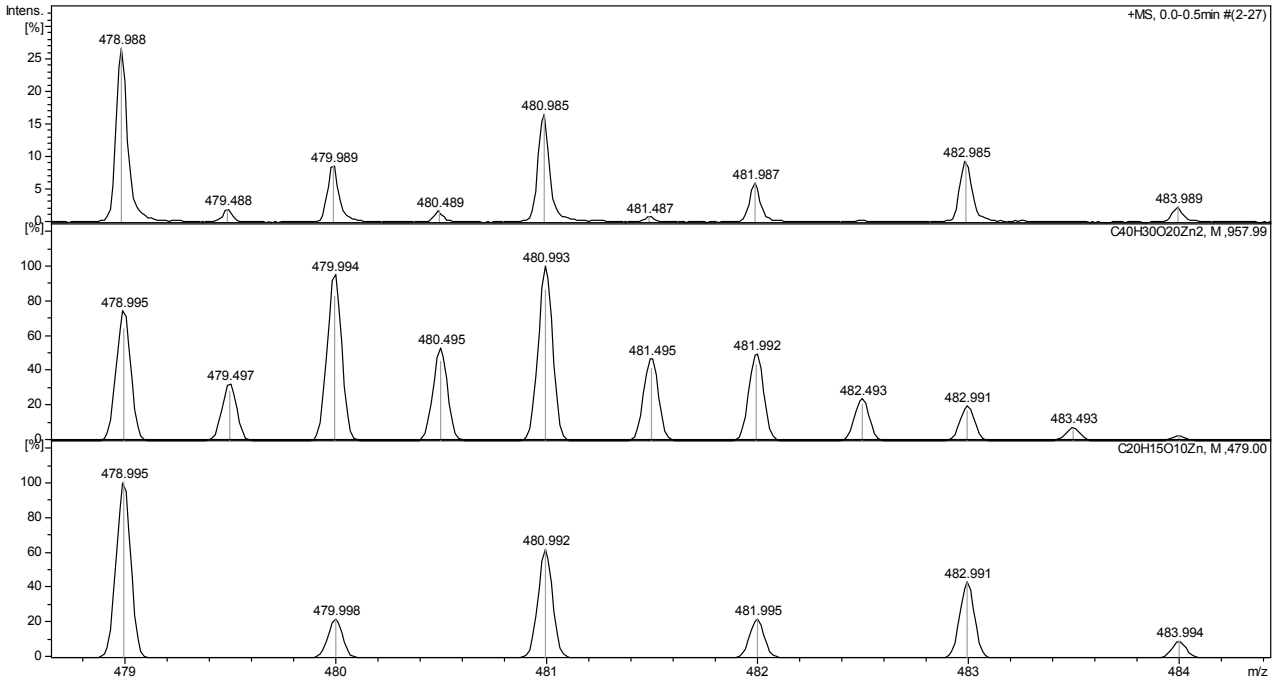

Figure S16B. Experimental data for the peaks m/z = 496.998 and 514.977 are shown at the top of the panel and compared with the data calculated for the $[Zn(L13)H_2+H_2O]^+$ ($C_{20}H_{17}ZnO_{11}$) and $[Zn(L13)H_2+2H_2O]^+$ ($C_{20}H_{19}ZnO_{12}$) complexes (lower panels).

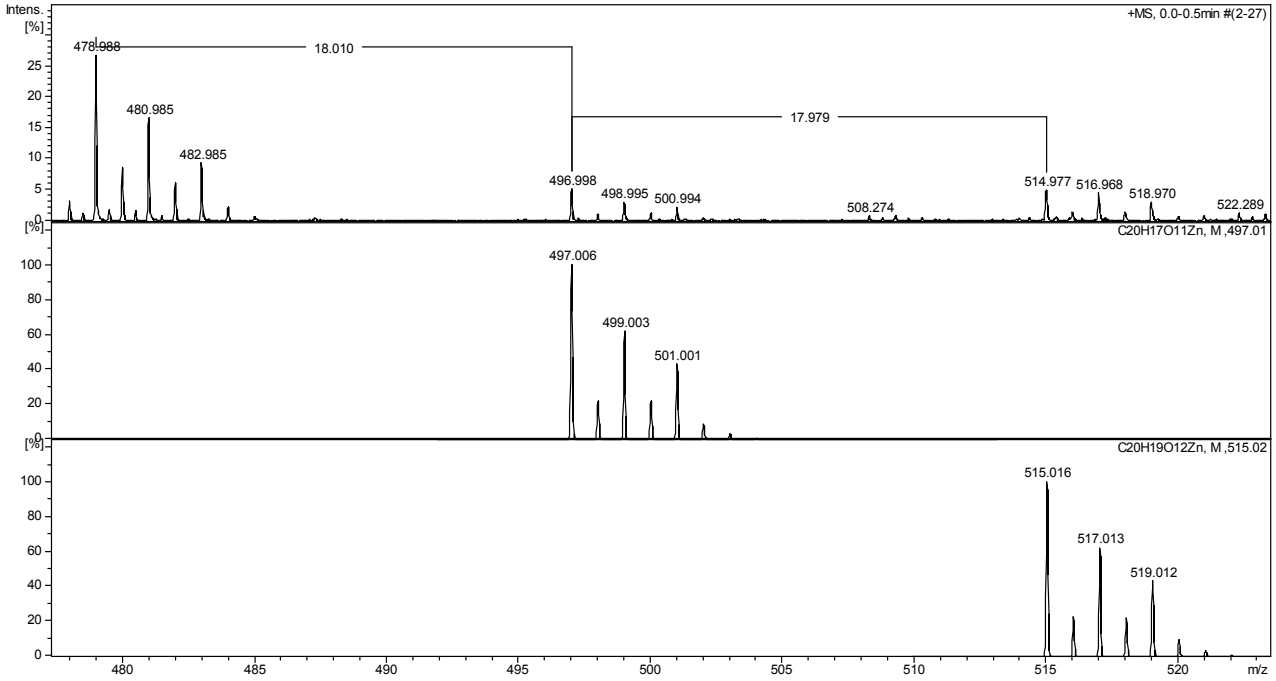

Figure S16C. Experimental data for the peak m/z = 956.964 are shown at the top of the panel and compared with the data calculated for the $[Zn_2(L13)_2H]^+$ ($C_{40}H_{29}Zn_2O_{20}$) (lower panel).

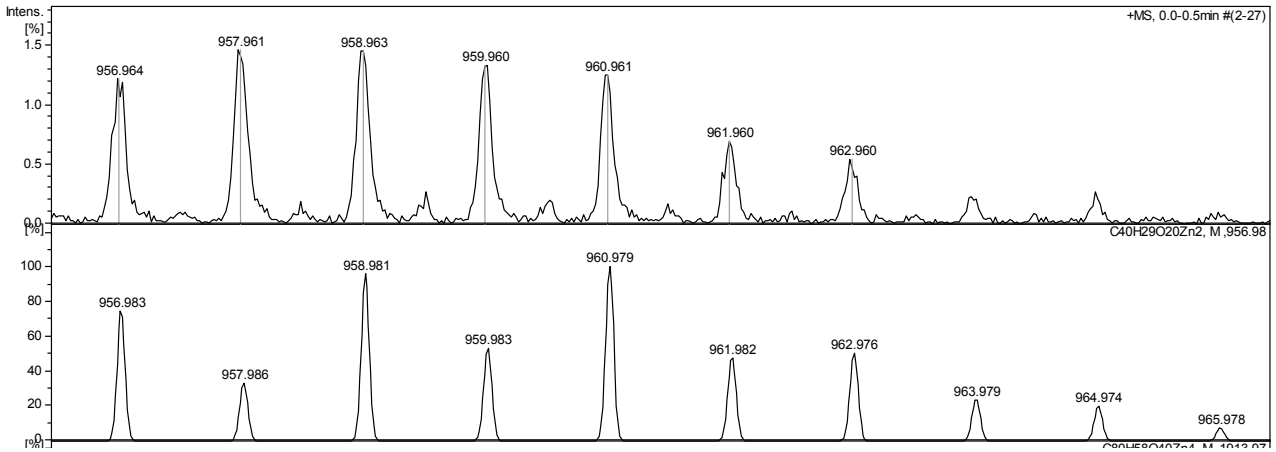

Figure S17. ESI-MS spectrum in positive mode for the L14 compound.

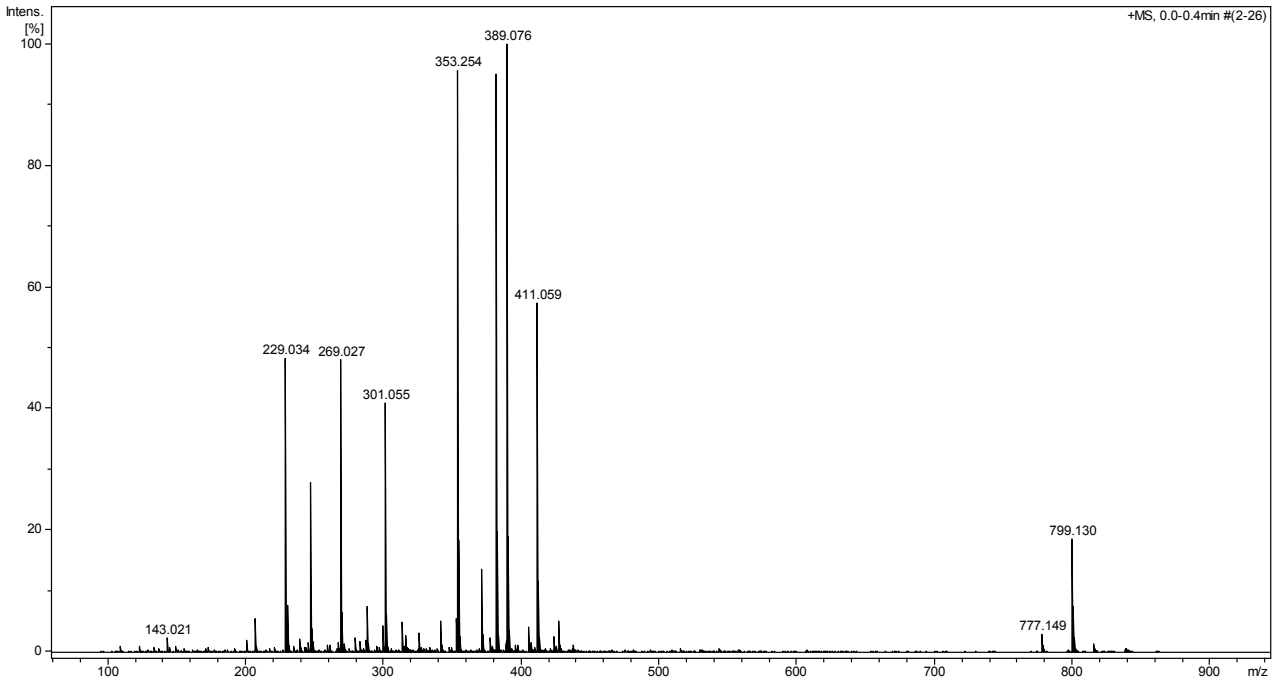

Figure S17A. Experimental data for the peaks m/z = 389.076, 411.059 and 427.033 are shown at the top of the panel and compared with the data calculated for the $[(L14)H_3+H]^+$ ($C_{19}H_{16}O_{10}$), $[(L14)H_3+Na]^+$ ($C_{19}H_{16}O_9Na$) and the $[(L14)H_3+K]^+$ ($C_{19}H_{16}O_9K$) (lower panels).

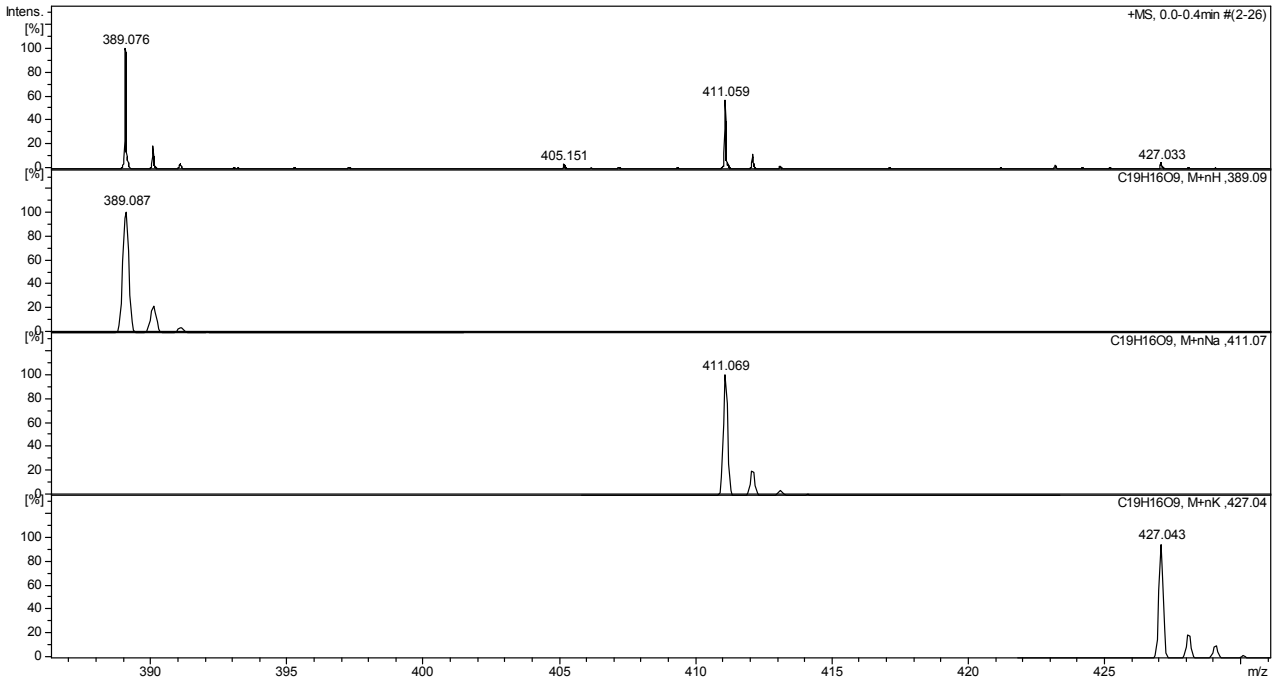

Figure S17B. Experimental data for the peaks m/z = 143.021 and 247.045 are shown at the top of the panel and compared with the data calculated for the ($C_6H_7O_4$) and ($C_{13}H_{11}O_5$) fragments (lower panels).

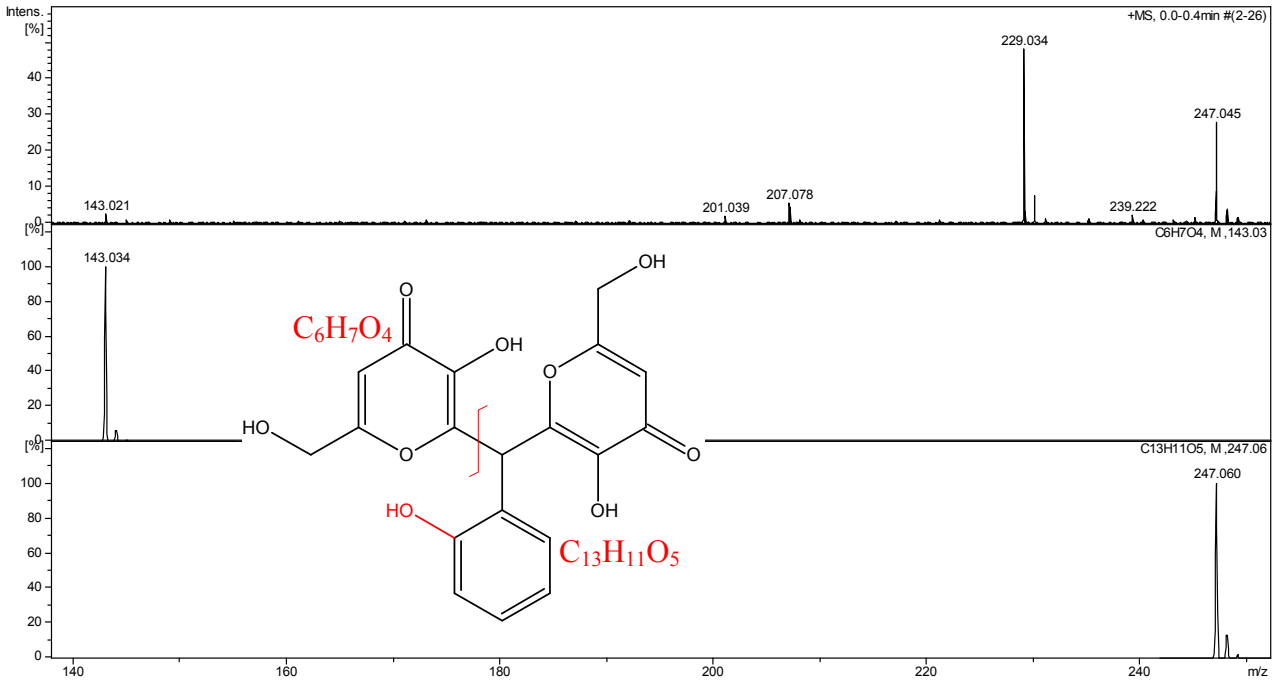

Figure S17C. Experimental data for the peak m/z = 799.130 are shown at the top of the panel and compared with the data calculated for the $[(L14)_2H_6+Na]^+$ ($C_{38}H_{32}O_{18}Na$) (lower panel).

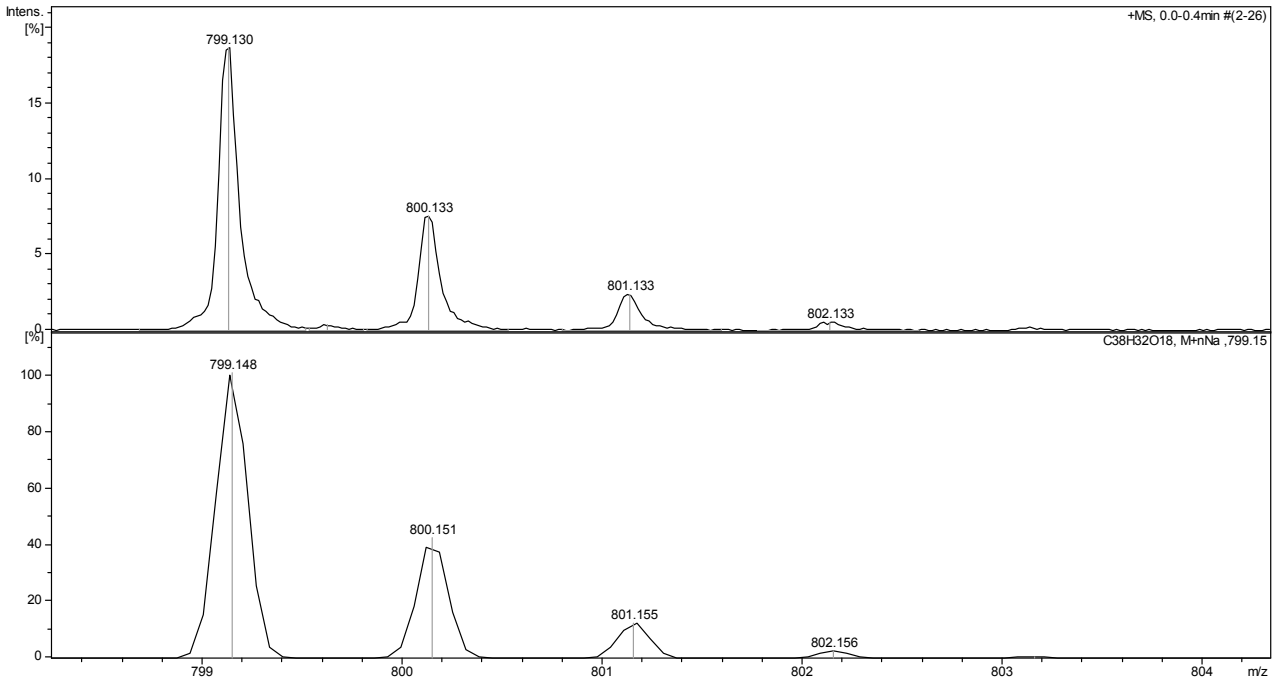

Figure S18. ESI-MS spectrum in negative mode for the L14 compound.

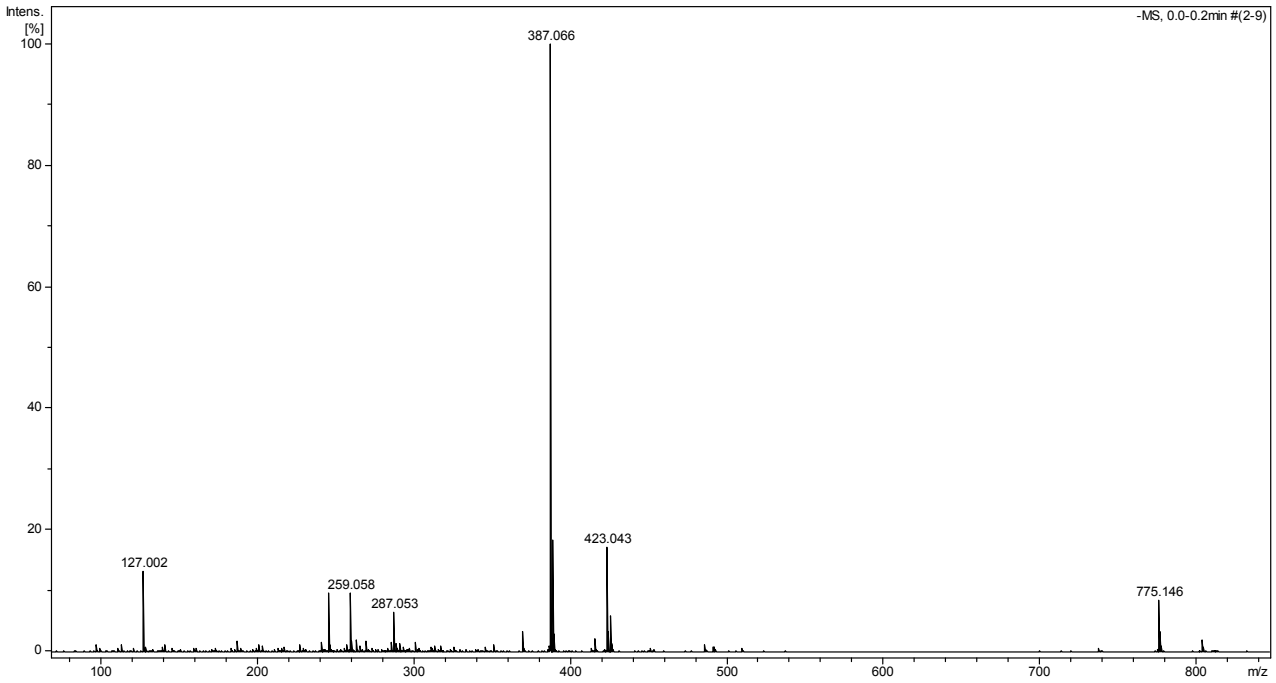

Figure S18A. Experimental data for the peaks m/z = 387.066 and 423.043 are shown at the top of the panel and compared with the data calculated for the $[(L14)H_2]^-$ ($C_{19}H_{15}O_9$) and $[(L14)H_3+Cl]^-$ ($C_{19}H_{16}O_9Cl$) (lower panels).

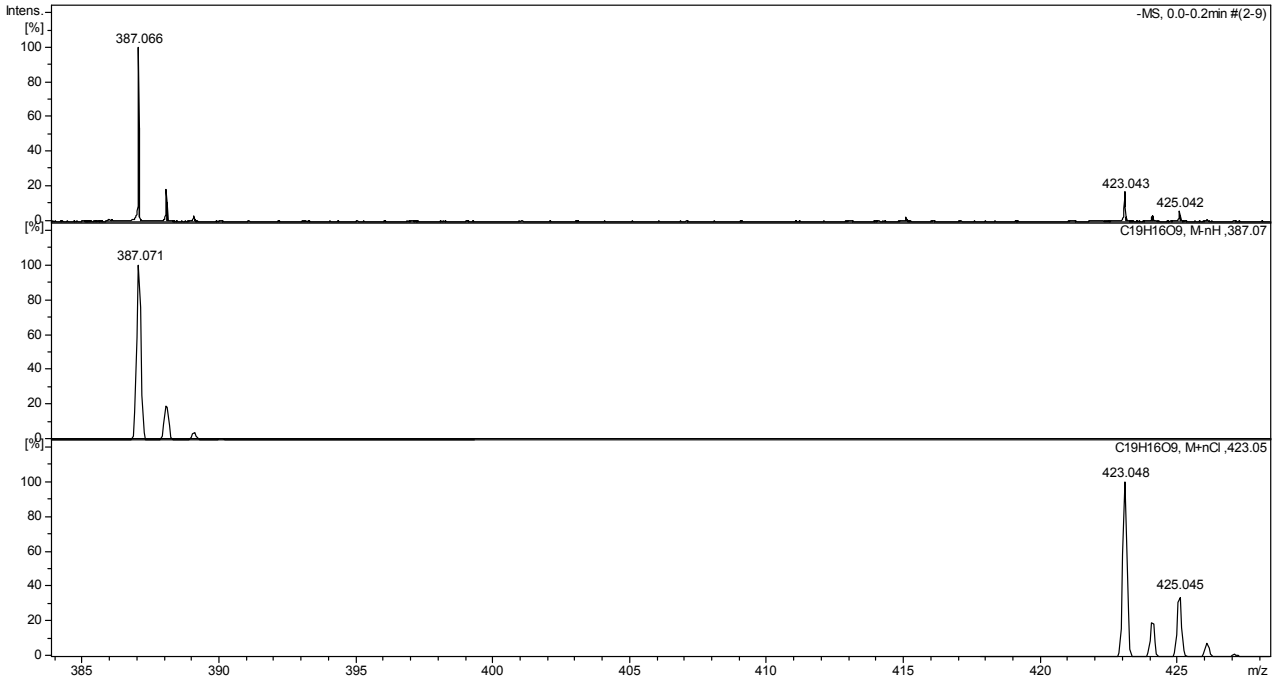

Figure S19. The full spectrum of L14-Al^{3+} solution in the 1:1 metal-to-ligand molar ratioin positive mode.

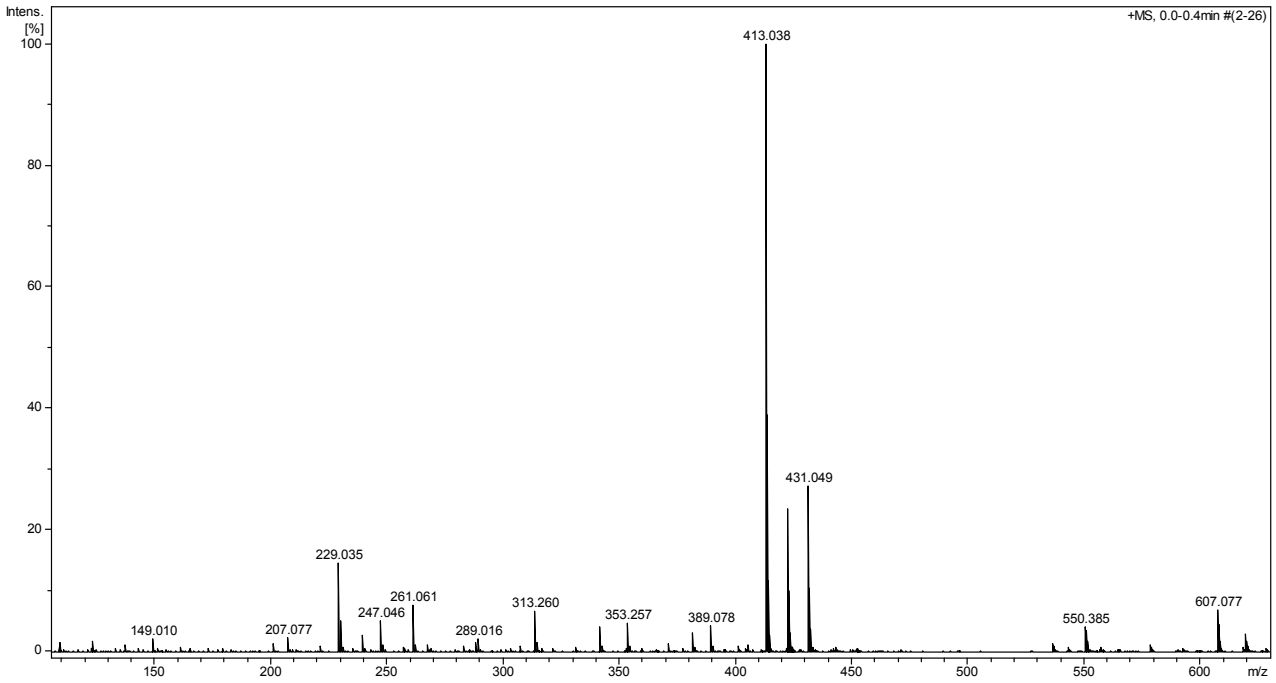

Figure S19A. Experimental data for the peaks m/z = 413.038, 422.044 and 431.049 are shown at the top of the panel and compared with the data calculated for the $[Al_2(L14)_2H_2]^{2+}$ ($C_{38}H_{28}Al_2O_{18}$), $[Al_2(L14)_2H_2+H_2O]^{2+}$ ($C_{38}H_{30}Al_2O_{19}$) and $[Al_2(L14)_2H_2+2H_2O]^{2+}$ ($C_{38}H_{32}Al_2O_{20}$) complexes (lower panels).

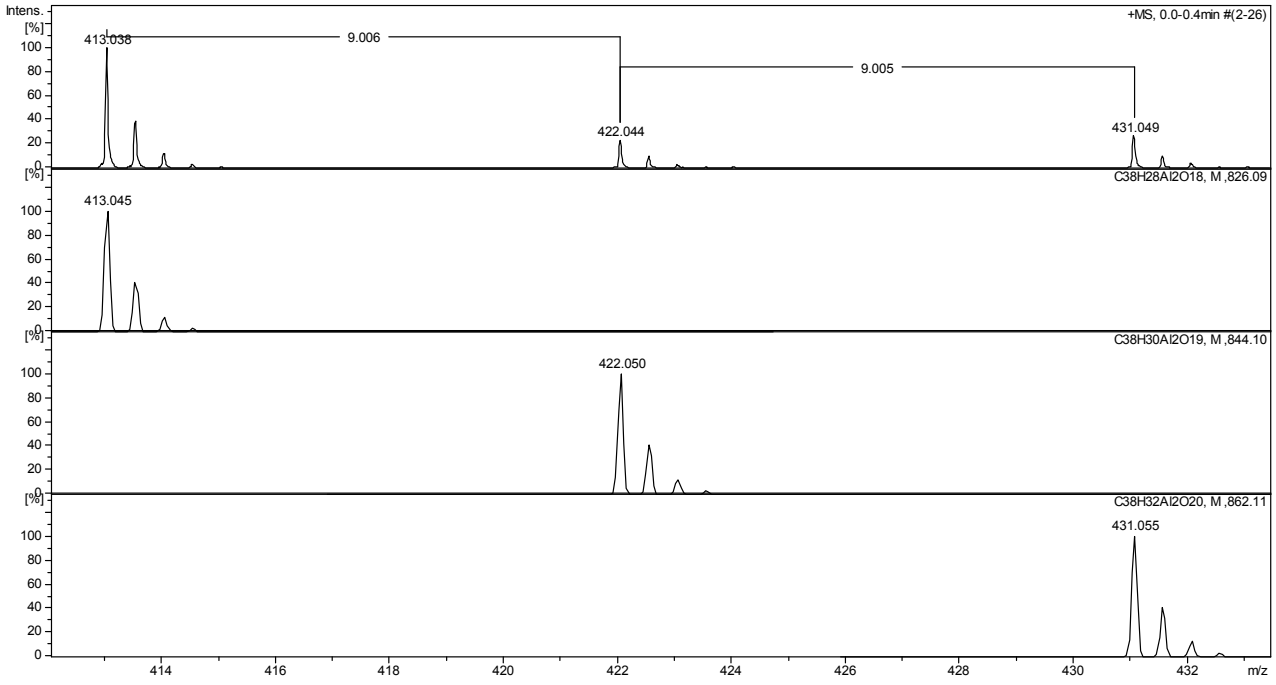

Figure S19B. Experimental data for the peak m/z = 607.077 are shown at the top of the panel and compared with the data calculated for the $[Al_2(L14)_3H_5]^{2+}$ ($C_{57}H_{44}Al_2O_{27}$) complex (lower panel).

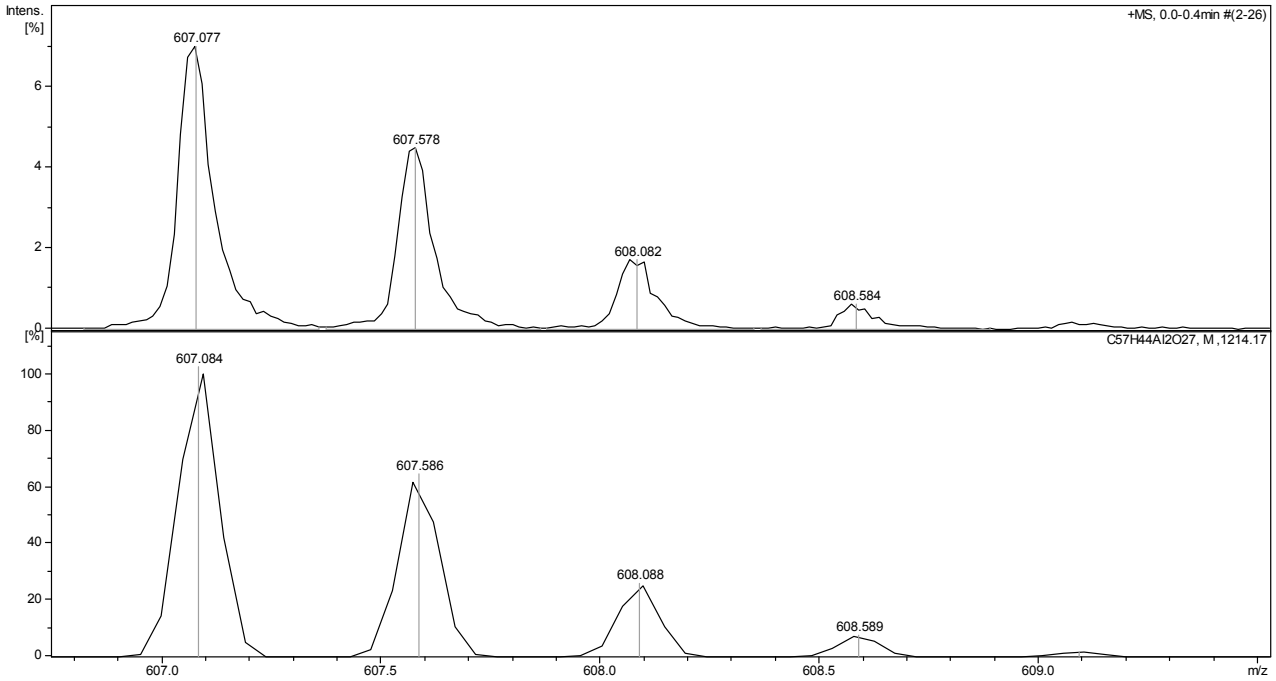

Figure S20. Electrospray ionization with tandem mass spectrometry (MS/MS) spectrum of the $[Al_2(L14)_2H_2]^{2+}$ complex. The peak selected for fragmentation in the MS/MS experiment is indicated by a diamond.

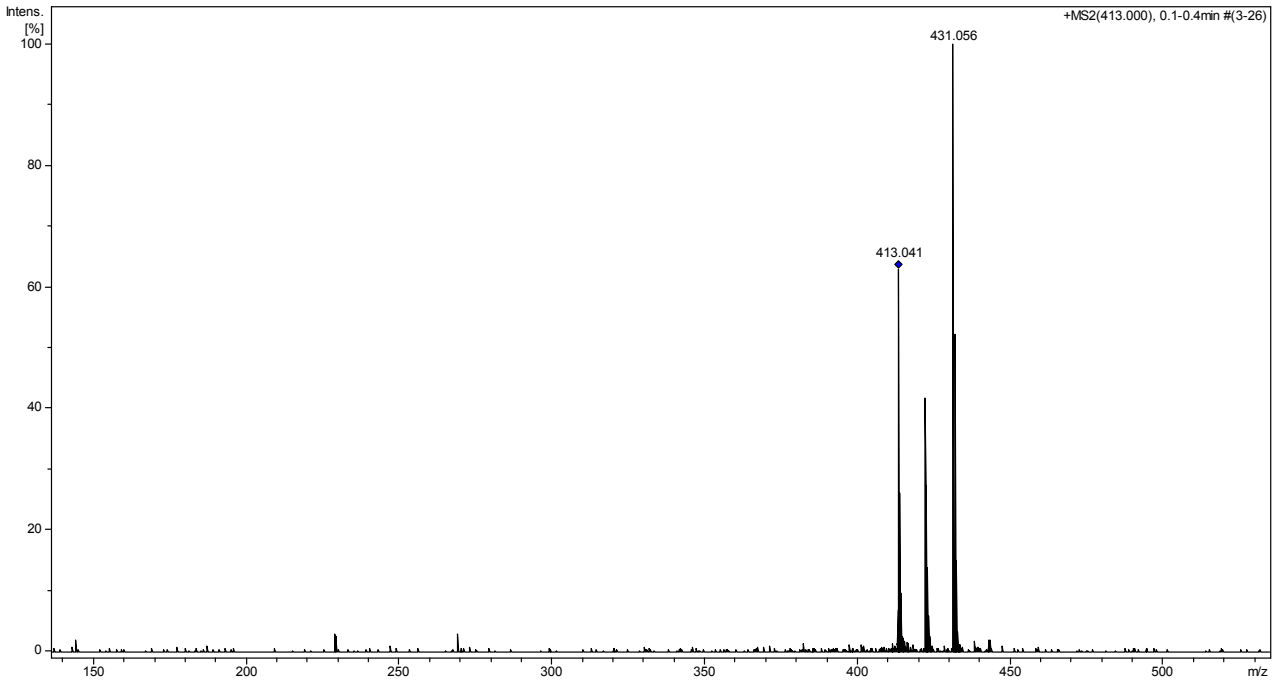

Figure S20A. Experimental data for the peaks m/z = 413.041, 422.049 and 431.056 are shown at the top of the panel and compared with the data calculated for the $[Al_2(L14)_2H_2]^{2+}$ ($C_{38}H_{28}Al_2O_{18}$), $[Al_2(L14)_2H_2+H_2O]^{2+}$ ($C_{38}H_{30}Al_2O_{19}$) and $[Al_2(L14)_2H_2+2H_2O]^{2+}$ ($C_{38}H_{32}Al_2O_{20}$) complexes (lower panels).

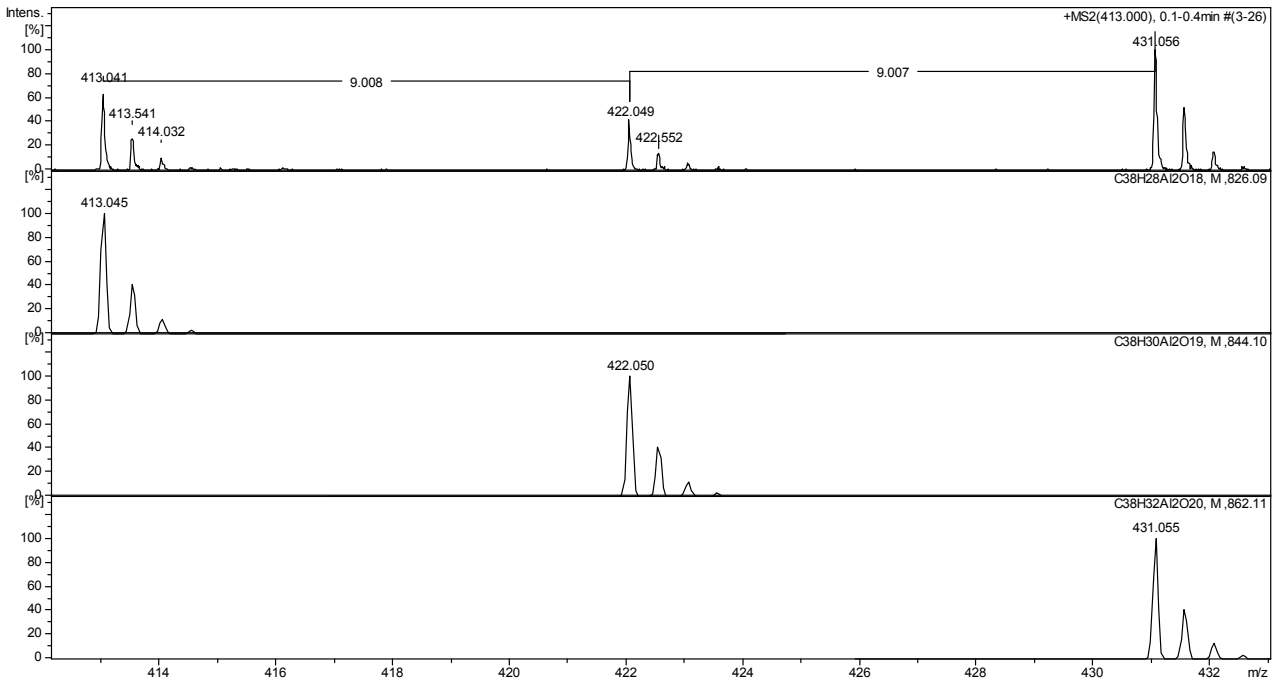

Figure S21. The full spectrum of L14-Cu^{2+} solution in the 1:1 metal-to-ligand molar ratioin positive mode.

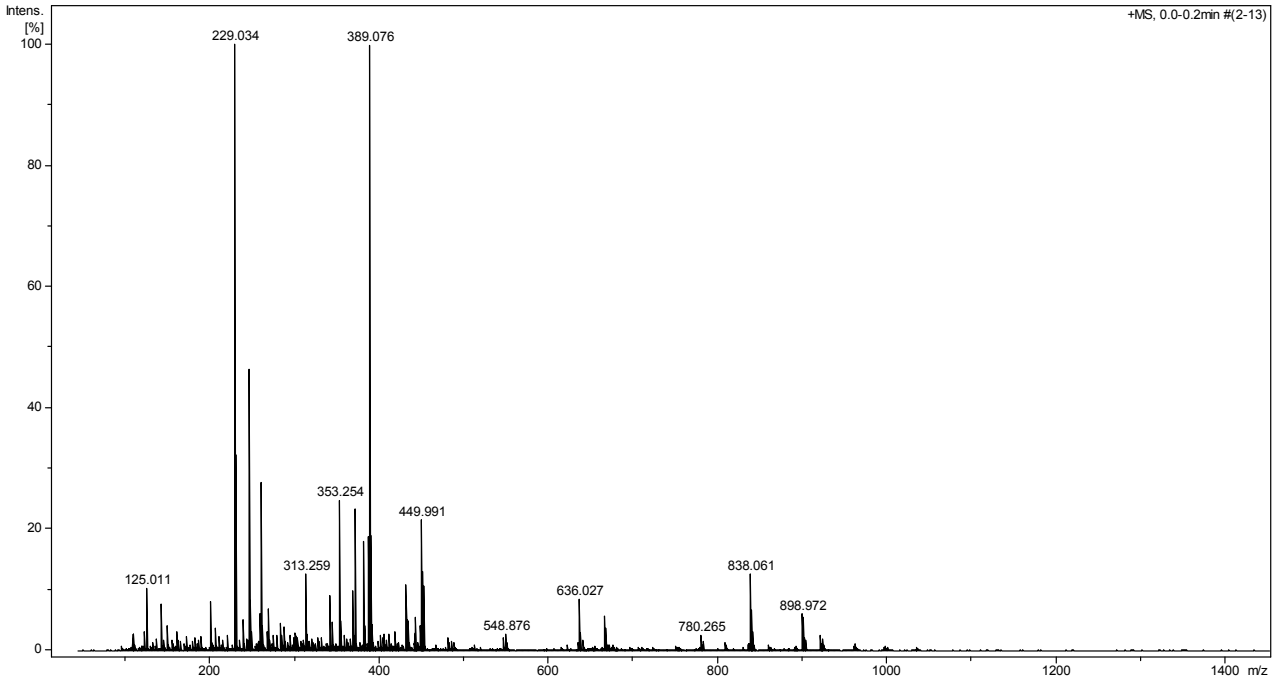

Figure S21A. Experimental data for the peak m/z = 449.991 are shown at the top of the panel and compared with the data calculated for the $[Cu(L14)H_2]^+$ ($C_{19}H_{15}CuO_9$) and $[Cu_2(L14)_2H_4]^{2+}$ ($C_{38}H_{30}Cu_2O_{18}$) complexes (lower panels).

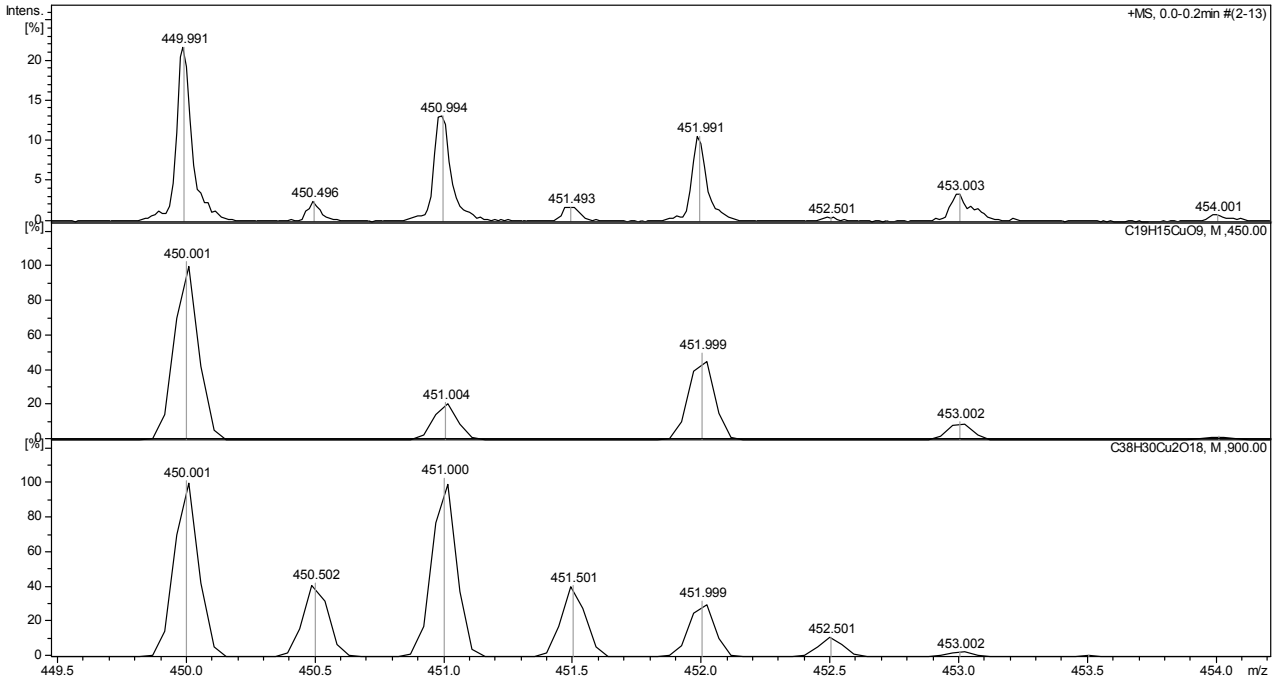

Figure S21B. Experimental data for the peak m/z = 838.061 are shown at the top of the panel and compared with the data calculated for the $[Cu(L14)_2H_5]^+$ ($C_{38}H_{31}CuO_{18}$) complex (lower panel).

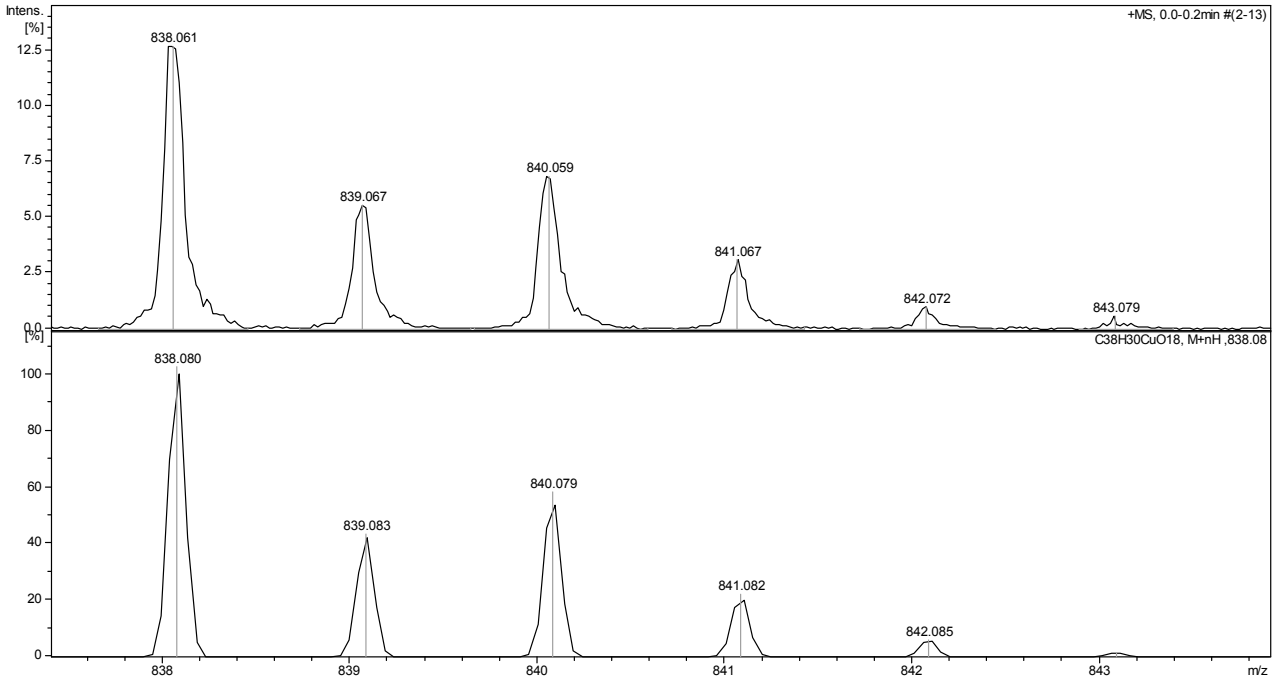

Figure S21C. Experimental data for the peak m/z = 898.972 are shown at the top of the panel and compared with the data calculated for the $[Cu_2(L14)_2H_3]^+$ ($C_{38}H_{29}Cu_2O_{18}$) complex (lower panel).

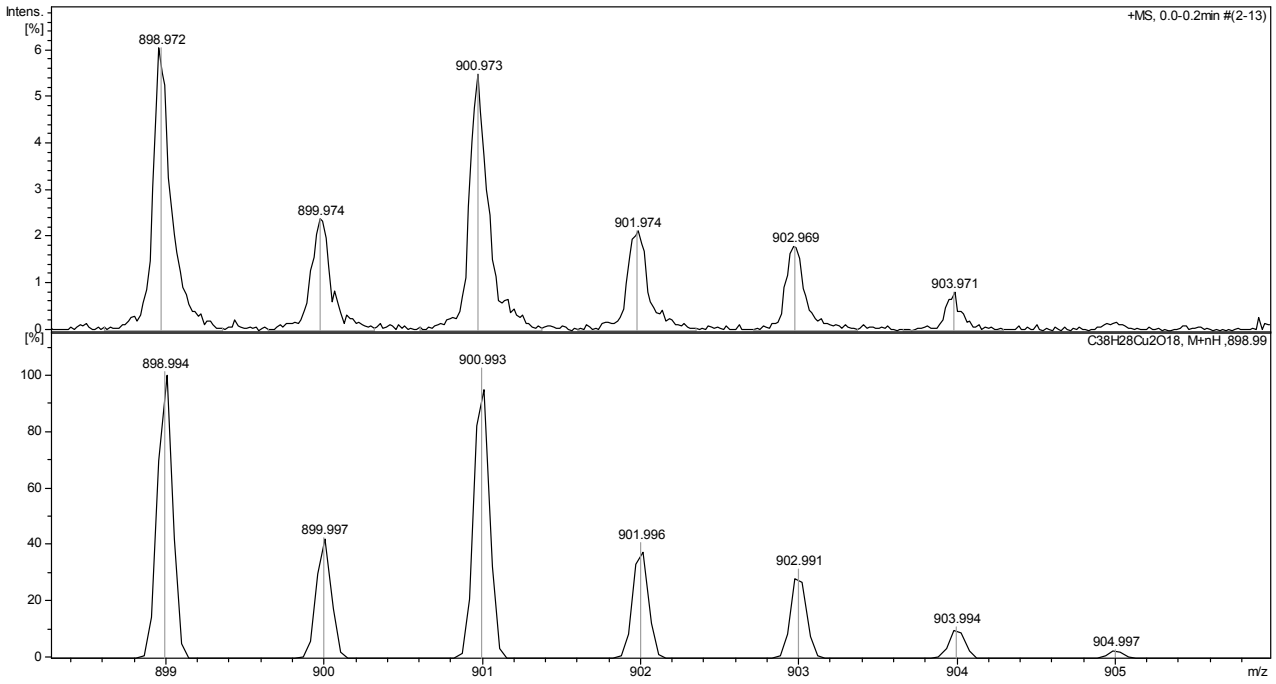

Figure S22. The full spectrum of L14-Fe^{3+} solution in the 1:1 metal-to-ligand molar ratioin positive mode.

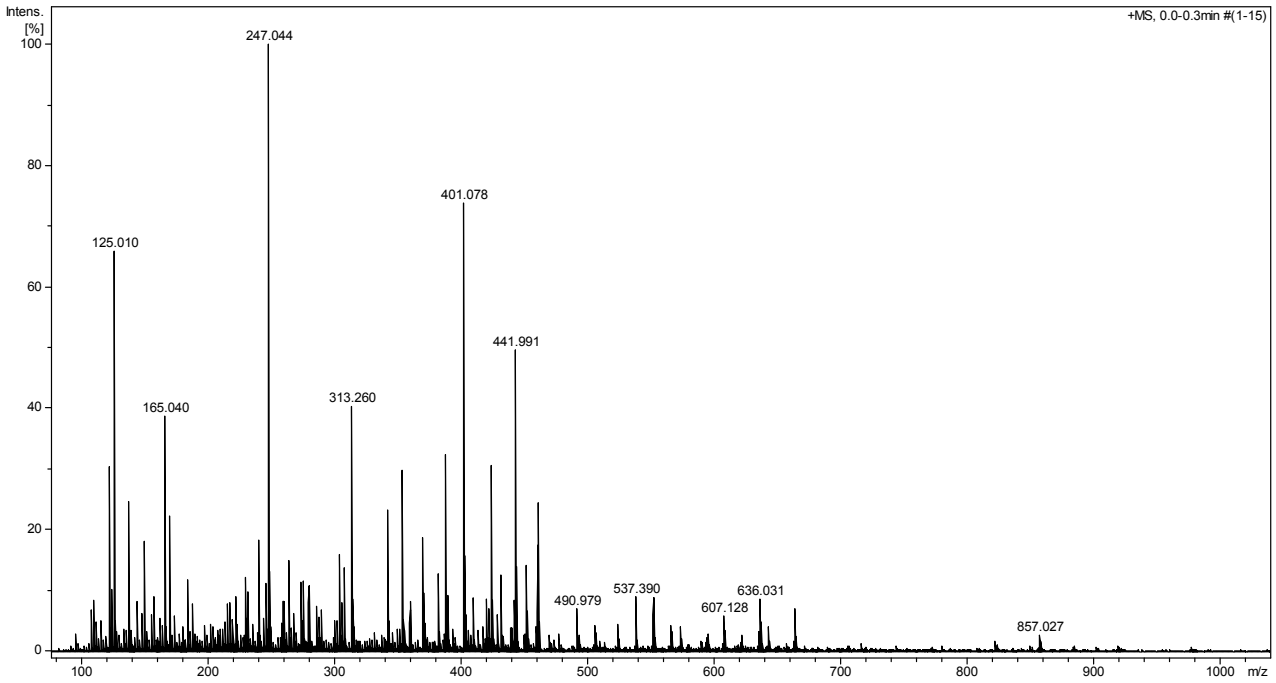

Figure S22A. Experimental data for the peaks m/z = 441.991, 450.998 and 460.004 are shown at the top of the panel and compared with the data calculated for the $[Fe_2(L14)_2H_2]^{2+}$ ($C_{38}H_{28}Fe_2O_{18}$), $[Fe_2(L14)_2H_2+H_2O]^{2+}$ ($C_{38}H_{30}Fe_2O_{19}$) and $[Fe_2(L14)_2H_2+2H_2O]^{2+}$ ($C_{38}H_{32}Fe_2O_{20}$) (lower panels).

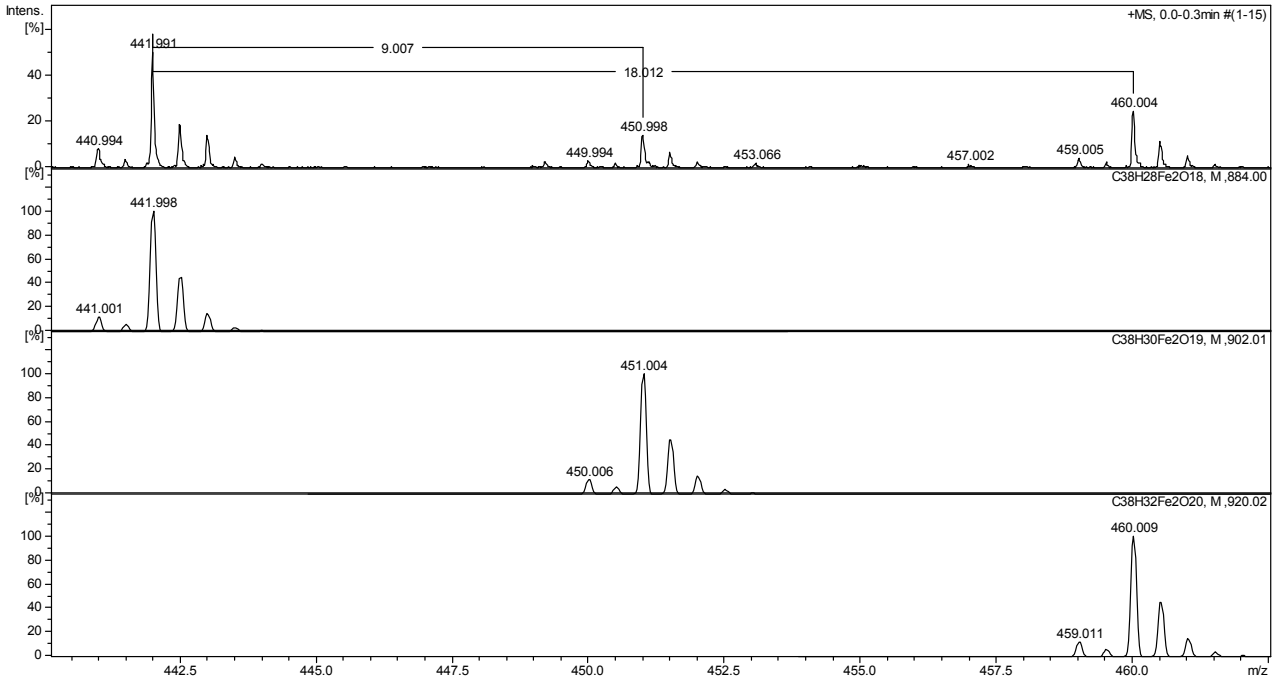

Figure S23. The full spectrum of L14-Zn^{2+} solution in the 1:1 metal-to-ligand molar ratioin positive mode.

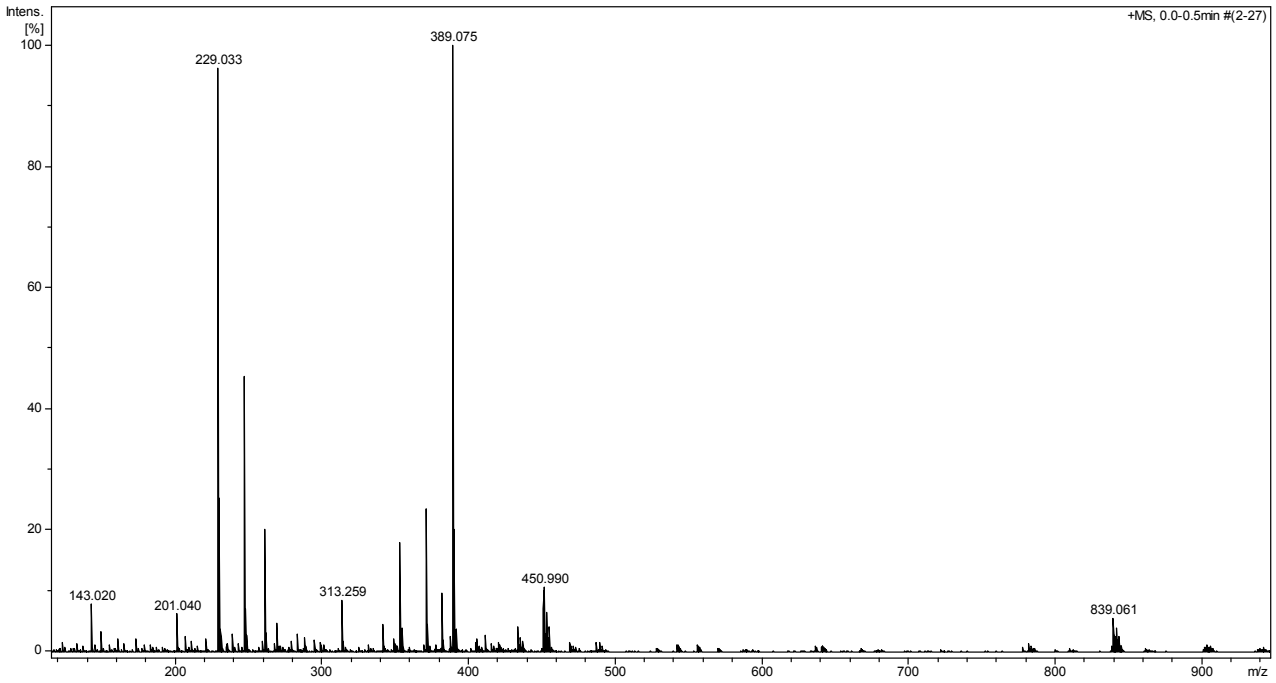

Figure S23A. Experimental data for the peak m/z = 450.990 are shown at the top of the panel and compared with the data calculated for the $[Zn_2(L14)_2H_4]^{2+}$ ($C_{38}H_{30}Zn_2O_{18}$) and $[Zn(L14)H_2]^{+}$ ($C_{19}H_{15}ZnO_9$) complexes (lower panels).

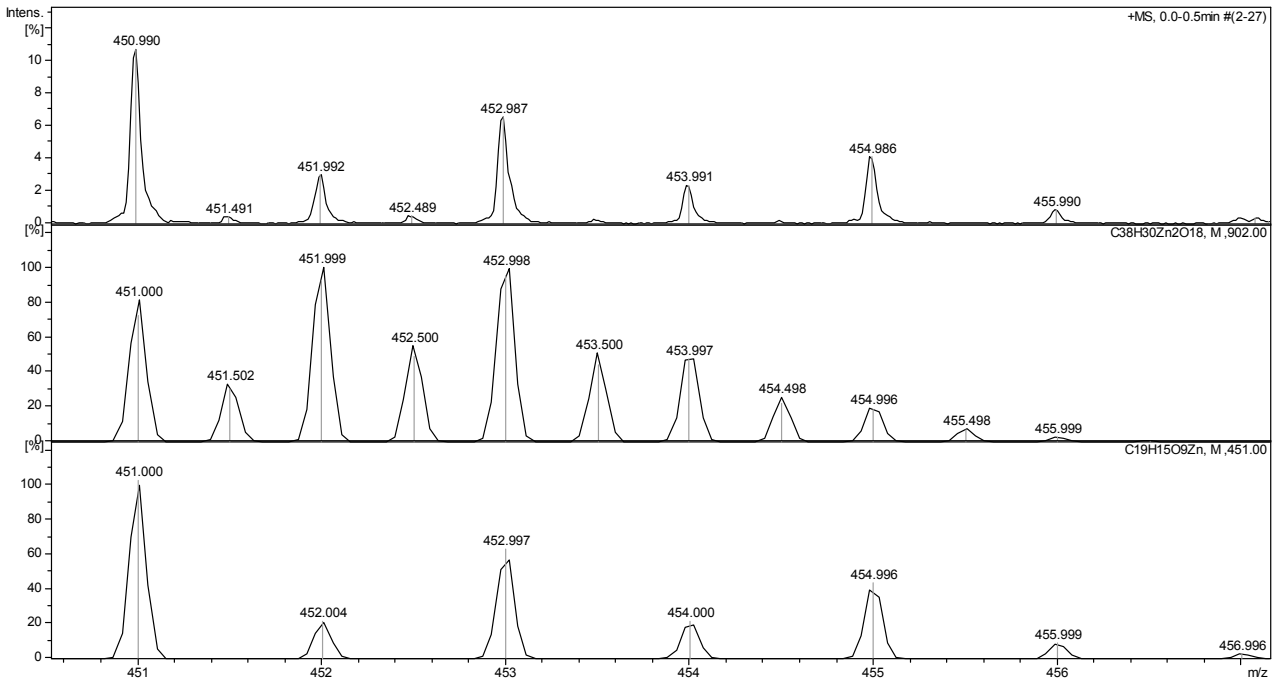

Figure S24. Electrospray ionization with tandem mass spectrometry (MS/MS) spectrum of the $[Zn_2(L14)_2H_4]^{2+}$ complex. The peak selected for fragmentation in the MS/MS experiment is indicated by a diamond.

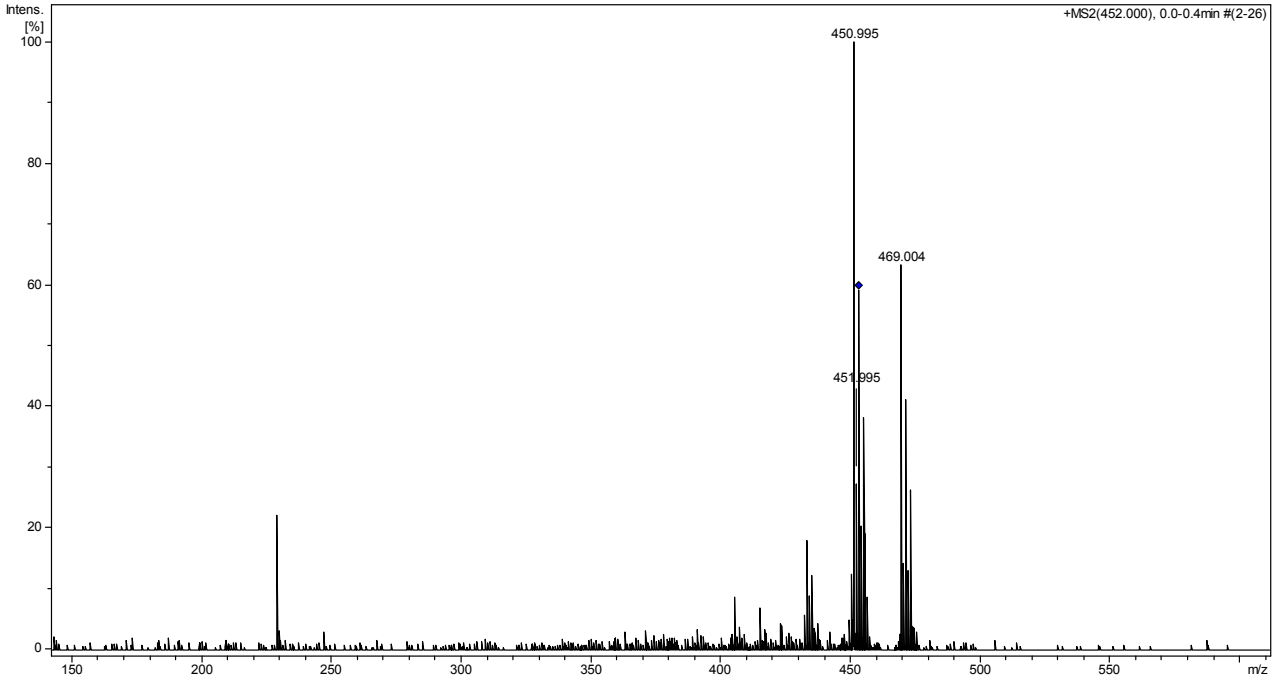

Figure S24A. Experimental data for the peaks m/z = 450.995 and 469.004 are shown at the top of the panel and compared with the data calculated for the $[Zn(L14)H_2]^+$ ($C_{19}H_{15}ZnO_9$) and $[Zn(L14)H_2+H_2O]^+$ ($C_{19}H_{17}O_{10}Zn$) complexes (lower panels).

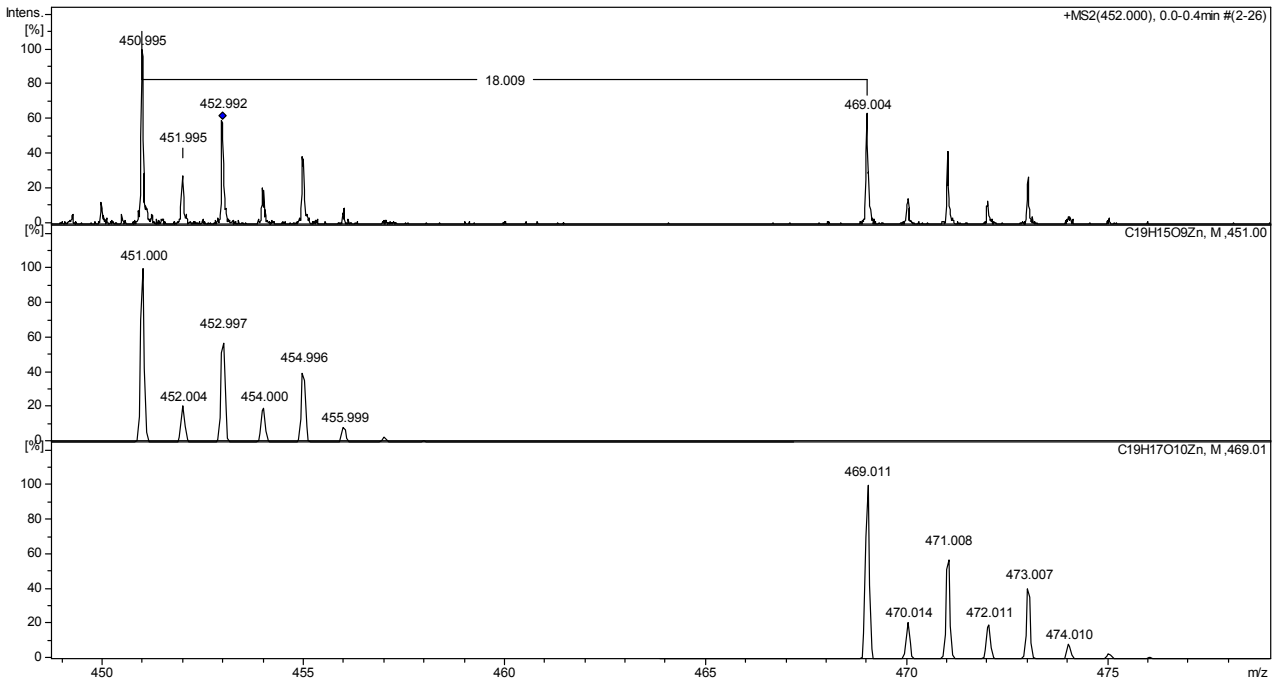

Figure S25. ESI-MS spectrum in positive mode for the L15 compound.

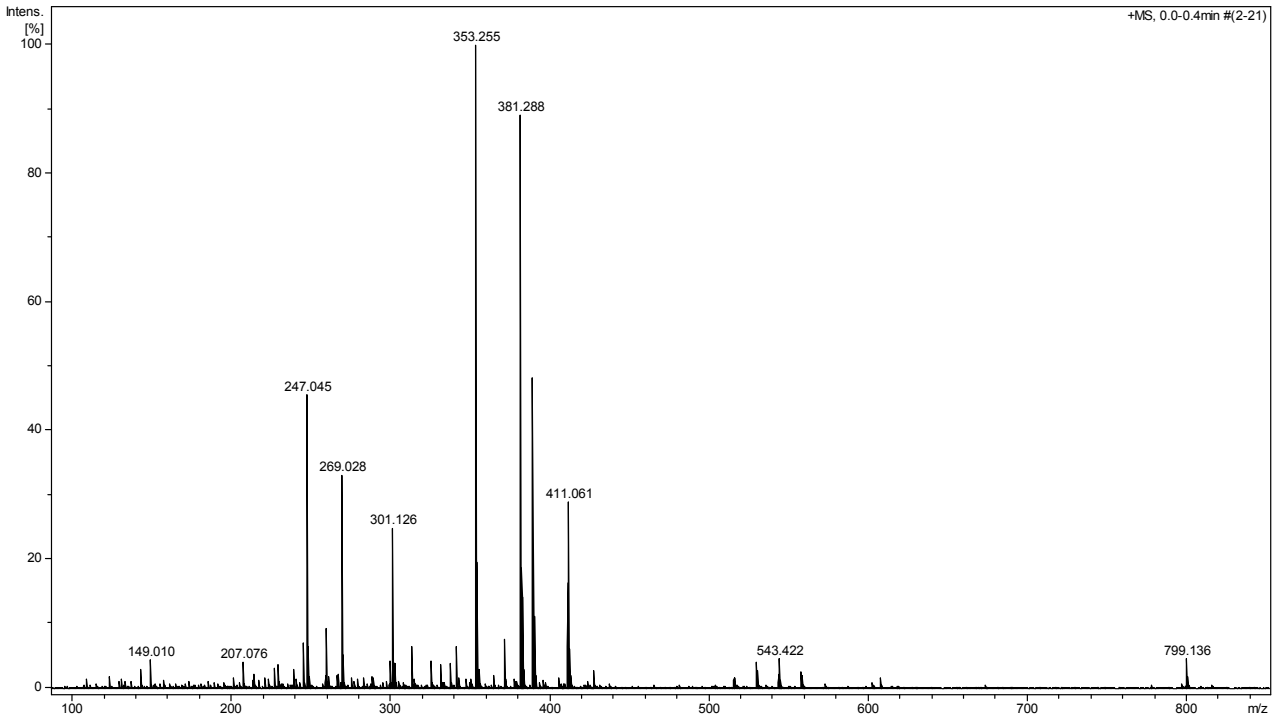

Figure S25A. Experimental data for the peaks m/z = 389.078, 411.061 and 427.031 are shown at the top of the panel and compared with the data calculated for the $[(L15)H_3+H]^+$ ($C_{19}H_{17}O_9$), $[(L15)H_3+Na]^+$ ($C_{19}H_{16}O_9Na$) and $[(L15)H_3+K]^+$ ($C_{19}H_{16}O_9K$) (lower panels).

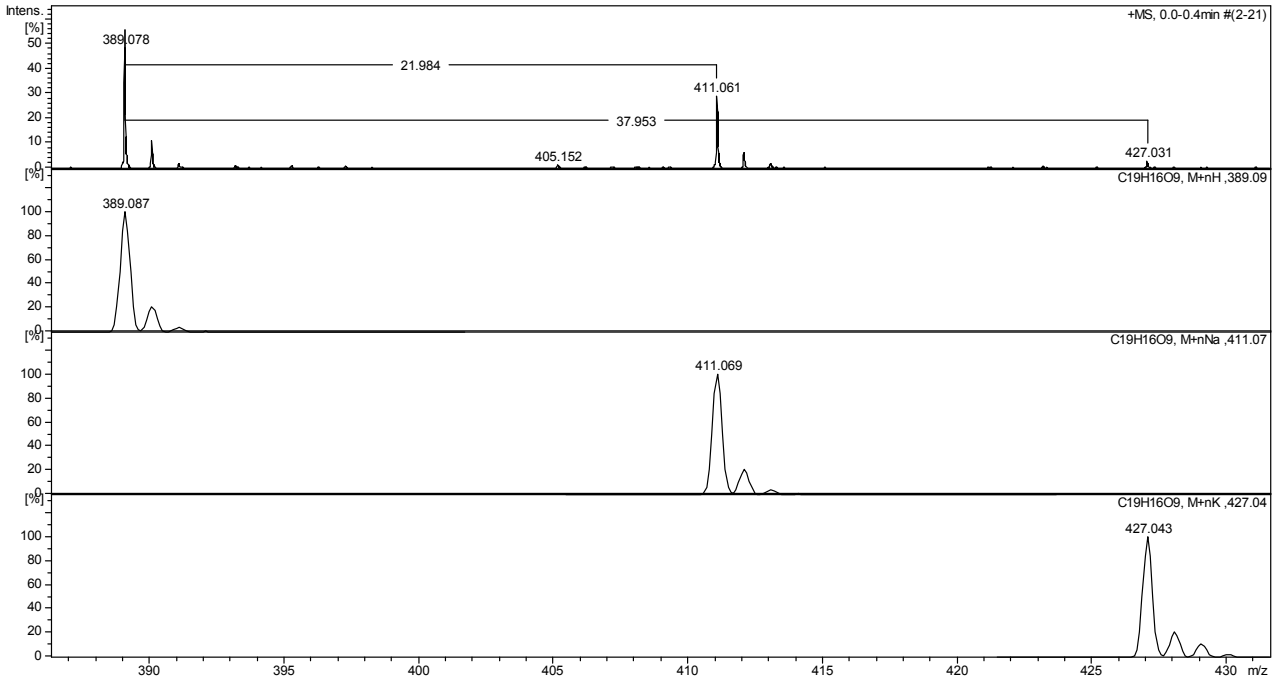

Figure S26. The full spectrum of L15-Cu^{2+} solution in the 1:1 metal-to-ligand molar ratioin positive mode.

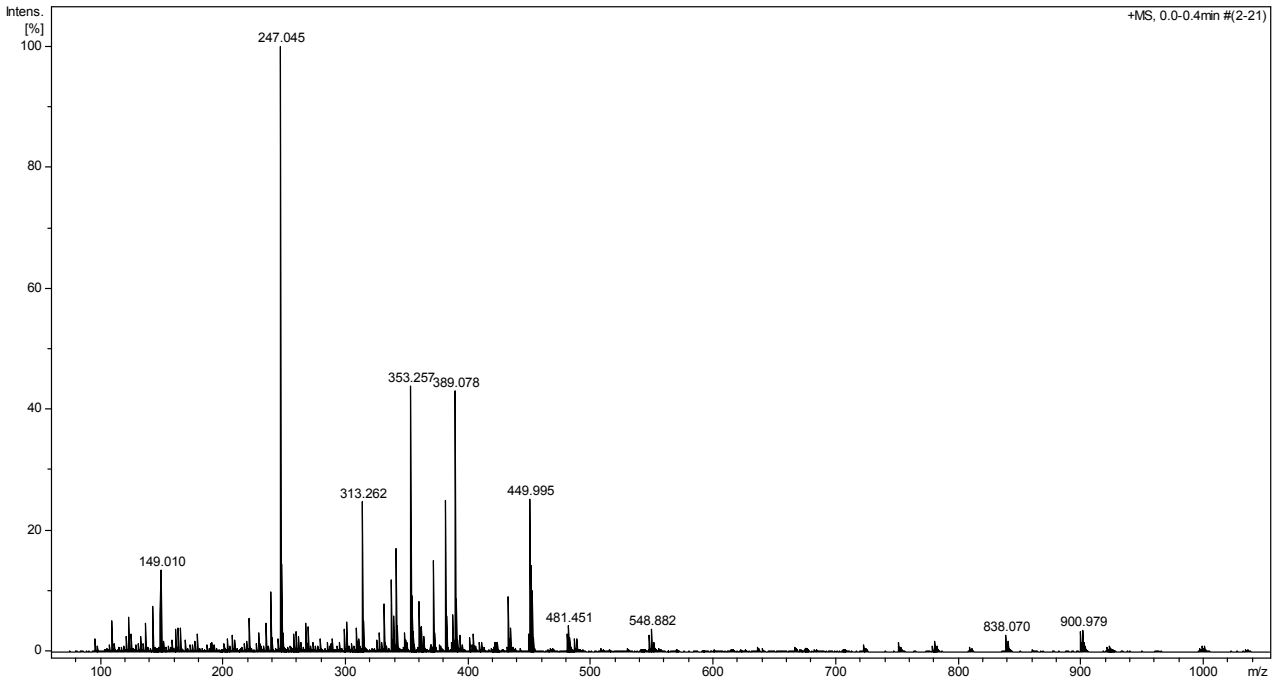

Figure S26A. Experimental data for the peak m/z = 449.995 are shown at the top of the panel and compared with the data calculated for the $[Cu(L15)H_2]^+$ ($C_{19}H_{15}CuO_9$) and $[Cu_2(L15)_2H_4]^{2+}$ ($C_{38}H_{30}Cu_2O_{18}$) (lower panels).

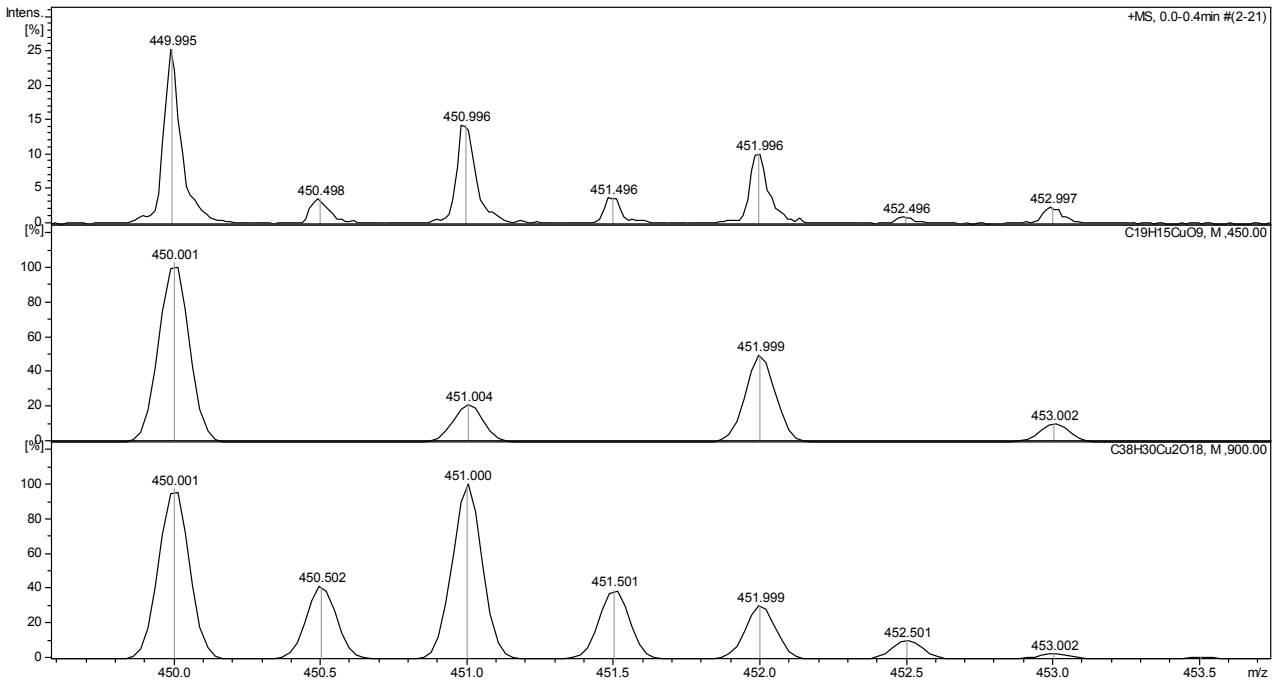

Figure S26B. Experimental data for the peaks m/z = 898.983 and 920.976 are shown at the top of the panel and compared with the data calculated for the $[Cu_2(L15)_2H_3]^+$ ($C_{38}H_{29}Cu_2O_{18}$) and $[Cu_2(L15)_2H_2+Na]^+$ ($C_{38}H_{28}Cu_2O_{18}Na$) complexes (lower panels).

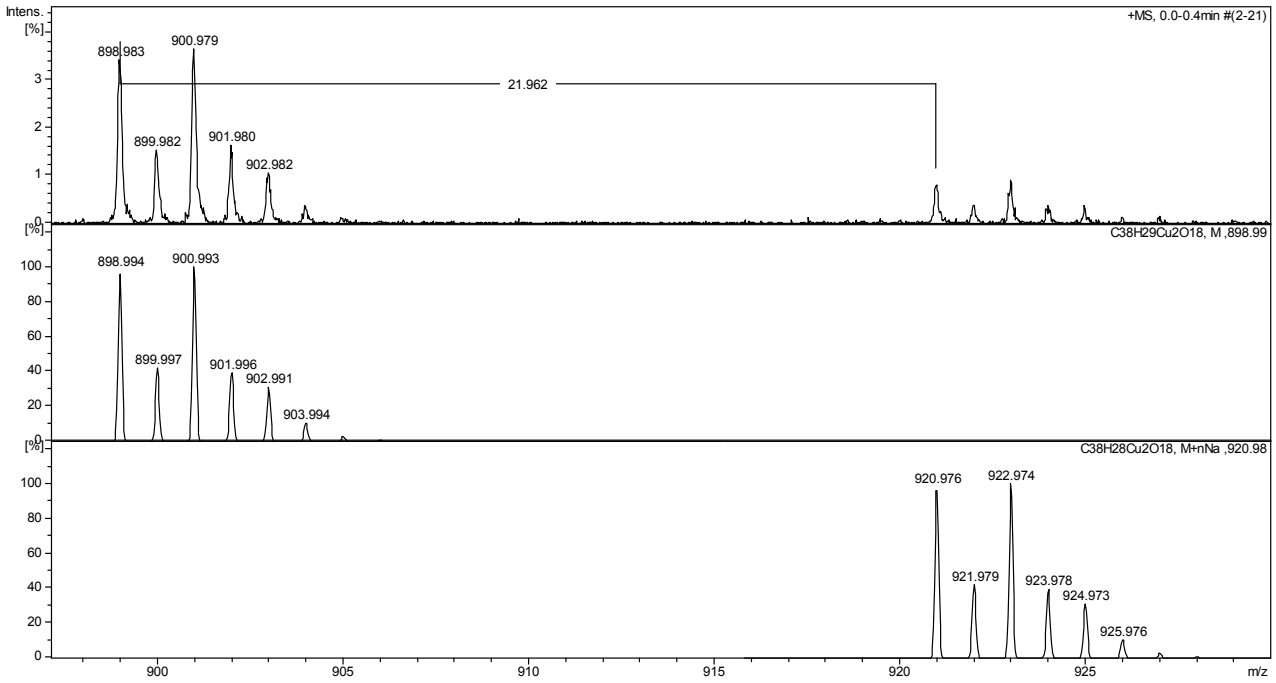

Figure S27. The full spectrum of L15-Fe^{3+} solution in the 1:1 metal-to-ligand molar ratioin positive mode.

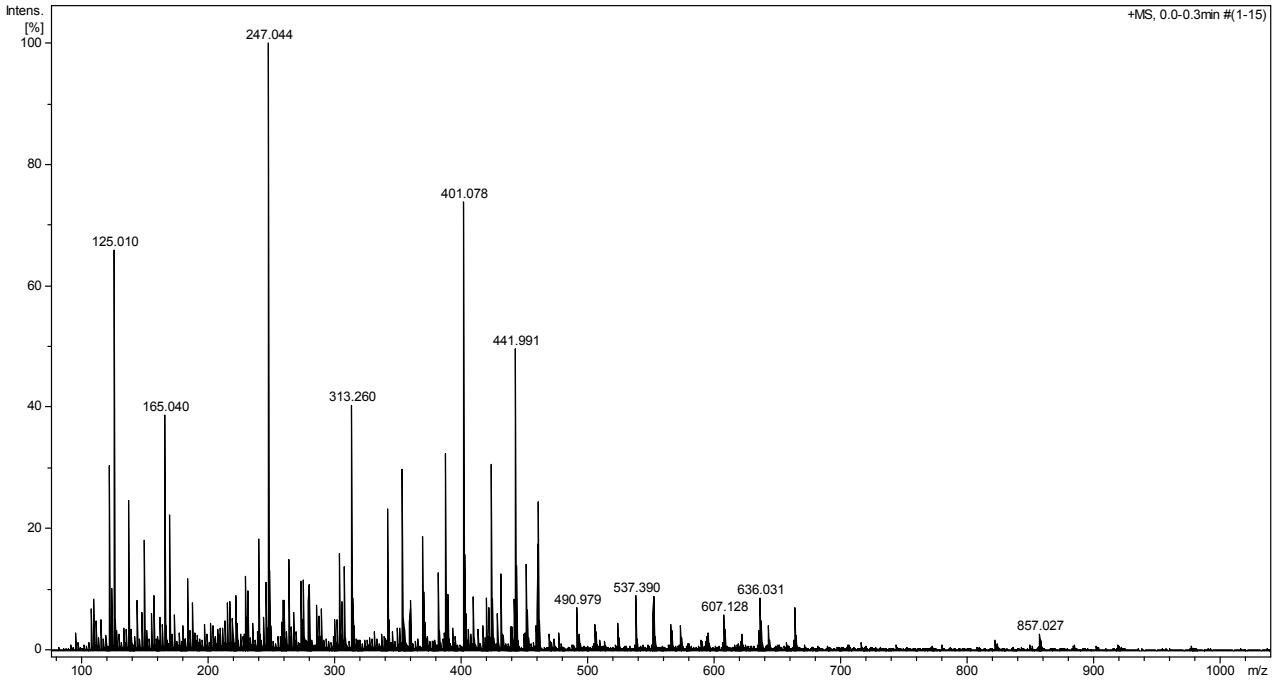

Figure S27A. Experimental data for the peaks m/z = 441.991, 450.998 and 460.004 are shown at the top of the panel and compared with the data calculated for the $[Fe_2(L15)_2H_2]^{2+}$ ($C_{38}H_{28}Fe_2O_{18}$), $[Fe_2(L15)_2H_2+H_2O]^{2+}$ ($C_{38}H_{30}Fe_2O_{19}$) and $[Fe_2(L15)_2H_2+2H_2O]^{2+}$ ($C_{38}H_{32}Fe_2O_{20}$) (lower panels).

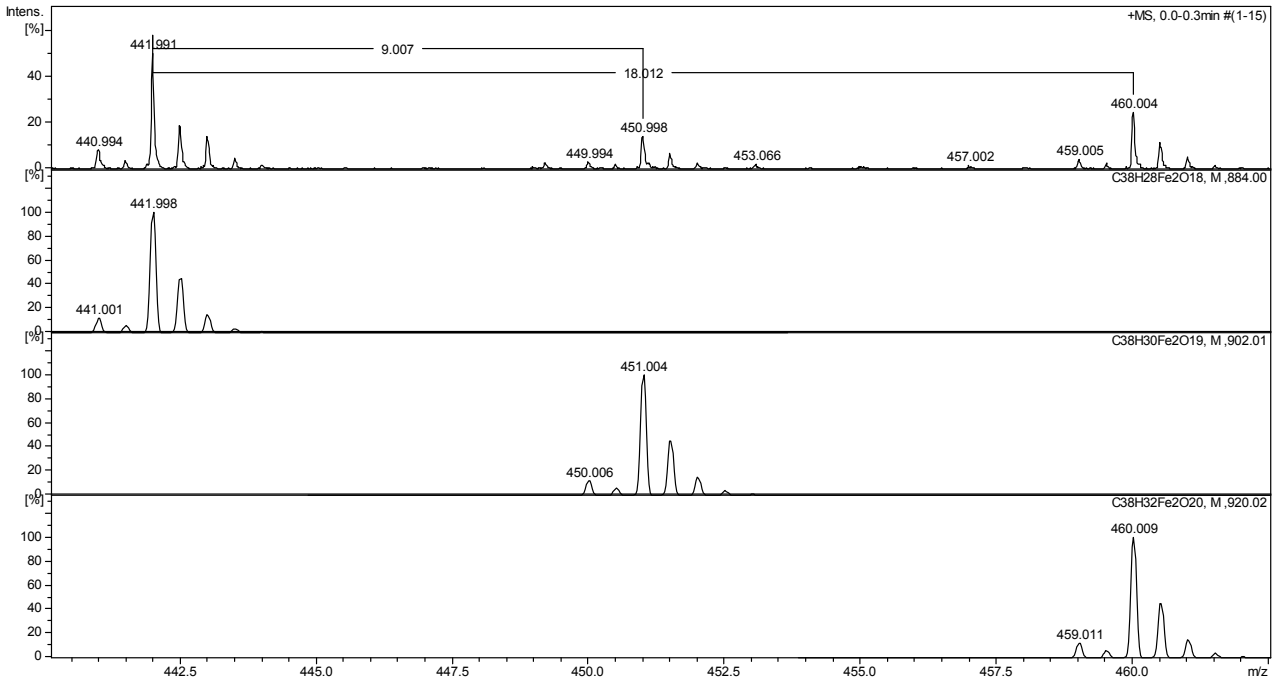

Figure S28. The full spectrum of L15-Zn^{2+} solution in the 1:1 metal-to-ligand molar ratioin positive mode.

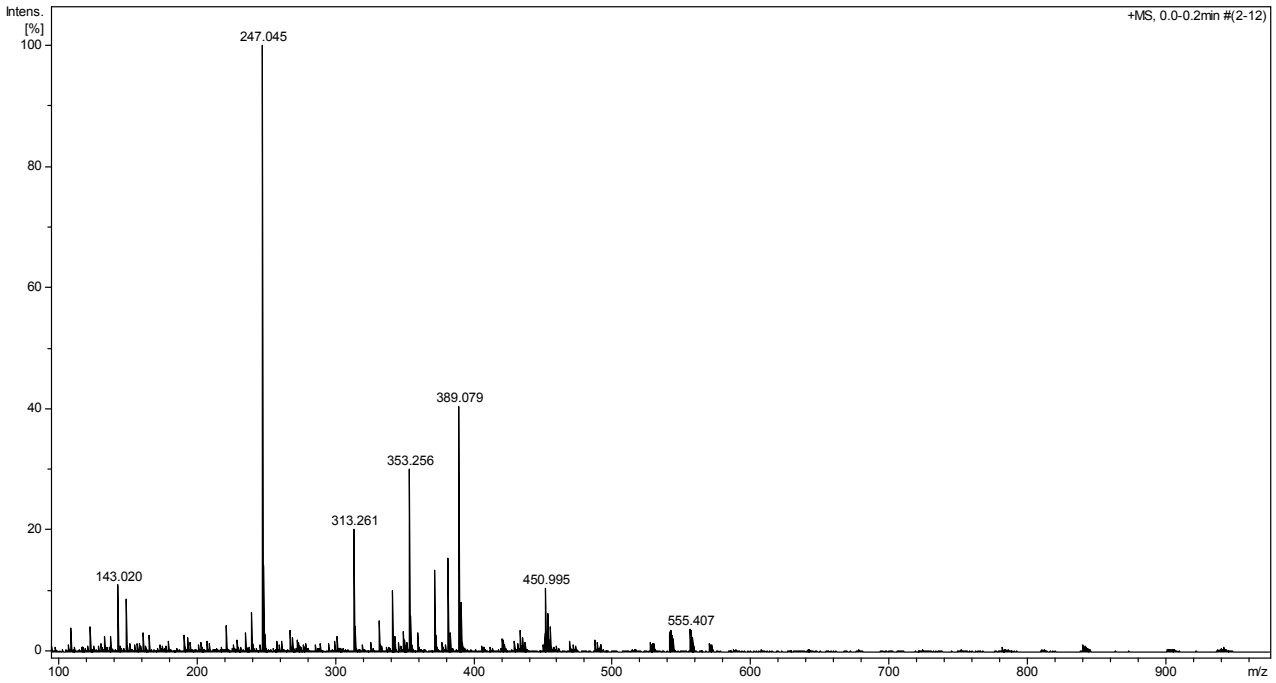

Figure S28A. Experimental data for the peak m/z = 450.995 are shown at the top of the panel and compared with the data calculated for the $[Zn(L15)H_2]^+$ ($C_{19}H_{15}O_9Zn$) and $[Zn_2(L15)_2H_4]^{2+}$ ($C_{38}H_{30}Zn_2O_{18}$) complexes (lower panels).

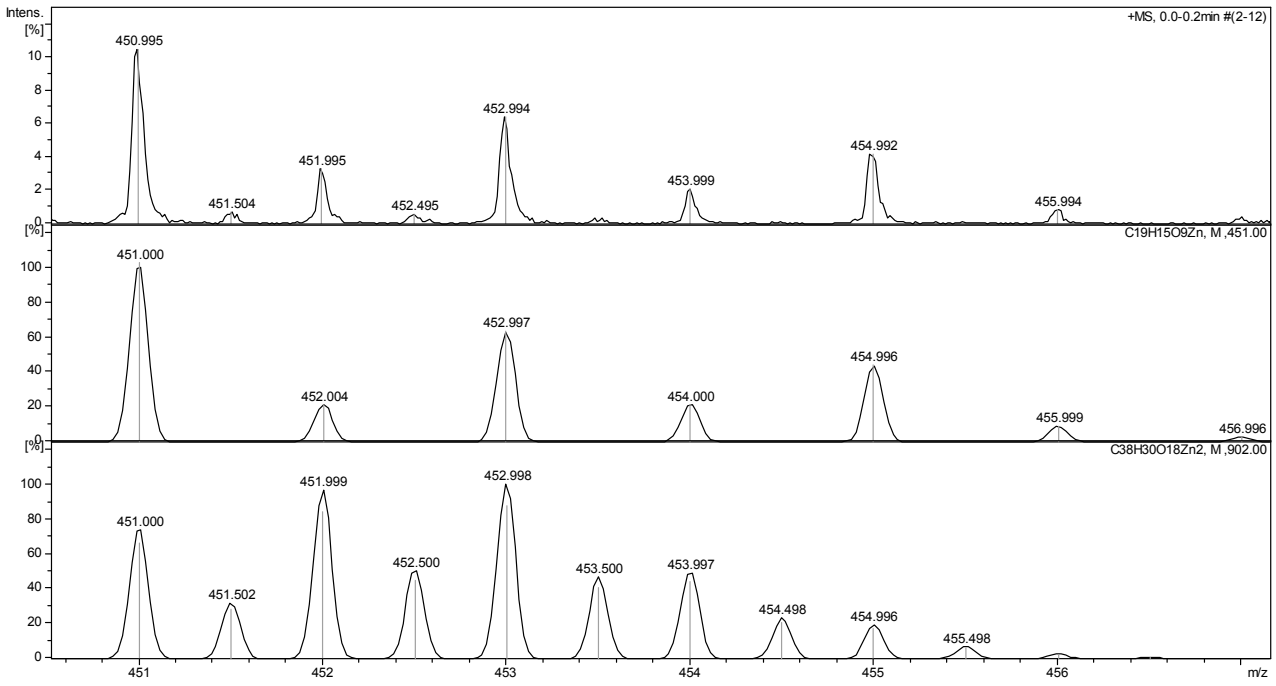

Figure S28B. Experimental data for the peaks m/z = 469.006 and 486.977 are shown at the top of the panel and compared with the data calculated for the $[Zn(L15)H_2+H_2O]^+$ ($C_{19}H_{17}O_{10}Zn$) and $[Zn(L15)H_2+2H_2O]^+$ ($C_{19}H_{19}O_{11}Zn$) complexes (lower panels).

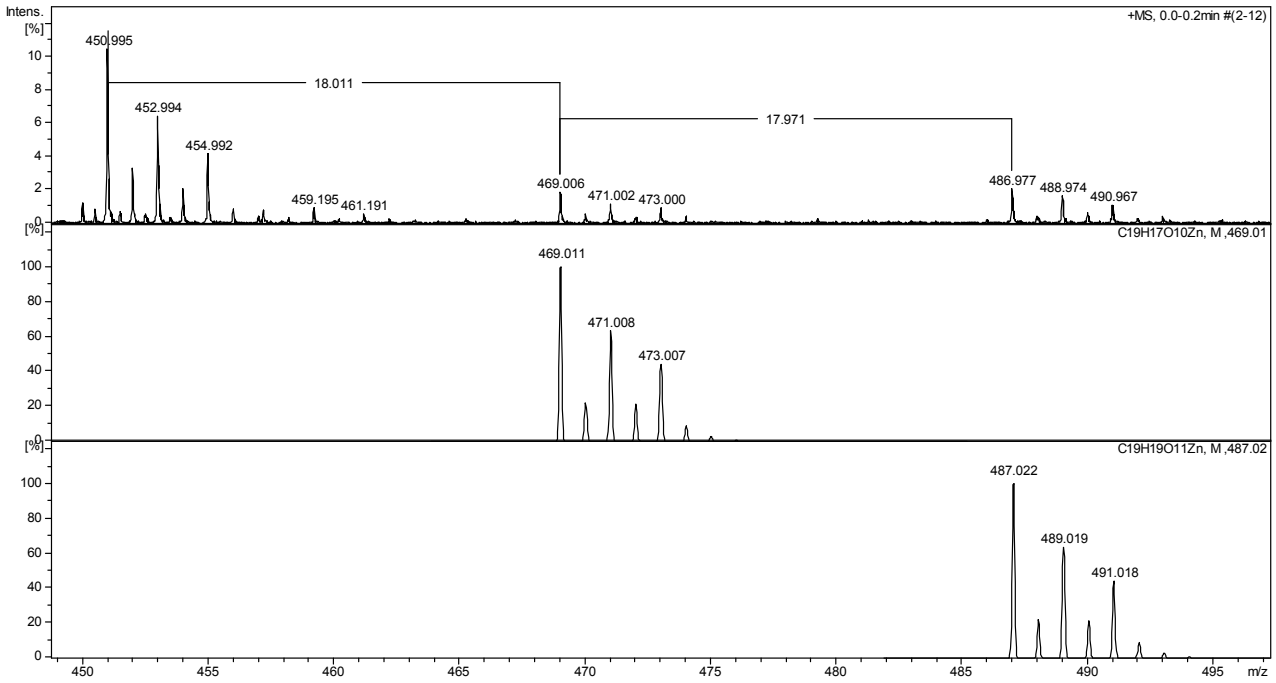

Figure S29. The full spectrum of L15-Al^{3+} solution in the 1:1 metal-to-ligand molar ratioin positive mode.

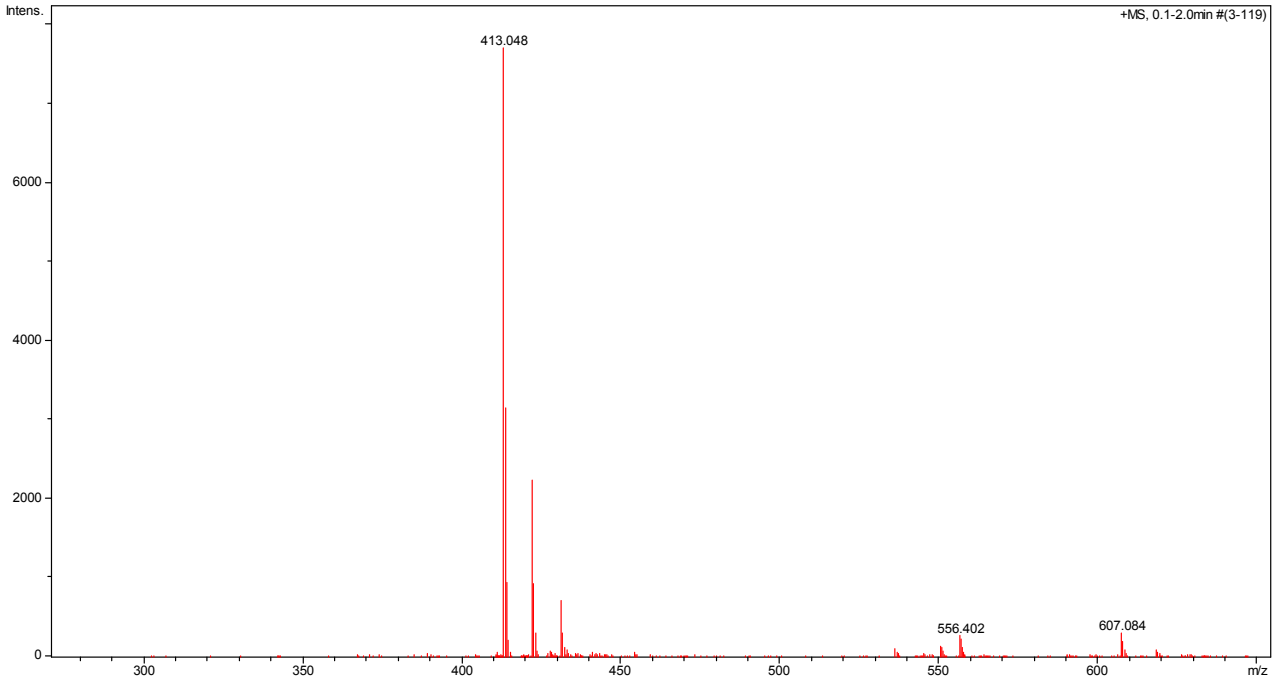

Figure S29A. Experimental data for the peaks m/z = 413.048, 422.054 and 431.057 are shown at the top of the panel and compared with the data calculated for the $[Al_2(L15)_2H_2]^{2+}$ ($C_{38}H_{28}Al_2O_{18}$), $[Al_2(L15)_2H_2+H_2O]^{2+}$ ($C_{38}H_{30}Al_2O_{19}$) and $[Al_2(L15)_2H_2+2H_2O]^{2+}$ ($C_{38}H_{32}Al_2O_{20}$) complexes (lower panels).

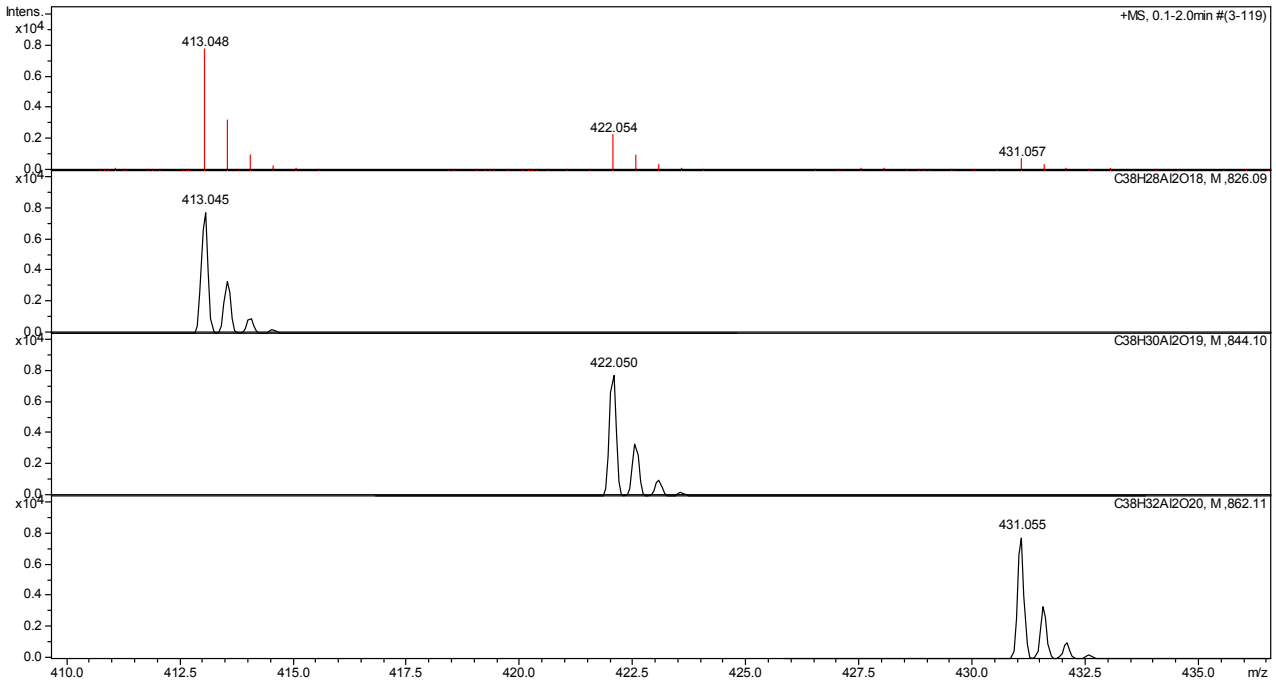

Figure S29B. Experimental data for the peak m/z = 607.084 are shown at the top of the panel and compared with the data calculated for the $[Al_2(L15)_3H_5]^{2+}$ ($C_{57}H_{44}Al_2O_{27}$) complex (lower panel).

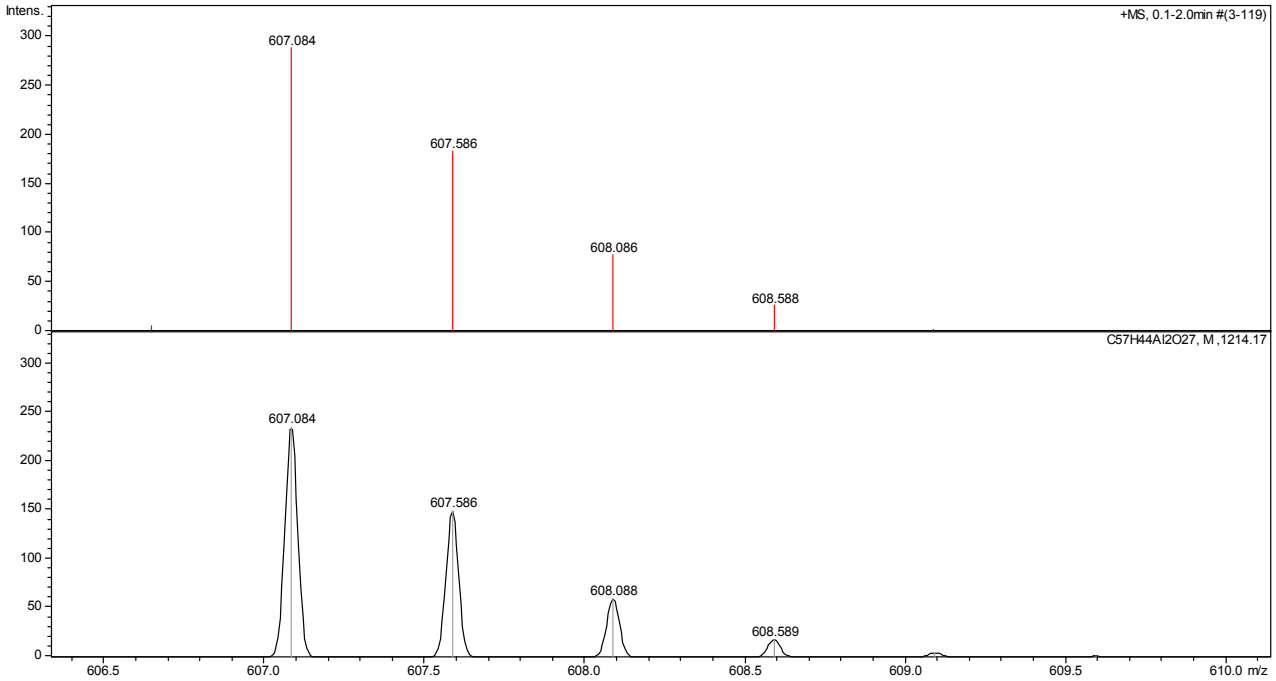

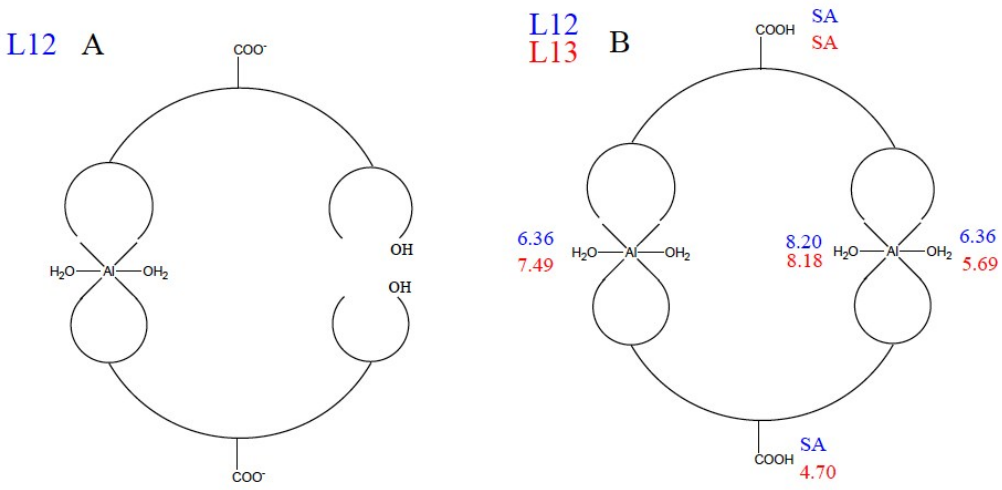

Scheme S1. Hypothesized coordination scheme of L12-L13 ligands with Al^{3+}.

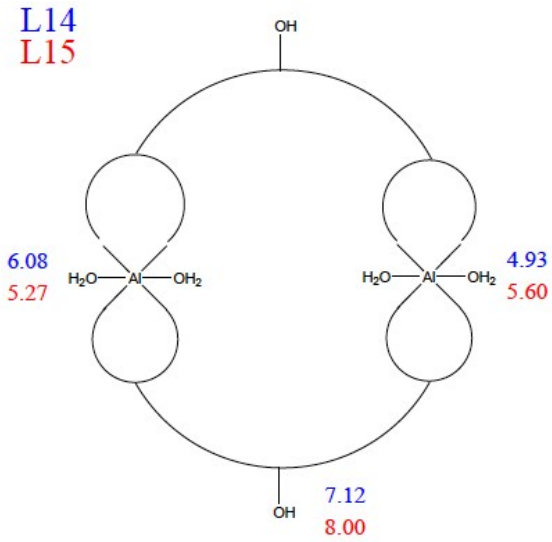

Scheme S2. Hypothesized coordination scheme of L14-L15 ligands with Al^{3+}.

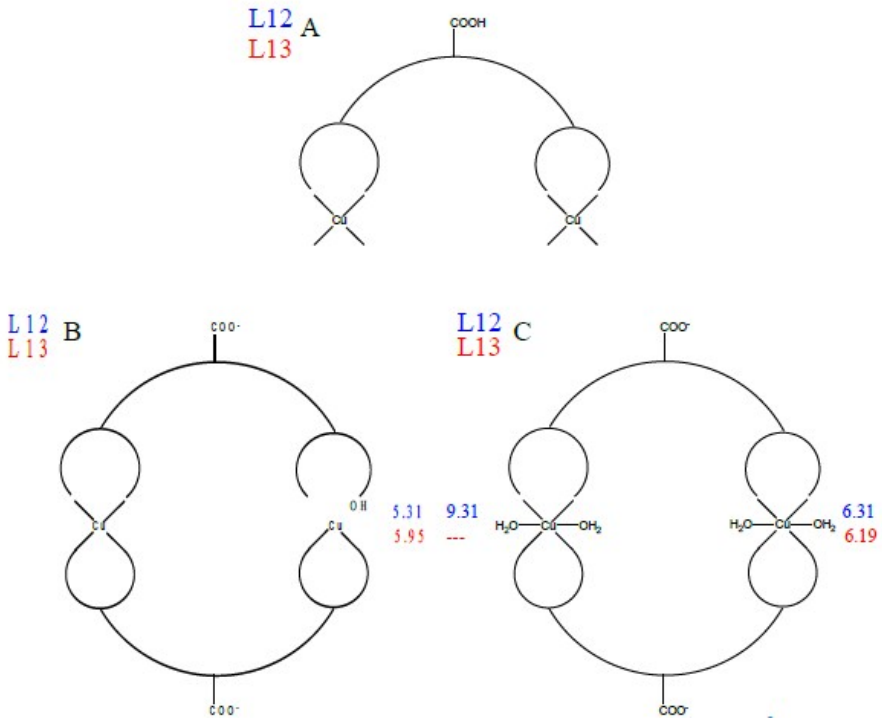

Scheme S3. Hypothesized coordination scheme of L12-L13 ligands with Cu^{2+}.

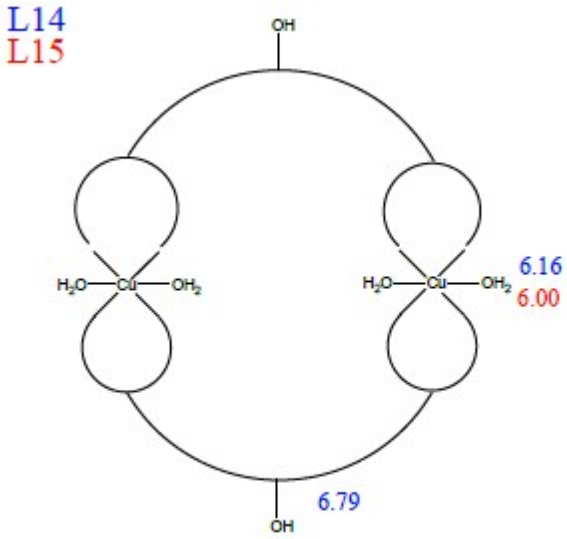

Scheme S4. Hypothesized coordination scheme of L14-L15 ligands with Cu^{2+}.

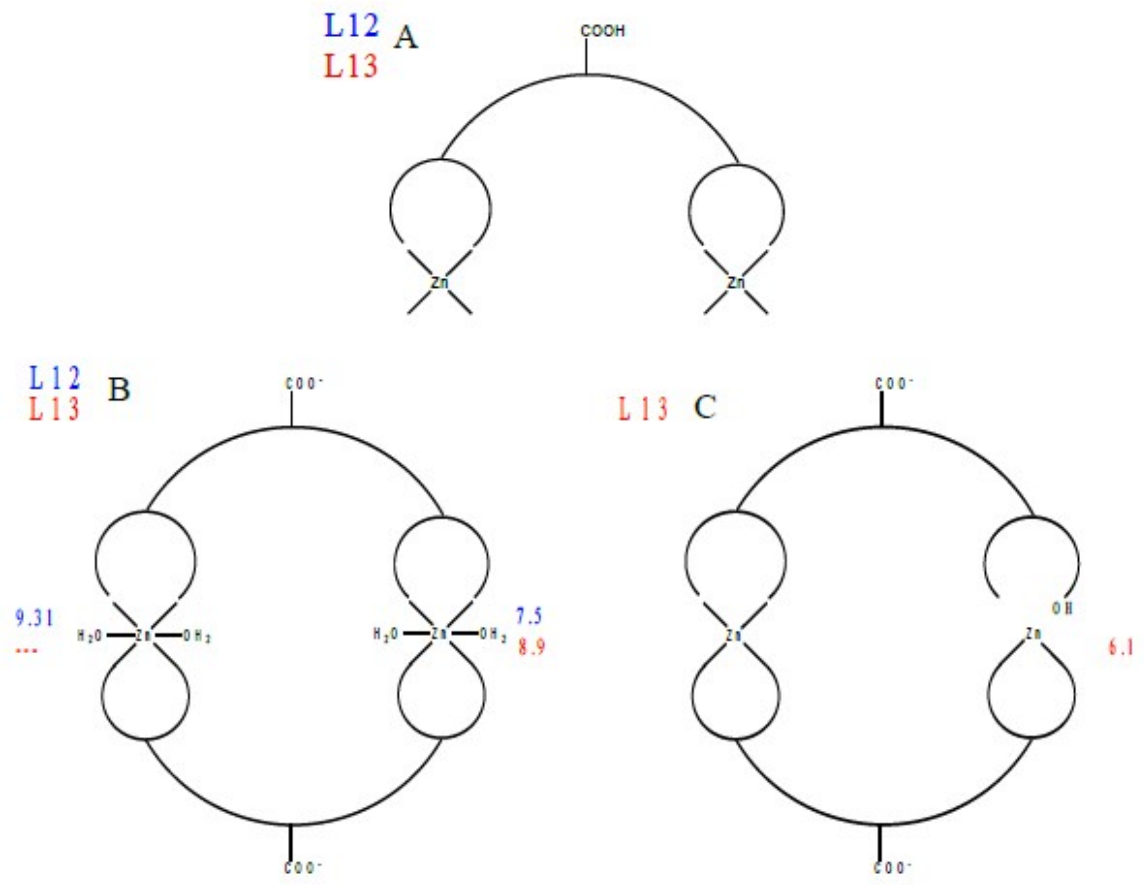

Scheme S5. Hypothesized coordination scheme of L12-L13 ligands with Zn^{2+}.

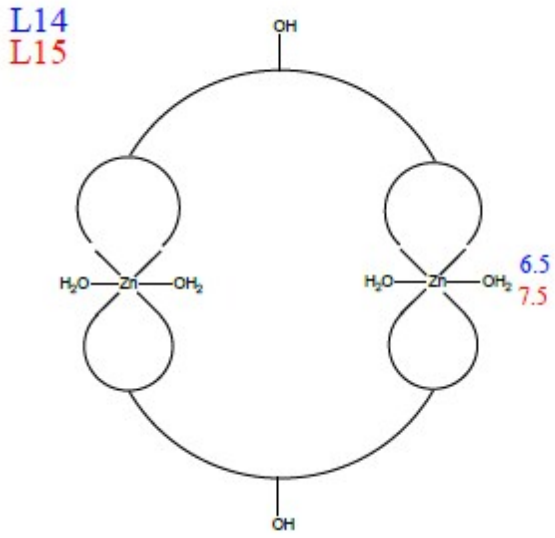

Scheme S6. Hypothesized coordination scheme of L14-L15 ligands with Zn^{2+}.